People's Democratic Republic of Algeria

وزارة التعليم العالي والبحث العلمي

Ministry of Higher Education and Scientific Research

جامعة حسيبة بن بوعلي الشلف

Hassiba Benbouali University – Chlef

Faculty of Civil Engineering and Architecture

Department of Hydraulics

END OF STUDY Dissertation

To obtain the diploma of

Master

Sector: Hydraulic

Specialty: Urban Hydraulic

By

TOUBA WAFA

Theme: Using Tropical Rainfall Measuring Mission for Accurate Daily Runoff Modeling using intelligent systems: The Case of Chelif Basin (Wadi ouahrane basin in Northen Algeria).

Dissertation defense : 2024/06/30/ in front of the jury composed of

Meziane Nasreddine	Doctor/MCA	Hassiba Benbouali University of Chlef	President
Chenaoui Bakhta	Doctor/MCA	Hassiba Benbouali University of Chlef	Examiner
Bilel Zerouali	Doctor/MCB	Hassiba Benbouali University of Chlef	Supervisor
Celso Augusto Guimarães Santos	Professor	Federal University of Paraíba, João Pessoa, Brazil	Co-Supervisor

University year : 2023/2024

Dr. Bilel Zerouali
- Department of Hydraulic
- Hassiba Benbouali, University of Chlef, Algeria
- Hassiba Benbouali, University of Chlef, B.P. 78C, Ouled Fares, 02180, Chlef, Algeria
- Chlef, 02180
- Email: b.zerouali@univ.chlef.dz

Prof. Dr. Celso Augusto Guimarães Santos
- Department of Civil and Environmental Engineering
- Federal University of Paraíba, João Pessoa, Brazil
- Federal University of Paraíba, 58051-900 João Pessoa, Brazil
- João Pessoa, 58051-900
Email: celso@ct.ufpb.br

30/05/2023

Miss. Wafa Touba (Master's student)
Department of Hydraulic, Faculty of Civil Engineering and Architecture, University of Chlef, B.P. 78C, Ouled Fares, 02180, Chlef, Algeria]
Phone: +213 697 84 83 03
Email: wafatouba@yahoo.com

Dear Wafa Touba,

Thank you for your interest in pursuing a Master's degree under our supervision. We have carefully reviewed your application materials and we are pleased to inform you that we are willing to accept you as our graduate student.

Your academic record, research experience, and proposed research topic are impressive. We appreciate your interest in hydrology and water resources topics, which is an area of great interest to us and one in which we have considerable expertise. We are confident that we can provide you with the guidance and support you need to successfully complete your Master's thesis in this area.

The title of your Master's thesis will be "**Using Tropical Rainfall Measuring Mission for Accurate Daily Runoff Modeling using Intelligent Systems: The Case of Chelif Basin (Northern Algeria)".** The aim of your research is to compare real rainfall with that of satellite observation for accurate daily runoff modeling using advanced machine learning models. We believe that this is a well-defined and interesting research problem that has the potential to contribute to the field. We look forward to working with you to develop a detailed research plan and to guide you throughout the research process.

Please let us know if you have any questions or concerns. We are available to discuss any aspect of your project and to provide you with the resources you need to get started. We would also like to arrange a meeting with you to discuss your research proposal in further detail and to establish a timeline for the project.

Congratulations on your acceptance as our graduate student and I look forward to working with you.
Sincerely.

Supervisor's Name

Co-Supervisor's Name

Acknowledgement

بسم الله الرحمان الرحيم

(وَقُلِ اعْمَلُوا فَسَيَرَى اللَّهُ عَمَلَكُمْ وَرَسُولُهُ وَالْمُؤْمِنُونَ)

صدق الله العظيم

إله لا يطيب الليل الا بشكره والا يطيب النهار الا بطاعته والا تطيب اللحظات الا بذكره الله جل جلاله

الى من بلغ الرسالة وأدى الأمانة ونصح الامة نبي الرحمة ونور للعالمين

"سيدنا محمد صلى الله عليه وسلم"

Firstly, I express my gratitude to Allah for protecting me and granting me the ability to work diligently. I am immensely thankful to the University of Hassiba Ben Bouali for providing me with the opportunity to pursue my studies here.

I would like to extend special thanks to my parents, Mr. Djamel and Mrs. Meriem Lazaar, for their unwavering support throughout my journey, both emotionally and financially, and for always believing in me. I cannot forget my best sisters, Rima and Chaima, for their support and encouragement. I am especially grateful to my supervisor, ***Dr. ZEROUALI Bilel****, whose guidance was instrumental in completing this work. His encouragement and challenges pushed me to overcome obstacles and strive for excellence.*

Furthermore, I express my gratitude to my co-director, ***Prof. Dr. Celso Augusto Guimarães Santos*** *from the Federal University of Paraíba, João Pessoa, Brazil, whose insights and contributions greatly enriched this research.*

I am also thankful to my friends Ouarghi Zakaria, Legraa Bilal, Rasselkaf Ibtissam, and Mammeri Idriss, Habbel Mounir, Farsi Fatima Zahra, Boucham Khouloud, and Youcef Mohamed Sahnoun for their support who stood by me throughout the years.

Special thanks to Mr. Benouda Hamid, the head of the hydraulic department, for his encouragement and guidance. Additionally, I cannot forget to mention the invaluable support of our beloved secretary Berkouk Amina, who has been like a second mother to us, providing unwavering care and support.

Finally, I extend my thanks to my family in Tebessa and Chlef, as well as the entire Touba family, for their encouragement and prayers. This thesis is dedicated to my grandfather, who passed away before its completion, with heartfelt love and remembrance.

Thank you all.

Dedication

This Modest work is especially dedicated to:

My dear mother Lazaar Meriem, my reason for living, as a testimony of my gratitude for her patience, love, and sacrifices.

My dear father Djamel, for his love and dedication.

To you, my parents: I say thank you for making me who I am today. No Dedication can fully express my respect, consideration, and great admiration for you. May this work demonstrate my affection and deep love.

My dear sisters, Rima and Chaima, who place great importance on my success. May Allah keep you for me.

To you, my princesses : I wish you a life full of happiness, joy, and success.

Dr. Zerouali Bilal, who showed me the right path by reminding me that self-made and determined people will always end up succeeding in life, even me.

My friends, teachers, and those who have helped me, May Allah repay you for all your blessings.

Finally, to all those I love and who love me, I dedicate this Thesis.

Touba wafa.

ملخص

تعتبر ادوات التنبؤ بتدفق مجرى الاودية باستعمال تعلم الالة والتعلم العميق.ومن بين الأدوات المستخدمة للتخطيط المستدام في إدارة الموارد المائية. في هذه الدراسة، نقوم بتقييم فعالية نماذج متعددة الطبقات(MLP) ، والذاكرة القصيرة والطويلة المدى(LSTM) ، و XGBoostفي تنبؤ التصريف اليومي باستخدام البيانات من مهمة قياس الأمطار الاستوائية (TRMM) في حوض شليف في شمال الجزائر. يشمل تقديرنا، استنادًا إلى جذر متوسط المربعات الخطية(RMSE) ، مجموعة من سيناريوهات الاختبار لـ 9 نماذج. تُظهر نتائجنا أن MLP يؤدي بشكل تنافسي، حيث يحقق أدنى RMSE في السيناريو M8 (RMSE = 2.485) عند استخدام بيانات .TRMM بالإضافة إلى ذلك، عند مقارنتها بالبيانات الموجودة في الموقع، تظهر كل من LSTM و MLPأداءً معقولًا. أخيرًا، يبرز هذا تميز LSTM في استخدام بيانات الأمطار المستمدة من الأقمار الصناعية للتنبؤ الدقيق بالتصريف اليومي.

الكلمات المفتاحية: تنبؤ التصريف، MLP، XGBOOST، LSTM، بياناتTRMM ، RMSE، تصريف يومي.

Résumé

Les outils de prévision du débit des cours d'eau utilisant l'apprentissage automatique et l'apprentissage profond sont envisagés comme des éléments essentiels pour la planification durable dans la gestion des ressources en eau. Cette étude évalue l'efficacité des modèles Perceptron Multicouche (MLP), Long Short-Term Memory (LSTM) et XGBoost dans la prédiction des débits journaliers en utilisant des données de la Mission de Mesure des Précipitations Tropicales (TRMM) dans le bassin de la Cheliff, au nord de l'Algérie. Notre évaluation, basée sur l'Erreur Quadratique Moyenne (RMSE), inclut une série de scénarios impliquant 9 modèles différents. Nos résultats indiquent que le MLP offre des performances compétitives, atteignant le RMSE le plus bas dans le scénario M8 (RMSE = 2.485) lorsqu'il utilise des données TRMM. De plus, en comparaison avec les données in-situ, les modèles LSTM et MLP montrent tous deux une performance raisonnable. En conclusion, cette étude met en évidence l'efficacité du LSTM dans l'utilisation des données de précipitations dérivées de satellites pour une prédiction précise des débits journaliers.

Mots-clés: Prédiction des débits, , MLP, XGBoost, LSTM, données TRMM, RMSE, débits journaliers,

Abstract

Predicting tools for river flow using machine learning and deep learning are considered essential for sustainable planning in water resource management. This study evaluates the effectiveness of Multilayer Perceptron (MLP), Long Short-Term Memory (LSTM), and XGBoost models in predicting daily flows using data from the Tropical Rainfall Measuring Mission (TRMM) in the Cheliff basin in northern Algeria. Our assessment, based on the Root Mean Square Error (RMSE), includes a series of scenarios involving 9 different models. Our results show that the MLP performs competitively, achieving the lowest RMSE in scenario M8 (RMSE = 2.485) when using TRMM data. Moreover, in comparison with in-situ data, both LSTM and MLP models demonstrate reasonable performance. In conclusion, this study highlights the effectiveness of LSTM in using satellite-derived precipitation data for accurate daily flow prediction.

Keywords: Flow prediction, MLP, XGBoost, LSTM, TRMM data, RMSE, daily flows.

List of Abbreviations

ACF: Autocorrelation Function.

ANRH: Agence National des Ressources Hydrauliques=Agency for Hydraulic Ressources.

ANFIS: Adaptive Neuro-Fuzzy Inference System.

ANN: Artificial Neutral Network**.**

BP : Back Propagation.

CIMP5: Coupled Model Intercomparison Project Phase 5.

CERES: Clouds &Earth's Radiant Energy System.

CV: The coefficient of variation.

DL: Deep learning.

EDLM: Ensemble Deep Learning Models.

EANN: Emotional Artificial Neural Network.

FFNN: Feedforward Neural Network.

GR4J: Rural Engineering with 4 Daily Parameters = Génie rural a 4 parameters journaliere.

GIS: The Geographic Information Systems.

GOES: Geostationary Operational Environmental Satellite.

GA: Genetic algorithm.

GRNN: The Generalised Regression Neural Network.

GPR: Gaussian Process Regression**.**

HEC – HMS: Hydrologic Engineering Center Hydrologic Modeling System.

HBV: Hydrologiska Buyråns Vattenbalan Savdeling.

HHO: Harris Hawk Optimisation Algorithm.

IHDM: Institute of Hydrology Distributed Model.

JAXA: The Japan Aerospace Exploration Agency.

KNN: K-Nearest Neighbors.

KELM: Kernel Extreme learning Machine.

LSTM: Long Short Term Memory.

LIDAR: Light Detection and Ranging.

LSI: Lighting Imaging Sensor.

ML: Machine Learning.

MLP: Multi-Layer Perceptron.

MIKE-SHE: Mike – System Hydrologique European.

MLR: Multiple-Linear Regression.

Meteo sat: Meteorological Satellite.

M5: M5 model Tree.

MLP-PSO: Multilayer Perceptron Optimized by Particle Swarm Optimization.

MAE: Mean absolute Error.

MARS : Multivariate Adaptive Regression Spline.

NWSRFS: The National Weather Service River Forecasting System.

NASA: The National Aeronautics and Space Administration.

NOAA: The National Oceanic and Atmospheric Administration.

NSE: Nash Sutcliffe criterion.

PACF: The Partial Autocorrelation Function.

ONM: National Meteorological Office.

RMSE: Root Mean Squared error.

RNN: Recurrent Neural Network.

RFR: Random Forest Regression.

R-R: Rainfall – Runoff.

RS: Remote Sensing.

R: Pearson Correlation Coefficient.

R^2: correlation coefficient.

SVM: Support Vector Machine.

SVR: Support Vector Regression.

SCS: the Soil Conservation Service Curve Number.

SWAT: The Soil and Water Assessment Tool.

STD: The standard deviation.

SD-GRU: Seasonal Decomposition-Based Deep Gated Recurrent Unit.

SVR-rbf: Support Vector Regression with the radial kernel function.

SVR-poly: Support Vector Regression with polynomial kernel function.

TRMM: Tropical Rainfall Measuring Mission.

TM: Thematic Mapper.

UH: Unit Hydrograph.

VIC: The Variable infiltration Capacity.

VMD: The Variational Model Decomposition.

Var: The Variance.

TMI: TRMM Microwave imager.

TVM: Time Varying Models.

XGBoost: Extreme Gradient Boosting.

WANN: wavelet-coupled artificial neural network.

WANFIS: wavelet-coupled adaptive neuro-fuzzy inference system.

List of Figures

Chapter I: General Introduction

Chapter II: Literature Review

Chapter III: Study Area and Methodology

Chapter IV: Results and Discussion

List of tables

Chapter II: Literature Review

Chapter III: Study Area and Methodology

Chapter IV: Results and Discussion

Table of contents

Chapter III: Study Area and Methodology

Chapter IV: Results and Discussion

Chapter I: General Introduction

Chapter I: General Introduction

I.1.Introduction

Rainfall-runoff modeling holds significant importance in hydrological sciences as it provides a key vision into the intricate interplay of the water cycle and its impact on socio-economic factors (Iamampai et al. **2024;** Adnan et al. **2023**; Aoulmi et al. **2021**). Water is an enduring factor in human progress and plays a vital role in the natural environment, serving as a primary resource for various plants and animals. However, human activities, compounded by climate change, present significant challenges (Zerouali et al. **2021**). The international scientific community is particularly concerned about the impact on regions, such as Africa. The relationship between rainfall and runoff is a complex hydrological phenomenon. Runoff, a key element of the water cycle, has long been a central focus in hydrology. It is influenced by multiple factors including precipitation, evaporation, solar radiation, and circulation patterns. This process displays significant spatial and temporal variations, lacking smoothness in its behavior. The understanding and modeling of R-R dynamics are crucial for addressing the challenges posed by climate change and ensuring sustainable water resource management.

The impact of climate change and human activities has increased the variability and disrupted the predictability of runoff patterns, leading to nonstationarity, it signifies that the statistical properties of the system under Runoff patterns are not constant over time. In addition, statistical nonconformity. Implies a deviation from expected norms. The increased runoff variability has resulted in more frequent extreme climatic events, such as prolonged warming of ocean surface temperatures in the central and eastern equatorial Pacific. Causing significant consequences like droughts and inundation. Droughts can be considered major environmental disasters, resulting in drinking water shortages (Salehi. **2022**) for both humans and livestock, reducing agricultural production, and increasing economic costs. Furthermore, floods induced by climate change have intensified over the years, causing devastating destruction including crop damage, destruction of agricultural infrastructure, and significant population displacement (Lyude et al.**2021**).

Accurately predicting daily runoff is crucial within the hydrological cycle, serving as a fundamental tool for improving watershed management (Zhanget al., **2018**). This capability

enables water resource managers to formulate effective strategies. Minimizing losses in public and private property, human lives, and physical assets, while mitigating health and ecological risks. Accurate daily Runoff prediction is an essential tool for long-term water resource management. In addition, it contributes to the prediction of extreme floods and dry periods and optimizing hydroelectric power production. Allocating water for farming, engineering hydraulic infrastructure (Wei et al.**2023**), and efficiently managing reservoirs, are the main research topics in accurately predicting runoff, including, dam design, water resource allocation plans, catchment area management, and flood management. It also it provides valuable information for decision-making and planning in various fields such as Flood analysis, supporting the design and evaluation of flood control measures and infrastructure.

Runoff prediction involves the utilization of two primary types of models: physically-based and data-driven. Physically based models simulate runoff processes through hydrological principles and equations, requiring numerous parameters and calibration, potentially limiting their capacity to capture the nonlinear and dynamic behavior of runoff (Moosavi et al. **2022**). Despite advancements, challenges persist in existing runoff prediction methods, particularly in representing the complexities of runoff dynamics using physically based models. On the other hand, data-driven models employ machine learning to discern the relationship between input and output data. However, these models may encounter challenges such as overfitting, generalization issues, and interpretational difficulties. Ensuring accurate and sufficient input data is crucial for runoff prediction, including details about weather conditions, watershed features, and historical runoff patterns. A comprehensive understanding of past climatic conditions is essential for predicting various elements of the water cycle. Accurate runoff prediction models become particularly crucial in tropical regions, where drought-related challenges are prominent and directly linked to observed climate changes (Qiu et al. **2023**). Predicting runoff is challenging because the data changes in ways that are not easy to understand. This challenge arises from temporal variations in data that defy simple patterns, complicating analysis and prediction.

Rainfall and Runoff data are crucial for various environmental applications, but their availability poses challenges, with low resolution and data limitation being the main issues in flood analysis resulting in inaccurate flood predictions. Consequently, the decision for flood disaster mitigation tends to be ineffective. Currently, satellite-estimated rainfall data is increasingly playing a vital and important role in accurate predictions. TRMM, a collaborative

effort between NASA and JAXA, operated from late 1997 to 2015 **(**Senior Review Proposal **2011**). It monitored tropical and subtropical rainfall to study interactions between the atmosphere and oceans in these regions. Its main instruments, include the Precipitation Radar (PR), TRMM Microwave Imager (TMI), Visible Infrared Scanner (VIRS), Clouds & Earth's Radiant Energy System (CERES), and Lightning Imaging Sensor (LSI), were incorporated into the TRMM Combined Instrument (TCI) calibration dataset. These instruments contributed to the TRMM Multi-satellite Precipitation Analysis (TMPA). Providing essential products for climate research, TMPA offers monthly precipitation averages and daily averages at a 0.25° spatial resolution from 50°N to 50°S for the period 1998-2015. More than 14 years of TRMM data have been collected. TRMM data is vital for water management and mitigating risks associated with water flow, offering detailed information about rainfall distribution. This data is utilized in studying climate, the atmosphere, the environment, and managing watersheds.

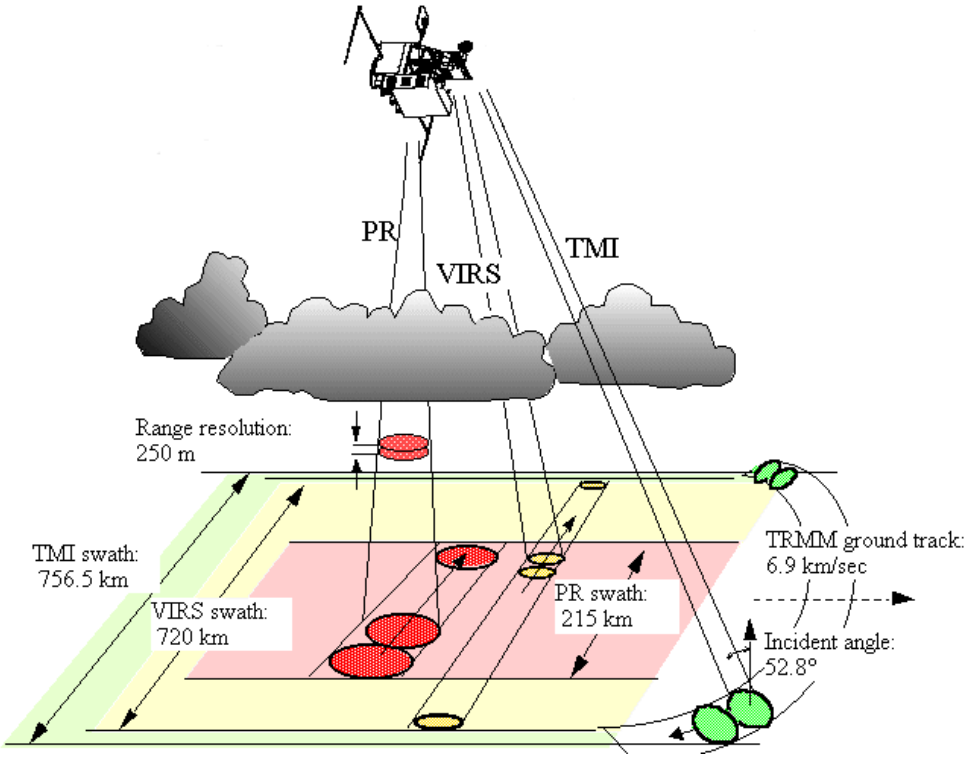

Figure I.1: Schematic representation of rainfall measurement using the TRMM sensor suite. (**Image source:** JAXA)

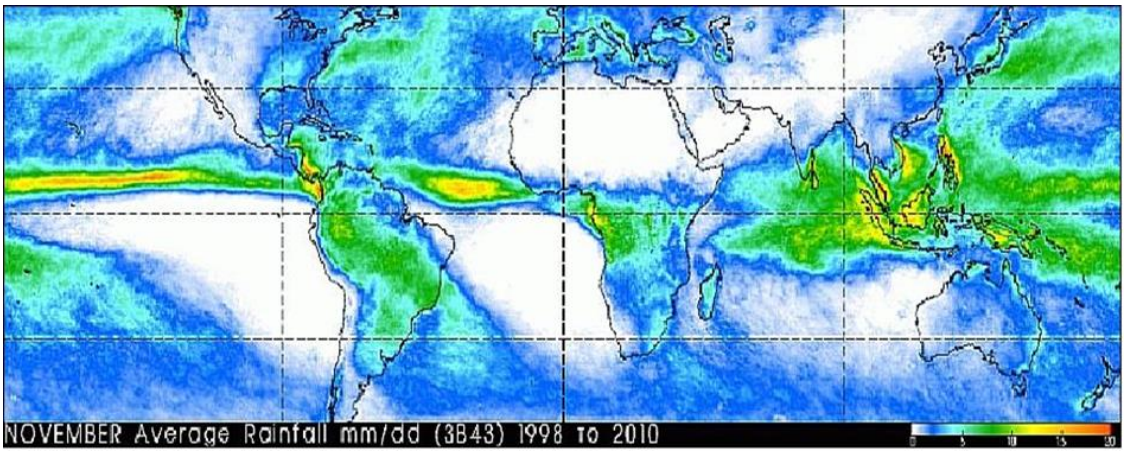

Figure I.2: Example image displaying 7-day accumulated global rainfall data.

(**Image source:** NASA)

The escalating threat of global warming and the increasing limitations on water access in various regions pose significant challenges to global hydrological sustainability (Mohammadi et al. **2021**). Consequently, there is a pressing need to enhance the current perspective from which hydrological studies are conducted worldwide, particularly in quantifying and comprehending water cycle modeling. so In recent decades, there was been notable progress in the theoretical understanding of machine learning (ML) algorithms for addressing engineering challenges, along with their practical application. In the field of hydrology, ML has been employed to gain a better understanding of hydrological complexities these algorithms have shown promise in addressing various engineering challenges. ML, with its capacity to learn from data and make informed decisions, Has become particularly crucial as human activities and climate change impact runoff patterns, introducing nonstationarity and nonconforming states in hydrological systems. The integration of ML into modeling has proven to be essential for effectively managing the inherent uncertainties and nonlinearity in hydrological systems. Hybrid models, which combine the strengths of physics-based models with ML, are emerging as a promising approach, offering a more comprehensive representation of hydrological processes by leveraging the interpretability of traditional models and the predictive power of ML. Uncertainty quantification holds a paramount importance in hydrology due to the natural variability and complexity of systems. ML serves as a means to estimate and communicate uncertainties in predictions (Nourani et al. **2011, 2021;** Mohammadi et al. **2020**), providing valuable information for decision-makers As ML continues to advance its integration into hydrological modeling offers new possibilities for improved accuracy, efficiency, and adaptability in predicting and managing water resources.

However, a subtle strategy is essential, considering the specific challenges and requirements of hydrological systems. Ensuring that developed models are not only accurate but also reliable in real-world applications. Machine learning proves to be a powerful tool in increasing the accuracy of runoff prediction within hydrological systems. Its ability to learn intricate patterns from large and diverse datasets significantly contributes to improving predictive models. ML adapts to changing hydrological systems by capturing critical runoff variables through automated feature extraction and integrating diverse data sources. It excels in handling uncertainty, offering decision-makers valuable insights and allowing for continuous refinement of predictions as data increases or our understanding of hydrological systems advances. In the context of TRMM, the integration of machine learning holds particular significance. Machine learning (ML) has the potential to elevate the accuracy of TRMM's runoff predictions within hydrological systems. Its adeptness at learning intricate patterns from extensive and diverse datasets significantly contributes to the enhancement of predictive models. ML exhibits adaptability in response to changing hydrological systems, capturing crucial runoff variables through automated feature extraction and integrating diverse data sources. This proficiency in handling uncertainty provides decision-makers with valuable insights, enabling a continuous refinement of predictions as data increases or our understanding of hydrological systems advances.

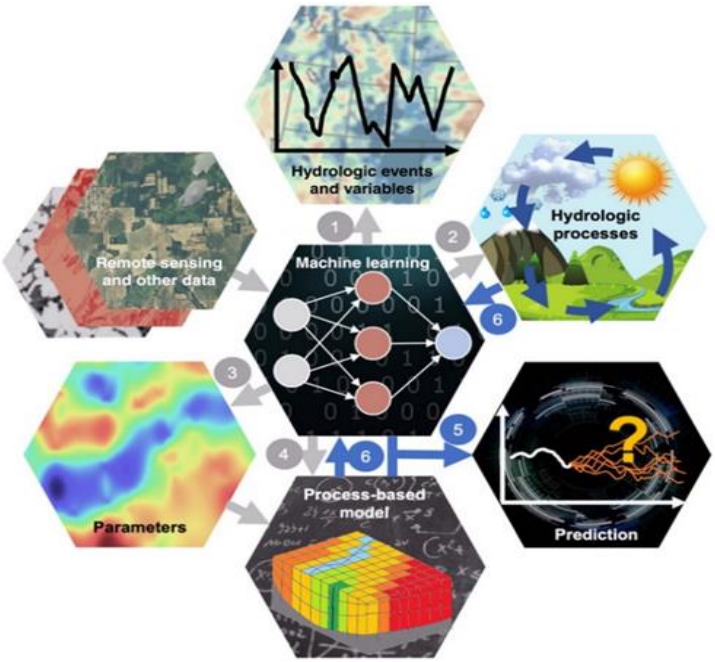

Figure I.3: Integration of machine learning in hydrologic applications

(**Image source:** https://wires.onlinelibrary.wiley.com/doi/10.1002/wat2.1533)

I.2. Problematic

As runoff stands as a pivotal parameter in hydrology, akin to other disciplines delving into the intricacies of natural systems, the realm of hydrology, encompassing rainfall-runoff modeling and the broader spectrum of central hydrology, grapples with the challenge of unraveling the complexities inherent in the systems under scrutiny. The evolution and expansion of rainfall-runoff models trace back to the 1960s. In our research, we concentrate on deploying an intelligent system, leveraging a multilayer perceptron (a subtype of the artificial neural network, ANN), XGBoost, and LSTM networks. These algorithms have been selected based on their demonstrated efficacy and robustness in fine-tuning hydrological models. Furthermore, we integrate TRMM data into our intelligent framework to compare its performance against actual rainfall data. This comparative analysis is geared towards augmenting the precision and prognostic capabilities of our hydrological models.

I.3. Objective of the Research

This study aims to assess the effectiveness of integrating Tropical Rainfall Measuring Mission (TRMM) data with advanced intelligent systems to improve Runoff prediction accuracy. It involves comparing TRMM-derived precipitation data with hydrological data Utilizing machine learning algorithms and artificial neural networks, the study aims to refine TRMM data and improve its reliability. By incorporating these improved precipitation inputs, the precision of daily runoff modeling will be evaluated. Model performance will be comprehensively assessed against observed runoff data to quantify improvements achieved through the integration of TRMM data and intelligent systems.

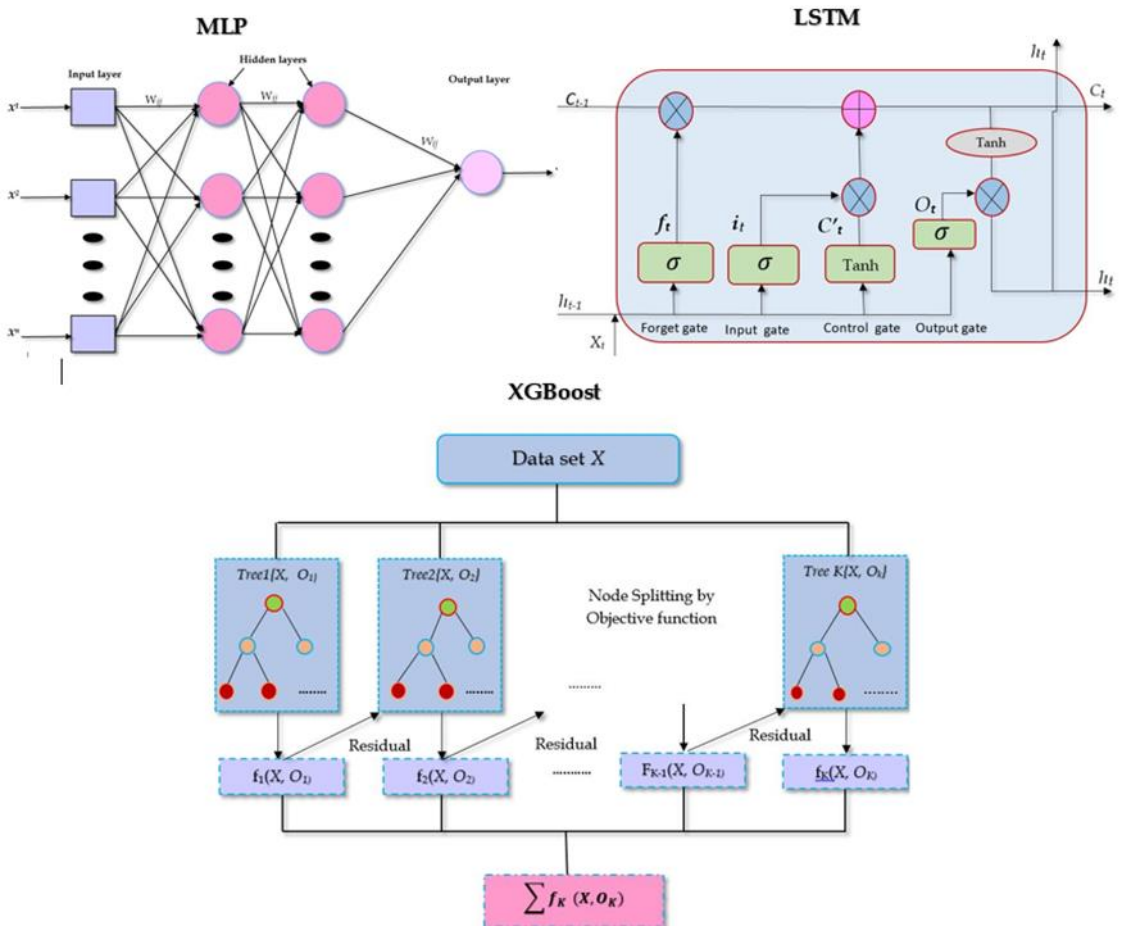

Figure I.4: The schematic diagram represents the proposed algorithm in this study.

I.4.Content of the thesis

In order to achieve the proposed objectives, the thesis is divided into four chapters, preceded by a general introduction and followed by a general conclusion, the arrangement is as follows:

Chapter 01: This chapter includes general information on modeling, the introduction explains with a presentation of the daily runoff prediction challenge. The Tropical Rainfall Mission (TRMM) is introduced, emphasizing its relevance to hydrology. The application of machine learning in runoff prediction is also introduced. This chapter briefly outlines the objectives and highlights the importance of integrating TRMM and machine learning to enhance the accuracy of daily runoff prediction.

Chapter 02: This chapter presents the existing literature on daily runoff prediction methods, examining studies that utilize TRMM for hydrological applications. It offers a concise overview of machine learning techniques in hydrological modeling and identifies gaps and

opportunities in combining TRMM and machine learning for runoff prediction. The chapter aims to lay the groundwork for a novel approach by assessing the strengths, limitations, and untapped potential in this intersection.

Chapter 03: This chapter presents the methodology, beginning with a simple explanation of how TRMM data is integrated into the modeling framework. Subsequently, discourse about the chosen machine learning algorithms and their parameters. Justification for the selected methodology is provided, emphasizing the synergistic relationship between TRMM and machine learning to ensure a robust approach.

Chapter 04: In this chapter, we will present, analyze, and discuss results obtained through the combined TRMM and machine learning approach. A comparative analysis with real data offers understanding of the novel approach's effectiveness. The discussion section addresses the strengths, limitations, and implications of the integrated model for TRMM and machine learning.

Methodology

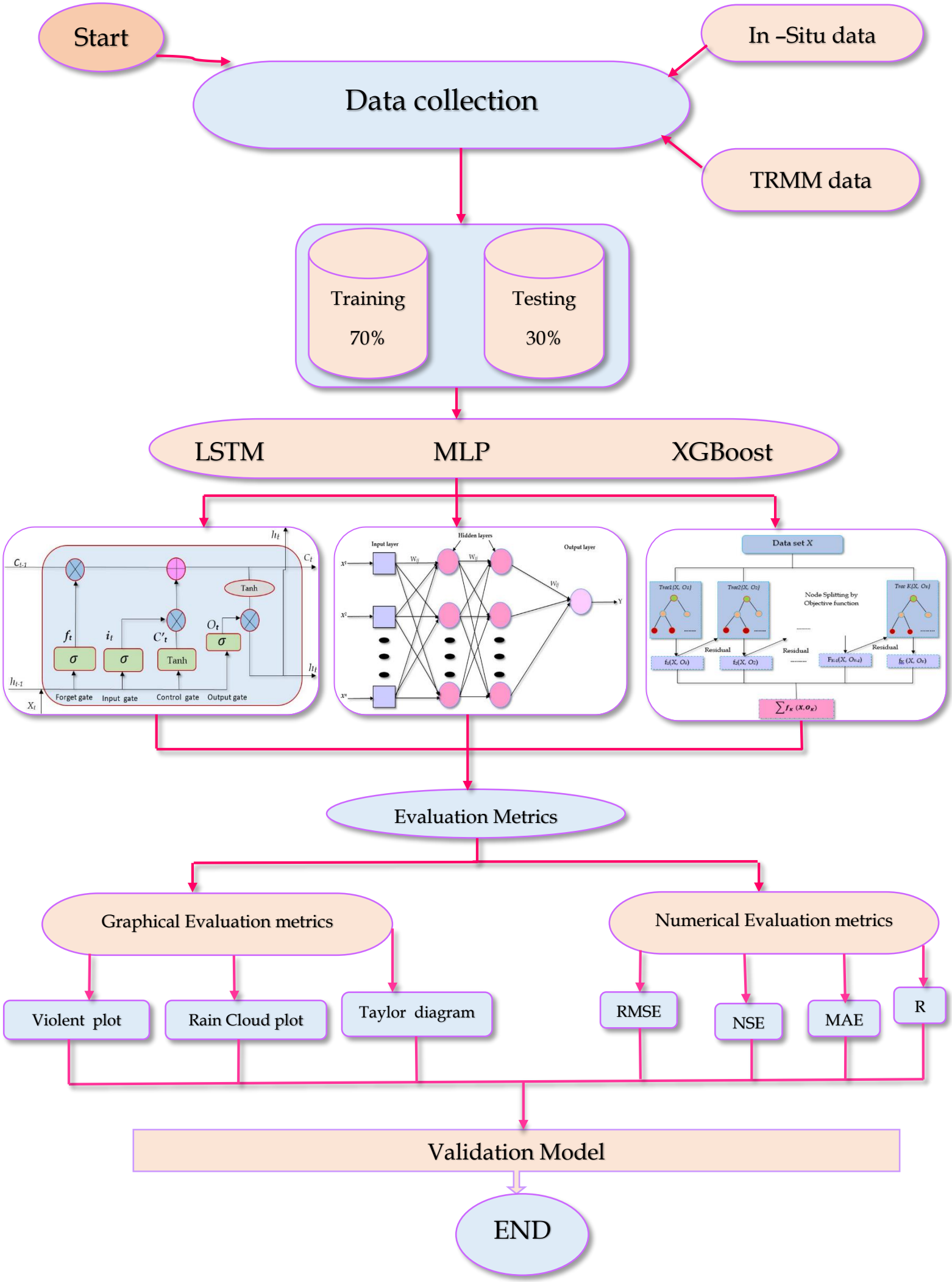

Chapter II: Literature Review

Chapter II: Literature review

II.1. Introduction

This chapter intends to comprehensively review the existing literature on runoff prediction, including traditional methods, advancements in remote sensing, integration of machine learning, and utilization of TRMM data. It provides visions into the historical context, methodologies, and limitations of hydrological modeling, highlighting the necessity of innovative approaches such as integrating remote sensing and machine learning. Through analysis of previous studies and emerging trends, this review identifies gaps in current understanding, laying the groundwork for the theoretical framework guiding the research in this study.

II.2. Introduction to runoff prediction models

Runoff prediction models are essential tools in hydrology because they can estimate when and how much water will flow from a catchment region area or watershed into a river. The term "runoff" describes the amount of precipitation that flows over the surface of land through drainage networks instead of infiltrating into the soil or evaporating into the atmosphere. These models use mathematical formulas and algorithms that take into account topography, precipitation, land cover, soil properties, and other variables to help understand the dynamics of water runoff across different geographic locations. There are various types of runoff prediction models, including the widely used SWAT model, IHDM, and others (E**,** **1988**) Hydrologists and water resource professionals rely on these models to predict and plan for potential flooding, as well as to assess the impact of land use changes on runoff patterns.

Because runoff prediction models offer valuable insights into the dynamic connections between temperature changes, precipitation patterns, and the behavior of water runoff over time, they become essential tools in climate change research. Scientists trying to understand how the dynamics of water movement are changing in response to climatic variability rely heavily on these models, commonly known as runoff. These models improve the predictive accuracy of their predictions by including real-time data, such as the present weather, together with sophisticated modeling approaches. For instance, these models assist in anticipating higher risks of floods in areas where climate change has resulted in increasing rainfall intensity. Additionally, they are essential in evaluating the effects of temperature changes, such as faster snowmelt in mountainous regions, which helps scientists analyze the downstream effects on water supply and possible flood risks. The development and

application of runoff prediction models significantly enhance our ability to comprehend and manage the hydrological cycle, ensuring the efficient utilization and preservation of water resources in a changing environment.

II.2.1. History of runoff prediction

Runoff prediction has a long history that spans centuries and represents the development of scientific methods and technology. Hydrologists initially estimated surface runoff using scant data and simple computing methods. The Rational Method, created by Thomas Mulvaney in 1851 and used to calculate the peak discharge in a drainage basin, was one of the first commonly used techniques. It used a runoff coefficient and the intensity of rainfall in the drainage area, and a runoff coefficient to determine the peak discharge in a drainage A graphical method for predicting the quantity of runoff basin was developed as a result of extensive research into the coefficient governing the relationship between rainfall and runoff (Asadieh B et al., **2016**). The graphical technique uses a sequence of graphs showing antecedent precipitation, week of the year, soil water retention index, and precipitation in the past six hours to calculate the amount of runoff. This technique is still used in the conceptual model, NWSRFS (Sitterson, **2018)**.

Based on the superposition principle, the unit hydrograph concept was developed to represent how a catchment might react to a storm event. This development made it easier to separate streamflow from storm event runoff and base flow. Runoff models have evolved with improved computational power and a better comprehension of hydrological processes. These models include distributed parameter models with physical foundations, conceptual models, and empirical models. Notable models including the VIC, Mike SHE, PSIHMS, and KINEROS are examples that are discussed in the literature. Utilizing the superposition principle, the unit hydrograph idea was introduced recently in runoff forecast to better understand the watershed response to storm events **(**Lettenmaier et al. **1999)** (Beven et al. **2012**)**,** (Todiniet al. **1988**),(Xu et al. **2002**). Separating baseflow and storm event runoff from streamflow has been made possible by this idea. Runoff models have changed significantly as a result of improved computational power and a better understanding of hydrological processes. The internal processes included in the black box method were able to be separated into several conceptual or empirical processes through the use of computers and computer modeling. Still, system states like soil wetness were merely estimated states inside the black box process at that point in the models' development (Engman, **1986**).

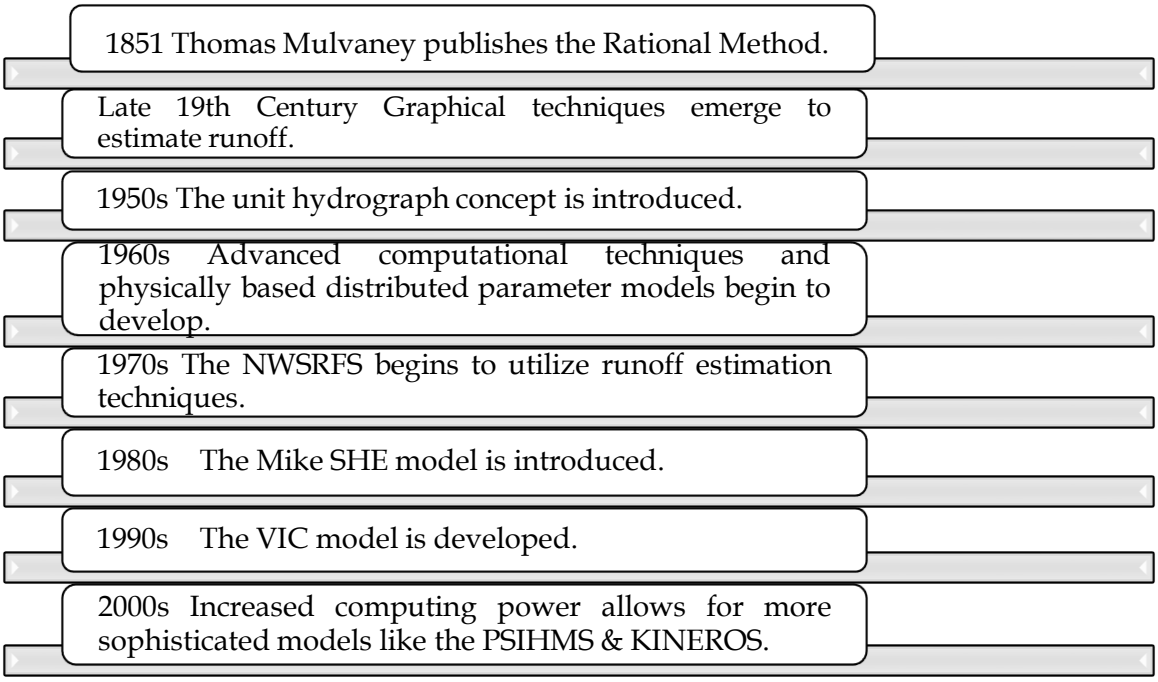

Figure II.1: The History of runoff prediction over the centuries.

Overall, the history of runoff prediction is varied and shows the development of scientific methods and technical breakthroughs over many decades. Modern approaches use sophisticated computational models to estimate runoff with better precision and accuracy than earlier methods, which depended on limited data and simple computational procedures

II.2.2. Runoff modeling

There are many interrelated parts to the hydrological cycle, and runoff is essential in tying precipitation and river flow together. When some precipitation crosses the surface of the ground and enters surface waters like rivers and streams rather than penetrating into the soil, this is known as surface runoff **(**Perlmane, **2016**). In order to display water resources and solve issues with quality and quantity, such as flood forecasting and daily or monthly runoff prediction, it is imperative that the amount of water flowing into stream systems be controlled (Koknoen et al.**2001**). In order to estimate water availability and changes over time, runoff modeling is utilized to understand watershed yields and responses (Vaze et al.**2012**). These models aid in visualizing the effects of modifications to past surface, vegetation, and climatic events on water systems. According to Devi et al. (**2015**), runoff models consist of equations that help determine how much rainfall turns into runoff based on several watershed-specific characteristics. Since surface runoff is a complex computation involving many interconnected factors, modeling it can be challenging. Models can be categorized in various ways, and not

all models fit into a single category since they were created for different purposes (Singh et al.**1995**). Different modeling approaches are used, including empirical, conceptual, and physically based models, which can be further classified based on spatial resolution, input/output type, and model simplicity. Models can also be classified based on the spatial interpretation of the model's catchment area, leading to the division into lumped, semi-distributed, and distributed models. The choice of a rainfall-runoff model depends on the purpose of the modeling, such as understanding and answering specific questions about the hydrological process, assessing the frequency of runoff events, or estimating runoff yield for management purposes (Vaze, **2012**). Identifying the priorities of modeling and accounting for the limitations of data availability, time, and budget helps narrow the choices and ensures that the model is best suited for the intended purpose.

II.2.3. Overview of traditional methods and models for daily runoff prediction

Daily runoff is a fundamental aspect of hydrology and over the years. Various methods and models have been developed to estimate daily runoff, reaching from traditional empirical techniques to more advanced computational approaches. Traditional methods used in daily runoff prediction involve a variety of approaches including both data–driven and physically based models and these methods have evolved to enhance prediction accuracy and effectiveness over time. Here below a table summarizes all the three traditional methods **Table II.1**.

Table II.1: Detailed description of conceptual, physical process-based and empirical models. (Jehanzaib et al, 2020).

Categories	Emprical or data driven models	Conceptual models	Physical process based models
Characteristics	**1.** Data based or metric model. **2**. Involves mathematical equations. **3**. Cannot be generated to other catchments.	**1.** Parametric or grey box models. **2.** Require large hydro-meteorological data. **3.** Simple and can be easily implemented on computers.	**1.** Mechanistic or white box model. **2.** Based on spatial distribution. **3.** Complex model and require human expertise.
Models	SCS-CN ANN,UH	HBV,TANK,GR4J	TOPMODEL SWMM WATFLOOD
Strengths	**1**.Small number of Parameters needed. **2.** Limited data Requirement. **3.** Can be used in Ungauged catchments.	**1**. Easy to calibrate. **2.** Calibrate with limited data. **3**. Need less computation.	**1.** Incorporates spatial And temporal variability. **2**. Very fine scale. **3**. Valid for wide range Of situations.
Weakness	**1.** No connection between physical catchment, input data distortion, Alternatively, Black box. **2.** High computation cost In addition, time.	**1.**Does not consider spatial variability Within catchment. **2**. Not recommended for large catchments	**1.** Suffer from scale Related problems. **2.** Large number of parameters and calibration needed; Site specific.
Related studies	Amaya, D et al 2022, analysis of four forested catchments on the Atlantic coastal plain using a modified SCS-CN rainfall-runoff model. (Amatya, 2022)	Jehanzaib, M.et al 2020 Investigating the impacts of climate change and human activities on hydrological Drought using non-stationary approaches. (Jehanzaib, 2020)	Bai, Y et al, 2019 Assessing the impact of climate change on flood events using HEC-HMS and CMIP5. Water Air Soli (Bai, 2019)

Empirical models, also known as data-driven models, use non-linear statistical connections between inputs and outputs. They are particularly effective for runoff prediction when additional outputs are unnecessary. However, these models do not provide a clear understanding of the underlying physical processes making them less interpretable compared to physical models (Khosravi et al.2013). Data–driven models are simple to use due to their minimal. Minimal parameters requirements, yet they lack a direct link to the essential physical mechanisms of the system they represent. (Dawson et al. 2001). One example of an empirical model is the SCS-Curve Number used in the Soil and Water Assessment Tool (SWAT).

Conceptual models aim to understand runoff processes by connecting simplified mechanisms within the hydrological process. They are based on reservoir storages and simplified equations of the physical hydrological process, which provide a conceptual idea of the behaviors in a catchment (Devi et al., **2015;** Vaze. **2012**). These models represent the water balance equation with the conversion of rainfall to runoff, as shown in **Figure II.2** (Vaze.**2012**). Each component in the water balance equation is estimated by mathematical equations that distribute the precipitation input data.

Physical models, also referred to as process-based or mechanical models, these model, rely on an understanding of the physics associated with the hydrological processes. (Vaze.**2012**). these models are guided by physically based equations that represent various parts of real hydrologic responses within a catchment. They utilize general physics laws and principles such as water balance equations, and conservation of mass and energy. One of the primary strengths of physical models lies in their ability to connect model parameters with physical catchment characteristics, improving their accuracy make it more. Spatial and temporal variations within the catchment are merged into physical models. Most physical models provide a three-dimensional view of the water exchange within the soil, surface, and air, as shown in **Figure II.2.** Examples of physical models include Visualizing Ecosystem Land Management Assessments (VELMA), MIKE System Hydrologique European (MIKE SHE)**.**

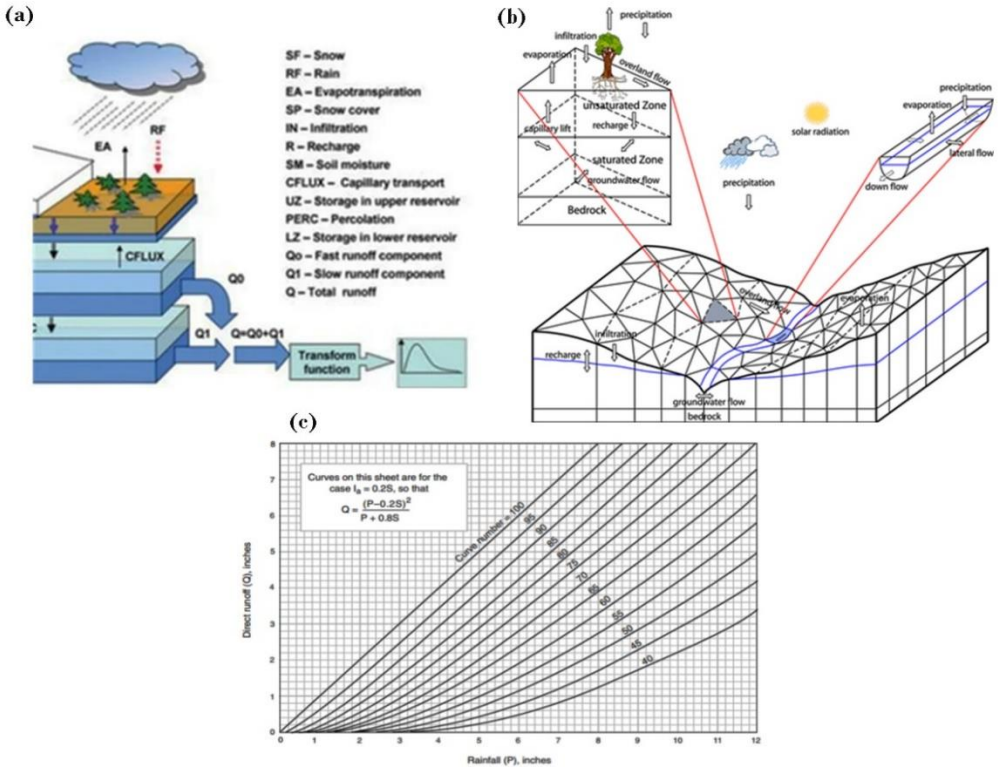

Figure II.2: Schematic diagram of rainfall-runoff models: (a) conceptual model, (b) physical process-based model, (c) empirical model. (**Image source:** Jehanzaib et al. 2020**).**

II.3.Remote sensing in hydrology

Hydrology is the scientific study of the occurrence, distribution, movement and its physical and chemical properties, along with its relationship with the living and material components of the environment. With challenges such as water scarcity, population growth, improved in quality of life and healthcare, increasing water consumption, and predicted food shortages in the upcoming decades, many countries will face a crisis, there is a pressing need to investigate various water resources and monitor the parameters influencing the hydrological cycle, utilizing sensors capable of estimating different patterns. According to Kairu (1982), remote sensing can be defined as "**the collection and interpretation of information about an object, a region or event without being in physical contact with the object**". Therefore, even a simple photograph, followed by the analysis of its contents, can be considered a form of remote sensing. Remote sensing has emerged as a valuable tool for estimating hydrological cycle parameters and observing hydrological state variables across extensive regions. It involves the process of driving surface parameters from measurements of the upwelling electromagnetic radiation from the land surface. Including both reflected solar and thermal infrared radiations (TIR), and microwave portions of the spectrum. Additionally,

imaging radars capture reflected microwave radiation. Reflected solar radiation used in hydrology for tasks such as snow mapping, vegetation/land cover analysis, and water quality studies. Meanwhile, thermal emission in the infrared is utilized for surface temperature analysis, and microwave is used for soil moisture and snow studies. Active microwave or radar technologies show promise due to their potential for high spatial resolution, however, the impact of surface roughness can pose challenges in extracting soil moisture information. Remote sensing observations play a crucial role in enhancing our understanding of these variables, particularly their spatial variations (Qanati et al.**2019**). A primary focus of remote sensing research in hydrology is the development of approaches to estimate hydro meteorological states and fluxes. Key state variables include land surface temperature, near-surface soil moisture, snow cover/water equivalent, water quality, landscape roughness, land use, and vegetation cover. The primary hydro meteorological fluxes include soil evaporation, plant transpiration (or evapotranspiration), and snowmelt runoff (Schmugge et al**. 2002**).

II.3.1.Types of remote sensing data

Geophysical datasets—in particular, remote sensing datasets—are being produced at an ever-increasing pace in the world we live in. Significant promise has been demonstrated by RS data and information in supplying crucial geographical data and parameters at an appropriate scale for application, in distributed hydrological models for water resource management. Remote sensing-based observations, in contrast to traditional methods that are usually reported through point measurements, provide spatial averages over pixels that are appropriate for distributed hydrological models. In addition, RS facilitates data access from remote areas, where data are typically sparse. RS technology uses electromagnetic spectrum, which includes wavelengths of different radiations reflected or emitted by objects. Although RS spectrum varies from 0.03 nm to 100 cm, observable, electromagnetic, and microwave spectra are commonly used in the recovery of hydrological parameters (Zhang et al. **2021**).

There are two main types of remote sensing: passive remote sensing and active remote sensing. Passive remote sensing systems rely on detecting natural energy emitted or reflected by the observed object, such as sunlight. These sensors can only detect energy when naturally occurring energy is present, which typically occurs during daylight when the sun illuminates the Earth. At night, when the sun is not shining, there is no available reflected energy. On the other hand, active microwave systems generate their own energy source for illumination. The sensor emits radiation directed toward the target to be under investigation. The sensor then detects and measures the radiation reflected from the target. One notable advantage of active

sensors is their ability to obtain measurements at any time, irrespective of the time of day or season. This flexibility allows active sensors to be employed for examining wavelengths that the sun may not adequately provide, such as microwaves.

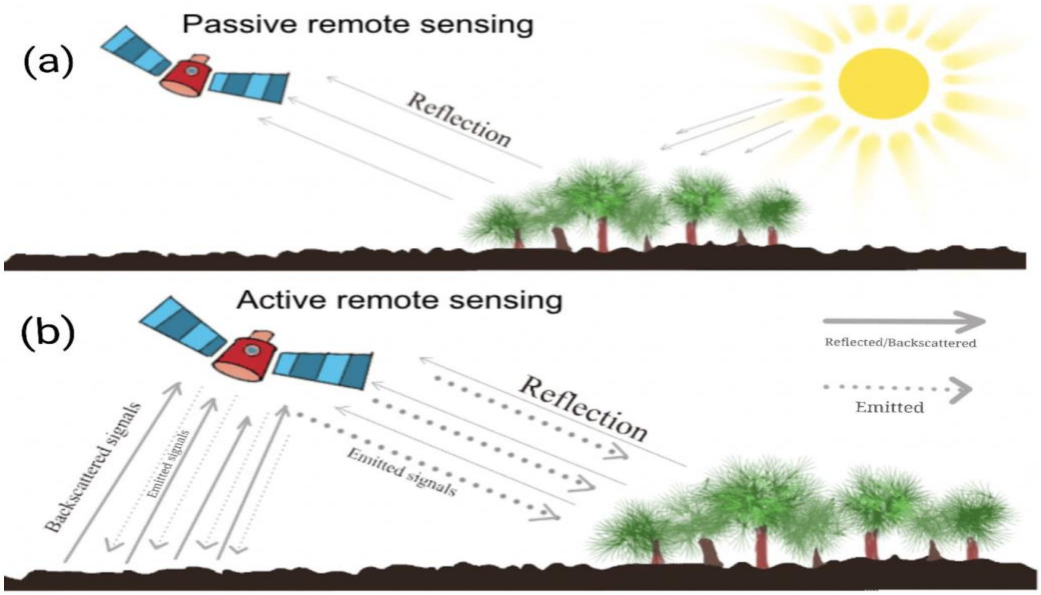

Figure II.3: (**a**) Passive remote sensing: the sensor receives information, (**b**) Active remote sensing: the sensor emits and receives information.

(**Image source :** janga et al.**2023**).

II.3.2. The integration remote sensing with hydrological models

As a science, hydrology mostly depends on observations and measurements. Hydrological research in catchments and regions with limited gauge coverage faces challenges when it comes to estimating runoff. Remote sensing (RS) data, which are globally available and include unique spatial and temporal characteristics, hold great potential in this regard. In areas with few stream flow measurements, hydrological models may be calibrated using remotely sensed data. the incorporation of geographic information systems (GIS) and remote sensing (RS) with hydrological models, as well as the gathering of data from satellite or aerial observations, in order to improve the resolution and accuracy of water cycle simulation. Numerous hydrological factors, including soil moisture, evapotranspiration, and runoff, can be obtained and included in models by Using RS data.

Remote sensing observation provides continuous data at both spatial and temporal scales, enabling the estimate of regional surface data quickly and widely (Stewart et al. **1993**; Sun et al. **2018**). Consequently, remote sensing data has been extensively applied and integrated with hydrological models (Beck et al. **2017**; Kittel et al. **2018**; Kumar et al. **2018**;

Wanders et al. **2014**). However, the quality of remote sensing data isn't always guaranteed (Andersen et al**. 2005;** Beck et al. **2017;** Liu et al**. 2016;** Sun et al. **2018**), and its accuracy varies across regions, which can have important regional consequences (Hijmans et al.**2005;** Wang et al**.2015**). Thus, the selection of datasets should be done carefully, aiming for the highest possible accuracy as inputs to hydrological models. Studies demonstrate that bias correction of input data improves runoff simulations under most conditions (Habib et al**.2014;** Li et al**., 2009;** Stisen et al. **2010;** Zhang et al. **2015**). Moreover, constraining multiple variables such as soil moisture and water storage data from remote sensing has been shown to improve the performance of hydrological models (Kundu et al. **2017;** Li et al**. 2016;** Pomeon et al. **2018;** Sutanudjaja et al. **2014;** Wanders et al**. 2014;** Yassin et al**. 2017**). However, most studies calibrate models against observed stream flow data, which is limited in poorly gauged regions**.** Zhang et al. (**2020**) proposed a remotely sensed actual evapotranspiration (RS-AET) calibration approach based on PML evapotranspiration products (PML-AET, a global evapotranspiration product based on improved Penman-Monteith-Leaning model) and showed its potential usefulness in relatively wet regions of Australia. Nevertheless, there are various limitations to the study by Zhang et al. (**2020**), which can be addressed. First, they did not consider the potential for improving the quality of the remote sensing actual evapotranspiration data used for hydrological model calibration. Second, the study used a lumped catchment-average rainfall-runoff modeling approach, neglecting the spatial continuity of remote sensing data. Third, the research did not explore the potential of combining remote sensing data on actual evapotranspiration with remote sensing data on water storage (Huang et al. **2020**). Hydrologists are particularly interested in remotely sensed data due to its wide spatial coverage and the frequency of measurements. An improved understanding of the hydrological cycle necessitates the measurement of time series data at a point, data varying over an area, and data, which do not change over the time scale of the modeling period. **Table II.2** shows some of the data types commonly used in hydrological models and classifies them by dimension and time dependency.

Table II.2: Examples of parameters in hydrology and water resources currently available from satellite (Kite et al. **1993**).

Variable	Satellite/Sensor	Wavelength	Resolution	Coverage	Sample reference
Snow Depth	GOES Nimbus 7	0.65 mm (visible)3 GHz	2 km	2 per hour	Donald et al, .**1990** Change et al, .**1982**
Precipitation	Meteosat	0.65 mm (Visible)	3 km	''	Pietronior et al, .**1989**
Spring Runoff	Nimbus 5	19 GHz	30 km	2 per hour	Wankiweiz ,**1989**
water depth	Landsat	0.48, 0.56, 0.66 µm (bands 1, 2, 3)	30 m	''	Hallada, **1984**
Snow covered area	NOAA	0.62, 10.80mm (bands 1 and 4)	1 km	2 per Day	Kite, **1989** ; Carroll & Baglio **1989**; Rango, **1980**

The use of RS in hydrological models can be categorized into three broad levels. The simplest level involves the use of RS imagery to identify items of interest such as snow-covered areas. The second level involves obtaining data such as land cover or other hydrological parameters through the interpretation and classification of remotely sensed data. This interpolation of satellite data is often used in combination with existing hydrological models such as the SCS watershed runoff model. The third level involves the use of digital data to estimate hydrological parameters directly. This is normally attained through the correlation of known hydrometric data with remotely sensed data. Estimates of soil moisture and precipitation have been obtained in this way (Schultz et al. **1993**). All three categories have been used successfully in hydrological applications with the second category being particularly well suited to hydrological models (Kite et al. **1996**).

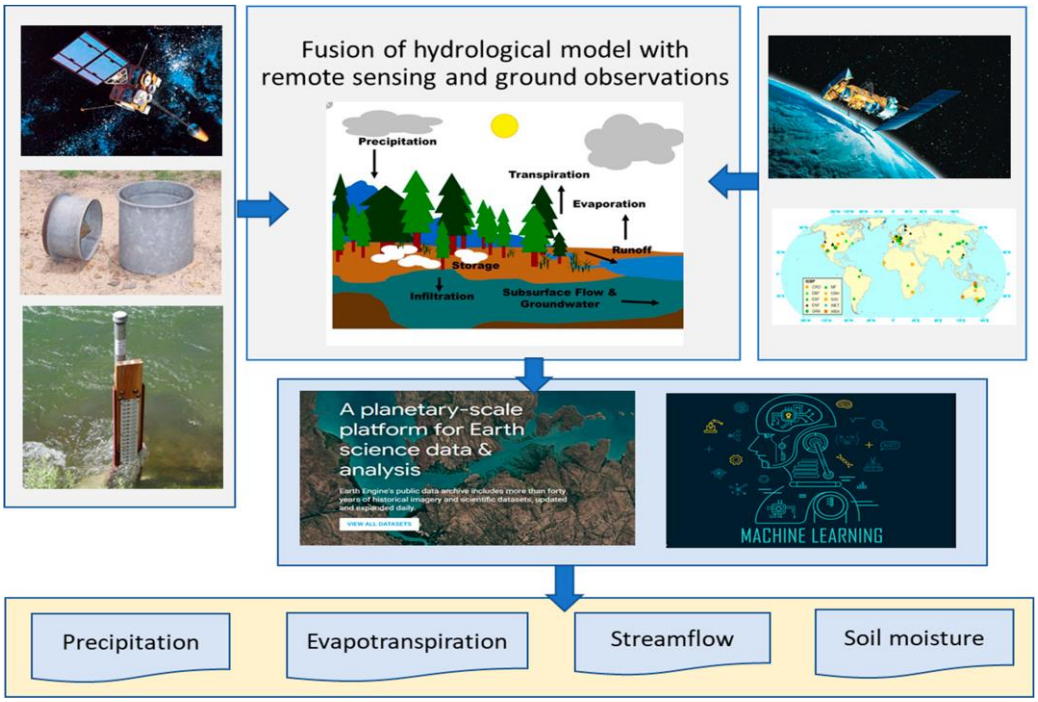

Figure II.4: Conceptualized summary of model and data fusion techniques for improving hydrological predictions. (**Image source:** Zhang et al. 2023).

II 3.3.TRMM in runoff prediction by using remote sensing

Remote sensing has been widely applied in many different hydrological and water resource applications. In particular, the TRMM satellite mission uses optical and microwave electromagnetic sensors to quantify precipitation in tropical and subtropical regions. Supplying precise rainfall data for a range of uses, such as hydrological modeling, TRMM has significantly influenced runoff prediction, a critical aspect of water resources management. Involving the estimation of water flow from land surfaces into rivers, lakes, and oceans. Accurate runoff predictions are essential for flood prediction, water supply planning, and environmental conservation. By integrating TRMM data with Remote sensing technologies, researchers have improved runoff prediction models by incorporating precise rainfall information, improving hydrological modeling, and enabling better water resource management strategies (Zhu et al. 2023). This integration has advanced our understanding of tropical rainfall dynamics, convective systems, and their impact on the hydrological cycle, highlighting the importance of TRMM data in increasing runoff prediction and hydrological research. Improving runoff prediction models is largely dependent on advanced Remote Sensing and GIS approaches, particularly the use of TRMM data. By estimating surface runoff based on several characteristics, these strategies help runoff prediction models become more accurate. In addition to helping with surface runoff estimation, RS and GIS technologies are

crucial in figuring out runoff coefficients, which enhances our comprehension and forecasting of surface runoff dynamics. Furthermore, by offering insightful information on model performance and selection, the combination of TRMM data with Remote Sensing (RS) technologies has greatly improved runoff prediction models and increased their accuracy. By using remote sensing data such as Synthetic Aperture Radar (SAR) and Landsat TM to map glacier units, we can consider their effects on terrain for more precise and refined runoff predictions. These applications emphasize the critical importance of advanced remote sensing techniques, particularly TRMM data, in improving the accuracy of runoff prediction models. This enhancement supports better hydrological modeling for more effective flood simulations and water resource management.

II.4.Machine learning in hydrological modeling: unveiling techniques and applications

Hydrological modeling relies heavily on machine learning, which functions as a bionics-based approach to problem-solving that imitates the workings of the human brain. It usually entails a number of mathematical transformations and operations carried out by computer programs in conjunction with contemporary electronic processors. The goal of improving the precision and dependability of hydrological variable forecasts in hydrological modeling has drawn a lot of interest (Niu et al. **2019**). Many models are unable to produce accurate forecasts because of runoff behavior and model instability, which includes extreme episodes in historical records (Oppel et al. **2020**). ML techniques have demonstrated a lot of promise recently for forecasting and simulating runoff (Yeditha et al. **2020**). Artificial Neural Networks, These techniques fall into three categories: decision trees and ensemble methods, support vector machines, Bayesian methods, and so on (Moosavi et al. **2018**)**.** In ML models, the association between hydrological cycle variables and runoff is examined directly without regard for the actual processes involved (Jehanzaib et al**.** **2022**) As a result, in recent years, researchers have concentrated on creating ML techniques for runoff modeling and flood prediction that are more reliable (Nourani et al. **2021**). These techniques are widely used in many areas related to water resources, such as stream flow forecasts, water quality modeling, and rainfall-runoff modeling. Compared to conventional physics-based models, machine learning (ML) models offer the advantage of improved predictive performance and require less work to construct and calibrate. In ways that traditional models might find difficult to accomplish, they have the ability to identify catchment similarities and create catchment-scale hypotheses. The shortcomings of machine learning models, such as their inability to be

explained and the requirement for careful consideration of parameter and data uncertainties, must be addressed, nevertheless. Scientific information can be used in machine learning algorithms to also be crucial for developing physically consistent models. These models aim to improve machine learning's prediction accuracy while ensuring consistency with fundamental hydrological principles. For instance, the Machine Learning Rainfall-Runoff Model Induction (ML-RR-MI) toolset utilizes genetic programming to develop lumped conceptual rainfall-runoff models. One important technique that uses machine-introduction knowledge augmentation to generate semi-distributed rainfall-runoff models without the requirement for human participation is the System Hydrologique Asiatique (MIKA-SHA). Over time, machine-learning approaches have progressed from basic feed-forward networks to more complex models that replicate hydrological processes. The most often used data science tools in hydrological modeling are fuzzy sets, support vector machines (SVM), and artificial neural networks (ANN) (Yaseen et al. **2015**). Each of these techniques has its strengths and weaknesses, Random Forests (RFs), Gradient Boosting Machines (GBMs), and even DL architectures like LSTM. These advancements increase our ability to model and understand hydrological systems. Recent applications of machine learning (ML) and deep learning (DL) models in catchment hydrology have the potential to improve runoff predictions because they are trained on large and highly variable data sets derived from multiple catchments (Kratzert et al. **2019;** Nearing et al. **2021**). These ML models' benefits and drawbacks are outlined in **Table II.3.**

Table II.3: Advantages and limitations of ML models (Jehanzaib et al.2022)

Model	Advantages	Disadvantages	Related studies
KNN	Capable of identifying past events.	It does not predict values greater than the range of historical observation.	Mohammadi, B et al 2020 Modeling daily reference evapotranspiration via a novel approach based on support vector Regression coupled with whale optimization algorithm. Agric. Water Manag.
ANN	Needs less formal statistical training.	Time consuming to train with traditional CPUs.	Wu, J.S. et al 2005 Artificial neural networks for forecasting watershed runoff and stream flows. J. Hydrol. Eng.
ANFIS	Hybrid models with the strength of ANN and fuzzy.	Low interpretability of learned information.	Sanikhani, H, et al, 2012 River flow estimation and forecasting by using two different adaptive neuron-fuzzy approaches. Water, Resour. Manag.
SVM	Easy to solve complex problems with appropriates kernel.	Fine-tuning of hyper parameters is difficult.	Samantaray, S.; et al, 2020 Estimation of runoff through BPNN and SVM in AgalpurWatershed. In Frontiers in Intelligent.

Many studies have investigated the use of machine learning in runoff prediction. For example, (Huang et al. 2022) used ANN to predict runoff in the Haihe River Basin in North China. Finding both outperformed traditional linear regression models, with SVM showing slightly better performance. In another study, (Kim et al. 2011**)** used decision trees and random forest algorithms for runoff prediction in the Yeongsan River basin in Korea. They found that random forest models outperformed decision trees for runoff prediction. While machine learning in hydrological modeling particularly in runoff prediction, shows promise, there are several challenges and limitations, Machine-learning models typically require large amounts

of data for training and validation. However, in hydrological modeling limitations in data availability, in areas with insufficient monitoring networks or data gaps. This scarcity can significantly affect the accuracy and generalizability, of the models. Increasing data collection can be one way to overcome these issues. Methode: to fill up data shortages, this entails using remote sensing techniques, initiating citizen science projects, and developing data assimilation strategies. Overfitting is a danger associated with machine learning models, which causes them to become too sensitive to noise or anomalies in the training set, and to perform poorly when applied to fresh data. Regularization strategies can assist reduce overfitting and enhance model performance. Examples of these strategies include employing cross-validation or including regularization terms in the loss function of the model. Moreover, Biases in the training set of data can affect machine-learning models. Measurement errors, data preparation techniques, and sampling biases are some of the causes of biases. It can be beneficial to follow strict data quality management guidelines and make use of representative, impartial datasets, to mitigate these issues.

II.5.Remote Sensing and Machine learning integration in hydrology

Remote sensing and machine learning play an important role in various applications across different fields. Within Hydrology they hold specific importance by improving the understanding and management of water resources. RS involves acquiring information about an object or phenomenon without physical contact .It is the scientific process of gathering data about the Earth's surface and atmosphere, using specialized sensors positioned on various platforms at a distance from the target area. In the realm of hydrology, RS plays a vital role in collecting data on various parameters, including precipitation, soil moisture, snow cover, and water quality (Saha et al**. 2024**). On the other hand, ML is a powerful tool within the realm of artificial intelligent. It enables computers to learn from data and make decisions without explicit programming (Islam et al.**2023**). Together, RS and machine learning revolutionize hydrology by providing advanced techniques for data collection, analysis, and prediction to improve water resource understanding and management. Both RS &ML are progressively being utilized in hydrology to improve flood forecasting and watershed modeling. RS data, including satellite imagery and LiDAR, offers valuable information into land cover, topography, and hydrological variables at large scales. Machine learning algorithms can process and analyze this data, enabling more accurate predictions of hydrological phenomena such as rainfall patterns, river flow, and runoff prediction. Integrating machine learning with remote sensing in hydrology improves our understanding of the Earth's water resources.

Yielding more comprehensive and accurate pictures of hydrological processes. This integration significantly impacts water-related applications. Researchers and scientists have recognized the potential of integrating remote sensing data with machine learning algorithms to improve hydrological modeling, prediction, and monitoring. By leveraging machine learning algorithms, such as neural networks, decision trees, and support vector machines, remote sensing data can be processed more efficiently, allowing for better understanding and forecasting of hydrological processes like rainfall-runoff modeling, flood prediction, and water resource management**.**

In a study by Chen et al. (2018), titled "**Flood Inundation Mapping Integrating Synthetic Aperture Radar and Light Detection and Ranging Data and Machine Learning Algorithm**", they combined remote sensing data from SAR) and LiDAR sensors with DL algorithms. This methodology accurately identified flood extent and water surface elevation, offering a valuable understanding of flood management. Similarly, Wang et al. (2022) titled" **Improved Runoff Prediction for Urban Areas Using Machine Learning and High-Resolution Remote Sensing Data**", researchers focused on improving runoff prediction in urban areas. They utilized machine-learning algorithms, along with high-resolution remote sensing data, to capture urban hydrological processes. By integrating various urban land cover characteristics like impervious surfaces, vegetation, and buildings, they developed precise runoff prediction models. Their findings highlighted the importance of enhancement in prediction accuracy, particularly in densely built urban regions. This study displays the potential of combining ML and high-resolution RS data to refine urban runoff prediction by offering insights for better urban water management. Over the years, hydrological studies have demonstrated a great deal of success with the integration of remote sensing and machine learning. For instance, in flood mapping, machine-learning algorithms may identify regions at risk of flooding by analyzing satellite photos and classifying them according to features of the land cover and water signs. This data facilitates the evaluation of flood risk and the creation of practical mitigation plans. Nevertheless, integrating these approaches presents difficulties, particularly with regard to the quantity and caliber of remote sensing data. The precision and usefulness of the models created may be impacted by the low temporal and geographical resolution of satellite imagery or the high cost and accessibility problems related to LiDAR data. Another challenge is balancing the complexity and interpretability of machine learning models. Deep learning algorithms, while powerful in predictive capabilities, often lack interpretability, (Islam et al. 2023). Delaying understanding of underlying hydrological

processes. Therefore, finding the right balance between model complexity and interpretability is crucial. Combining remote sensing with machine learning in urban hydrology has significant implications. Researchers have successfully utilized this integration to enhance predictions of runoff, develop strategies for urban water management, and mitigate floods, y considering urban characteristics like impervious surfaces and vegetation; predictions that are more accurate have been achieved, leading to improved water resource management practices. The future of this integration holds promise for advancing our understanding of water systems enhancing predictions, and fostering sustainable and resilient water management practices.

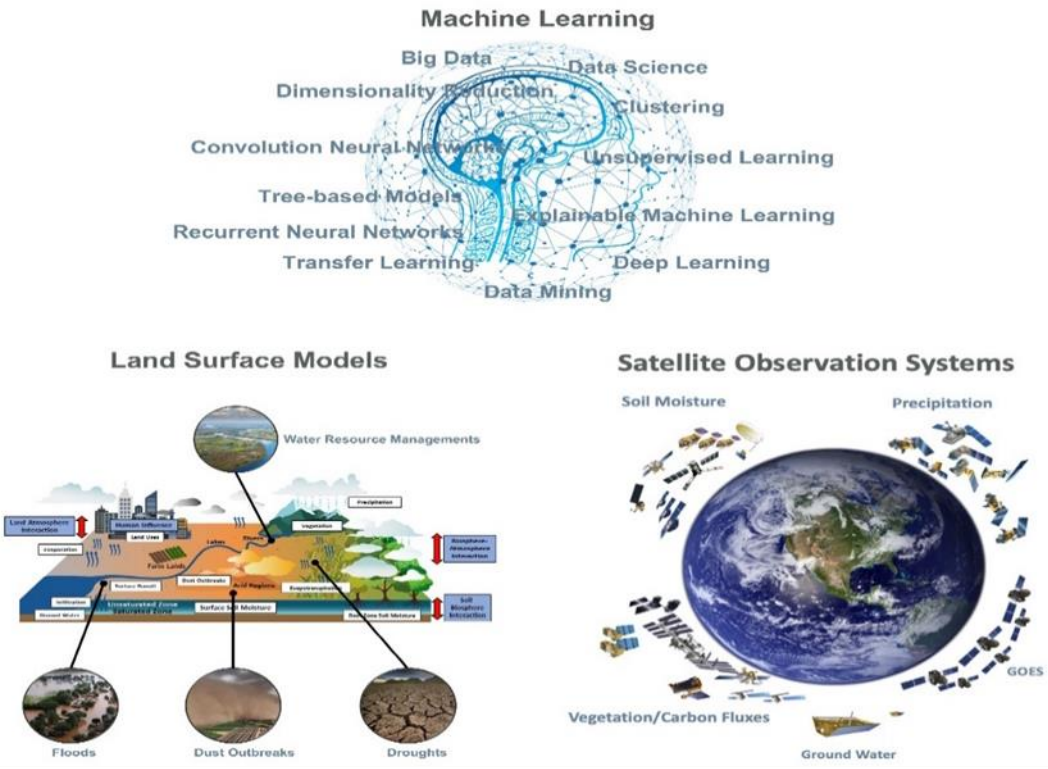

Figure II.5: Hydrology with AI and remote sensing.

(**Image source**: https://www.hydroai.net/contact)

II.6.TRMM in hydrology

The Tropical Rainfall Measuring Mission (TRMM) was a NASA and JAXA collaborative project that ran from 1997 to 2015. Using tools like the Precipitation Radar (PR) and the TRMM Microwave Imager (TMI) to measure rainfall intensity, water vapor, and cloud water, the mission sought to measure rainfall and other precipitation within the tropics. This data was crucial in shedding light on the structure and growth of tropical storms. Because it

allowed for precise rainfall readings in areas with little or no ground-based data, TRMM was crucial to hydrology. This information is crucial for hydrological studies and flood forecasting, as precipitation directly affects river flow and water availability (Abro et al.2020). However, TRMM's mission ended in April 2015. Since then, other satellite and reanalysis data products have emerged to continue providing precipitation data for hydrological studies. These evolving technologies hold the potential to improve the accuracy and reliability of flood forecasting and water management by offering valuable precipitation data in areas without rain gauge data. Various studies have estimated the suitability of satellite/reanalysis precipitation data products compared to observed rain gauge data. These studies have used various statistical and categorical matrices, such as Bias, Nash Sutcliffe, MAE, RMSE, R^2, R, percentage difference, peak error percentage, and peak time error, to assess the accuracy and performance of the satellite/reanalysis precipitation data (Abro et al. 2020).

The application of TRMM in hydrology has significantly improved the understanding of precipitation patterns and their impact on various hydrological processes. With its capacity to provide accurate and high-resolution rainfall data, TRMM has become a valuable tool in hydrological research and applications. One of the primary applications of TRMM in hydrology is in flood forecasting. By capturing precipitation data over large areas, TRMM enables researchers and water management authorities to observe and predict rainfall events that could lead to floods (Suroso et al.2023) This timely information is essential for effective response and mitigation efforts, helping reduce potential flood damage. Moreover, TRMM data has been instrumental in hydrological modeling, which involves simulating water flow and distribution in specific regions. By integrating TRMM rainfall data into hydrological models, researchers can improve the accuracy of stream flow predictions and water availability assessments. This is particularly significant for water resource management, as it helps decision-makers optimize the allocation of water resources and plan for potential water shortages or surpluses. Furthermore, TRMM data has been utilized in studying water balance in different regions, including estimating evapotranspiration rates and understanding the overall water cycle. These understandings are crucial for assessing the availability and distribution of water resources, both in natural ecosystems and human communities.

TRMM data is essential for hydrological modeling because it offers accurate and high-resolution observations of rainfall. For instance, Tang et al (2009), corrected TRMM data for areas, lacking rainfall stations in the upper Bengawan Solo River basin, which increases modeling precision. Similarly, Willy et al. (2020) used TRMM data to analyze water availability

and flood discharge in the Duriangkang Dam, demonstrating its value in hydrological application. Despite These limitations, TRMM data offer valuable insights into precipitation patterns and distribution, vital inputs for hydrological models (Chen et al. **2018**).

II.7.Hydrological models

Hydrology is concerned with the earth's water, its occurrence, circulation, and distribution, as well as its chemical and physical properties and interaction with the environment, particularly its relationship with living organisms. (Ray **1975**, Chow et al. **1988**). Additionally hydrology cycle (Devia et al.**2015**) Hydrological models, as described by (Sorooshian et al.**2008**) are computer-based tools or simplified representations of real-world systems, such as surface water, soil water, groundwater, and estuaries. These models aid in understanding, predicting, and managing water resources. The effectiveness of a hydrologic model is determined by its ability to provide results that closely be similar to reality while using minimal parameters and complexity. Runoff models, which are a type of hydrological model, help estimate the runoff of water as a function of various parameters that describe watershed characteristics. Rainfall data and drainage area are two important inputs required for these models. It's important to note that hydrological processes at the catchment scale are no longer stationary when highly variable nature changes occur within the catchment (Cornelissen et al.**2013**; Mauser et al. **2009**). There are various models available to address hydrological problems, Rainfall-Runoff prediction stands out as one of the most complicated processes in environmental modeling due to the spatial and temporal variability of topographical characteristics of rainfall patterns (Nandakumar and Mein, **1997**). Hydrologic models have evolved into crucial tools for studying hydrological processes and assessing the influence of contemporary anthropogenic factors on the hydrologic system. These models can be categorized based on the presence of random variables and their spatial distribution (Chow, et al. **1988**), as the board classification of hydrological models is shown in **Figure II.8.**

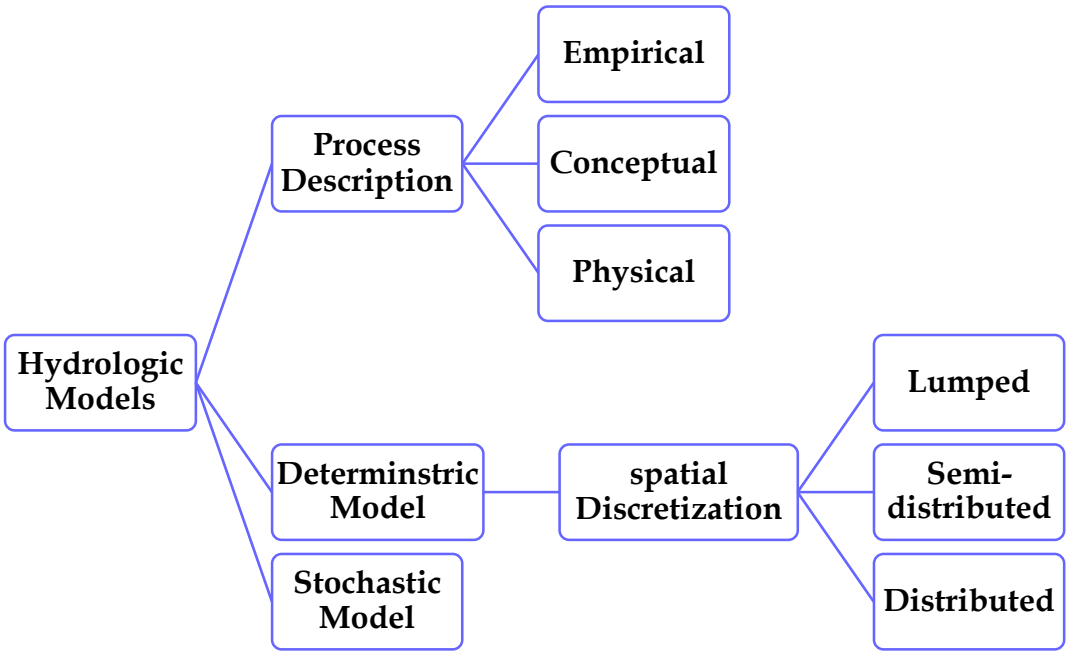

Figure II.6: Classification of hydrologic models.

(**Image Source:** G.S. Dwarakish et al.2015).

Deterministic models, which do not consider randomness, consistently produce the same output for a given input. These models are used for prediction. Lumped models are generally applied to a dimensionless region for simulating various hydrological processes (Niel et al. 2003). Semi-distributed models divide the entire catchment into Hydrological Response Units (HRUs) (Daofeng et al. 2004), while distributed models consider hydrological processes occurring at each grid and define model variables as functions of spatial dimensions (Beven et al. 1980).

Stochastic models produce output that is at least partially random. Hydrological models can be classified into conceptual, empirical, and physically based categories (see Figure II.6). Empirical models, such as Artificial Neural Networks (ANNs) and Genetic Algorithms (GA), establish relationships between rainfall and runoff to predict runoff in various catchments. These empirical models, often referred to as black-box models, lack a physical transformation function to relate inputs to outputs. Daily runoff prediction using ANN models has become important for effective resource planning and management.

A major limitation of empirical models stems from their data-driven nature and their lack of connections with physical catchment processes, leading to errors in representing spatially and temporally distributed precipitation (Roy et al. 2021). On the other hand, conceptual hydrological models, also known as grey-box models, such as the HBV and

HYMOD models, offer functional algorithms to describe hydrologic processes but may require calibration for accurate representation (Parra et al. 2018). The study highlights that the HBV model better represents quick precipitation-runoff processes, while the HYMOD model excels in slow, time-aggregated processes, underlining the importance of selecting models based on the specific hydrological processes under study.

Physically based models, also known as white-box models, are advanced tools based on differential equations, often regarded as deterministic models (Liu et al. 2017). However, like all models, they have limitations in accurately capturing daily runoff due to various factors, requiring a deep understanding of hydrological parameters. Representing the complexities of hydrological processes at small scales can be challenging. Another limitation is the gap in short-term prediction capability. These models often struggle to predict daily runoff accurately, failing to account for local hydrological conditions, land use changes, and precipitation patterns (Aynom et de al. 2018). Additionally, inaccuracies in runoff prediction methods can lead to uncertainties in results.

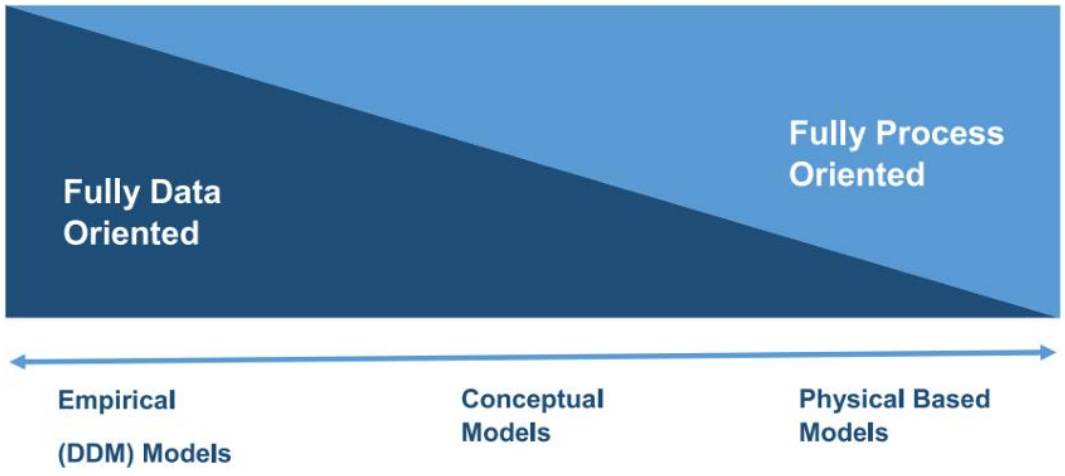

Figure II.7: Data use degree for each model type (**Image source:** Moulahoum ,2019).

Researchers like "**Comparison of Conceptual and Distributed Hydrological Models for Runoff Estimation in a River Basin**" show daily runoff estimation accuracy is considered against model complexity and data needs (Sreedevi et al. 2021). Lastly, **"Daily runoff prediction based on the adaptive Fourier decomposition method and multiscale temporal convolutional network**" by Yu L et al. (2023), presents novel strategies to get around the non-linearity and non-stationary of runoff series, which are significant hurdles for traditional forecasting models.

These studies collectively highlight the current need to improve hydrological models to increase their accuracy and reliability in daily runoff prediction. Overall, there is a recognition of gaps in traditional models, particularly in their ability to account for the complexities of hydrological processes at small scales and to accurately predict floods and extreme events. This necessitates the exploration and adoption of innovative approaches that can bridge these gaps and improve the effectiveness of hydrological modeling. Recent studies have explored the efficacy of data-driven approaches, such as ANN, SVR, and LSTM models, in improving runoff. Here are some examples of innovative approaches in accurate runoff prediction.

Table II.4: Examples of some innovation approaches

Innovation approaches	Method	Process	Results
Ensemble deep learning models (EDLM)	Combining variational mode decomposition (**VMD**), convolutional neural networks (**CNN**s), bi-directional long short-term memory networks (**BiLSTMs**), and Bayesian optimization	VMD decomposes daily runoff data into internal model functions (**IMFs**) with different frequencies. CNNs extract features from each IMF component. BiLSTMs with an attention mechanism (AM) predict runoff. Bayesian optimization optimizes BiLSTMs hyper parameters.	Applied to Wei River Basin data, achieved RMSE of 3.54 and 15.23 for test sets at two stations, outperforming other models **(**Wu, **2023)**.
Time varying models (TVM)	Time varying dynamic model averaging.	Incorporate TV weights for model averaging.	Achieve high prediction accuracy with a 0.97 NSE and reduce uncertainty (Ran, **2022)**
Hybrid frameworks	Deep neural network combined with CNN, LSTM and ConvLSTM networks	Addresses nonlinear relationships between runoff and meteorological topographic and geomorphic elements.	Provides an improved accuracy by leveraging deep learning techniques **(**yang, X, **2024**)

II.8.Advancements and innovations in runoff prediction

Runoff simulation serves as an important technique in modeling the water cycle (H et al. **2015**), Accurate and reliable runoff prediction aids flood control managers in effectively managing floods, which holds important for watershed and urban flood control ,which disaster reduction and urban planning (Hadid et al. **2019**). However, due to the nonlinearity and complexity of runoff series (Man et al. **2022**), accurate and reliable prediction of runoff is a very challenging task. Therefore, advanced models were needed to provide higher accuracy and more stable runoff prediction (Yang et al. **2022**). While previous research has made significant progress in rainfall-runoff modeling, there remains a serious need for innovative approaches to address the limitations of current models. Notably, the absence of a physical mechanism poses a substantial obstacle in applying machine-learning methods, which typically rely on labeled observations (Xie et al. **2021**). The consideration of initial loss (IA) within a DL network for rainfall-runoff simulation has received limited attention. IA represents a crucial stage in the rainfall-runoff process, the numerical model of the physical mechanism started early and has been widely used in runoff prediction (Petroselli et al**. 2022**). However, the hydrological process of the basin is very complex. Therefore, accurate hydrological process simulation requires a large number of accurate hydrological process data and fine underlying surface data (Mignot et al, **2019**). With the development of artificial intelligence and deep learning technology, runoff series prediction by the data-driven method has become popular (Hou et al. **2021**) the data-driven model does not need to consider the physical mechanism. Through the analysis of time series, it can capture the nonlinear relationship between driving factors and runoff, which can avoid the influence of subjective factors on the uncertainty of the model (Guo et al. **2022**).

DL models, especially LSTM, are receiving a lot of interest in hydrological modeling due to an increase in hydrological observations and advanced computing capabilities (Ahmed et al. **2022**). LSTM stands out as an alternative to traditional RNN for treating and predicting significant events with extremely long intervals and delays in time series. It effectively the issues of long-term information retention and short-term input loss. Currently, LSTM has proven to be the most accurate model for runoff.

Kratzert et al. (**2018**) found that the Sacramento Soil Moisture Accounting Model (SAC-SMA) combined with the Snow-17 snow routine produced inferior results to the usage of LSTM to model runoff in 241 catchments of the CAMELS (Catchment Attributes and

Meteorology for Large-sample Studies) dataset. Across 531 catchments in the CAMELS dataset, Kratzert et al. (**2019**) EA–LSTM model beat two regionally calibrated hydrological models, VIC and mHM. Furthermore, in order to simulate runoff in the Xingjian and Qujiang River basins, the accuracy of runoff forecasts based on meteorological and hydrometric stations can be limited due to their low numbers and dispersed distribution in many watersheds. To address these challenges, researchers have found that satellite data's spatial coverage and the use of remote sensing methods provide more precise and comprehensive information about soil moisture, increasing the performance of runoff prediction models **(**Nimai, **2023)**These developments use DL and artificial intelligence to get around the drawbacks of conventional physical models. Data-driven models are becoming more and more popular because they can identify nonlinear correlations in the data without depending on particular physical mechanisms. Examples of these models are Gated Recurrent Unit (GRU), LSTM, and BP. In a study by Xianqi Zhang et al. (**2023**), a hybrid predicting model was developed to improve runoff predicting. It integrates the kernel extreme learning machine (KELM) algorithm, optimized using the butterfly optimization algorithm (BOA), with the variational modal decomposition method (VMD) and the complementary ensemble empirical modal decomposition method (CEEMD). The model achieved average absolute errors ranging from 23.72 to 30.02, and RMSE spanning from 18.66 to 21.87 m^3/s. furthermore, decision coefficients consistently exceed 90%, while NSE coefficients surpass 90% highlighting the superior predictive performance of the proposed method in predicting runoff time series (Zhang et al.**2023**).

II.9.Gaps in the Literature

Runoff is one of the most important hydrologic elements necessary for water resource management (Adam et al. **2017**), and in recent years, there has been growing interest in combining satellite-based precipitation data from the Tropical Rainfall Measuring Mission with machine learning techniques for runoff prediction. However, there are still significant gaps and challenges that need to be addressed in this field. One of the key gaps in the existing literature is the limited availability of long-term and high-quality runoff data for model training and validation. Another challenge is the heterogeneity of TRMM data, which includes various sources such as microwave radiometers and radar sensors. The accuracy of runoff predictions by hydrological models is frequently limited, particularly in areas with limited data or during extreme events. ML provides a possible remedy by using explicit statistical

models to handle complex nonlinear interactions. Furthermore, machine learning's power lies in its versatility, since it can be used to a wide range of issues, including classification, regression, and prediction. As well as its effectiveness in learning and generalizing a huge number of data (He et al. **2016**). Due to these features, various ML algorithms are widely adopted in runoff prediction, SVR (Kumar et al. **2019**), CNN, (Le et al. **2020**), DNN, (Tao et al**.** **2016**), ANN (Wehbe et al. **2020;** Hong et al. **2021**), LSTM network (Tang et al. **2021**). However, most of these studies mostly considered limited environmental information and spatial correlation related to precipitation while neglecting the spatial autocorrelation between gauge observations in merging processes. TRMM is a satellite mission that provides high-resolution rainfall data, which can be used as input for runoff prediction models. In recent years, there has been a growing interest in combining TRMM data with machine learning algorithms for runoff prediction. One study by AghaKouchak et al. (**2009**) highlighted the uncertainties in TRMM satellite estimates, which can limit their usefulness in hydrologic predictions such as rainfall-runoff modeling. The study suggested that accounting for these uncertainties is important for improving the accuracy of hydrologic predictions. Another challenge is the interaction of spatial and temporal rainfall variability with hydrological response in urban basins, as discussed in Elena Cristiano et al**.** (**2017**)**,** the study suggests that the characterization and influence of spatial and temporal rainfall variability on runoff response is not well understood, particularly in urban catchments. The study also highlights the importance of basin characteristics in impacting the sensitivity of hydrological response to rainfall, and the need for more research in this area. In summary, though there is potential for improved runoff predictions by integrating machine learning with satellite data such as TRMM, there are still obstacles to overcome, including understanding the impact of spatial-temporal variability on hydrological response and accounting for uncertainty.

II.10.Theoretical framework

Accurate runoff prediction demands the integration of TRMM data with machine learning algorithms. TRMM data, standing for Tropical Rainfall Measuring Mission data, provides valuable information about precipitation patterns and rainfall rates. By combining TRMM data with advanced machine learning algorithms like the MLP neural network we can create a robust predictive model.MLP is a type of artificial neural network that consists of an input layer, one or more hidden layers, and an output layer. This neural network architecture allows for nonlinear mapping between input and output variables, making it suitable for complex data analysis tasks like weather prediction, and runoff prediction. Another relevant

theoretical framework is the XGBoost Algorithm, an implementation of gradient boosting that has proven highly effective in various ML tasks such as regression and classification. XGBoost works by sequentially adding weak prediction models to create a strong model that can accurately predict runoff outcomes based on the TRMM data. In addition to MLP and XGBoost, another relevant theoretical Framework for integrating TRMM data with machine learning for runoff prediction is the Long Short-Term Memory network.LSTM is a type of (RNN) well-suited for analyzing sequential data. Widely adopted in times series analysis and prediction tasks, LSTMs use gates-namely (input, output, and forget gates) to control information flow within the network. By integrating TRMM data into the machine learning algorithms, we can increase the performance of these models and further improve the accuracy of Runoff predictions. Several studies have explored the application of different machine-learning models in conjunction with TRMM data. Performance evaluation of runoff prediction models using TRMM and machine learning typically involves statistical metrics such as the R^2, RMSE, R, and MAE (Shah et al. **2023**), these metrics help assess the accuracy and reliability of the models, providing understanding of their suitability for water resource management applications. According to a study that compared the performance of LSTM, XGBoost, MLP, MLR, and SVR models in runoff prediction, LSTM exhibited improved performance compared to the other models. However, its performance was inferior to the best-performing model (Sibtain et al. **2022**). A study by YuanYuan Man et al, (**2023**) used the LSTM model for daily runoff prediction in the Upper Huai River Basin, China. The method involves incorporating a novel loss function, PES, into the LSTM model to improve accuracy. The study evaluates the performance of the enhanced LSTM model for daily runoff prediction. Results demonstrate that the enhanced LSTM model with PES as a loss function outperforms the traditional LSTM model in predicting daily runoff in the Upper Huai River Basin. Additionally, the study compares the enhanced LSTM model's performance with other machine learning models such as RFR and XGBoost. However, the results still show that the enhanced LSTM model performs better than these models in predicting daily runoff in the Upper Huai River Basin.

II.11.Conclusion

In this second chapter, we provided a detailed examination of how we predict runoff, such as when rainwater flows over the ground. We discuss both traditional and modern approaches, including the use of satellites and computers to aid in this process. The chapter shows the evolution of these methods over time and identifies determined challenges. Additionally, it highlights areas requiring further innovation to improve predictive accuracy.

This chapter lays the groundwork for future research aimed at improving the utilization of satellite data and computer technology for more precise runoff prediction.

Chapter III: Study Area and Methodology

Chapter III: Study area and methodology

III.1.Introduction

The watershed of Wadi Ouahrane has been chosen as the study basin for its rich diversity of available data. In this Chapter a comprehensive examination of the geographical and geomorphological features of the study area, focusing on its hydrographic network and climatic variables. The chapter begins with an exploration of relief characteristics, including area, perimeter, shape, altitudes, and slope indices, offering critical insights into the terrain's morphology. Then, the constitution and morphometric of the hydrographic network are investigated, underlining the region's water distribution and flow patterns. Climatic factors such as temperatures, evapotranspiration, humidity, wind speed, and precipitation are scrutinized to understand their influence on the study area's hydrology. The chapter also details the data acquisition process, including the integration of TRMM data, and the selection of input variables for further analysis. Statistical methods such as PACF and ACF are employed to refine the input selection process, laying the groundwork for subsequent machine learning modeling.

III.2.Geographical Location of Study Area

The study region is the Wadi Ouahrane Basin in northern Algeria, situated between latitudes 36°00′ and 36°24′ N and longitudes 01°00′ and 01°3′ E. Spanning over 270.7 km², it serves as a tributary of the Wadi Cheliff Basin. The Wadi Ouahrane Basin is bounded by the Wadi Fodda Basin to the east, the Wadi Ras Basin to the west, the Wadi Allala Basin to the north, and the Wadi Sly Basin to the south. It has a Mediterranean climate, with an annual average rainfall of 333 mm over the period 1972–2018. The mean annual temperature is 18 °C. (Achite et al.**2023**). The spatial distribution of precipitation shows two contrasting rainfall zones in two different areas:

- The Ouled Fares area receives less than 400 mm of rain and is located below 200 m. It occupies nearly 40% of the basin's area.
- The Benairia area is located above 350 m, where the average annual rainfall ranges from 280 to 740 mm. This area occupies about 60% of the basin area.

The watershed of the Wahrane Wadi is characterized by an impermeable marl substrate covering 80% of the basin's surface.

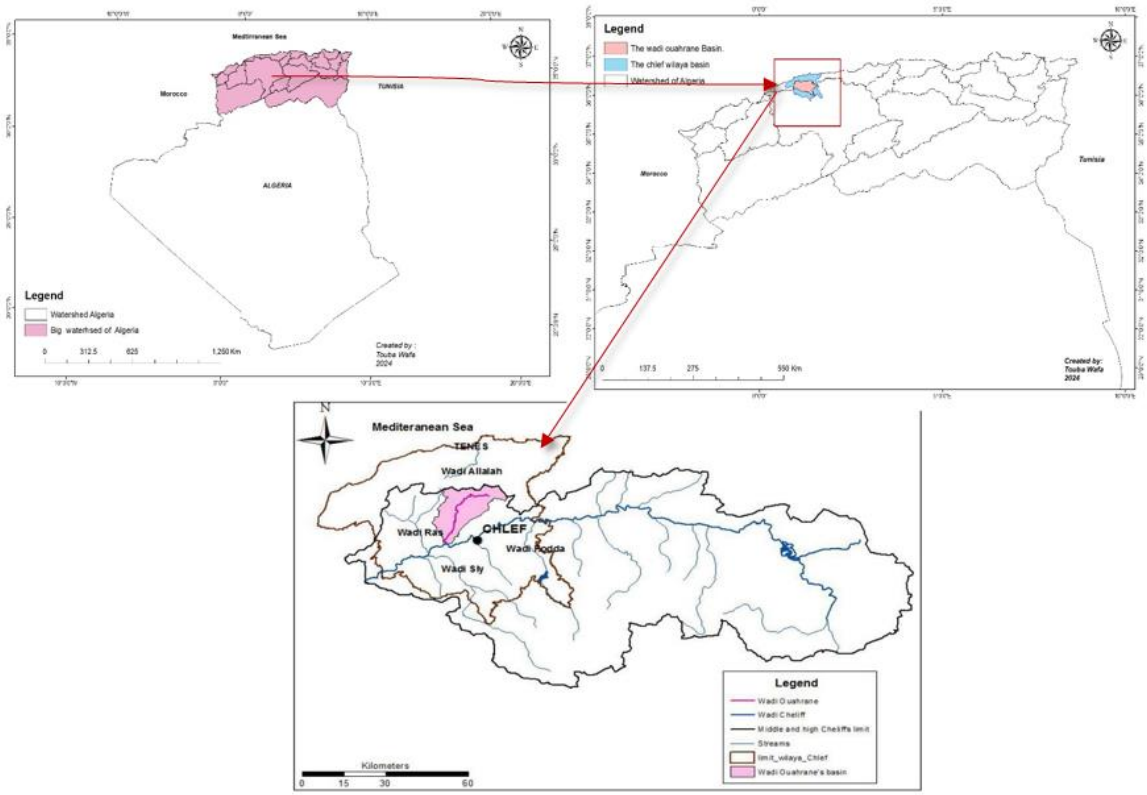

FigureIII.1: Location, of the Wadi Ouahrane basin.

III.3.Geomorphological setting

The various morphometric parameters of a watershed (shape, altitude, slope, relief, etc.) often interact in combination, influencing the flow dynamics. They enable quantitative analysis and comparison of different hydrological units. However, to ensure the reliability of the morphometric assessment, this quantification must be applied to small, geologically homogeneous watersheds.

III.3.1.Relief

The influence of relief on the hydrograph is even more evident. A steeper slope correlates with a shorter concentration time of runoff water in drainage channels and thus in tributaries and the main river. Figure III.2 illustrates the basin relief of Oued Ouahrane, which is indicated by contour lines connecting points of equal elevation.

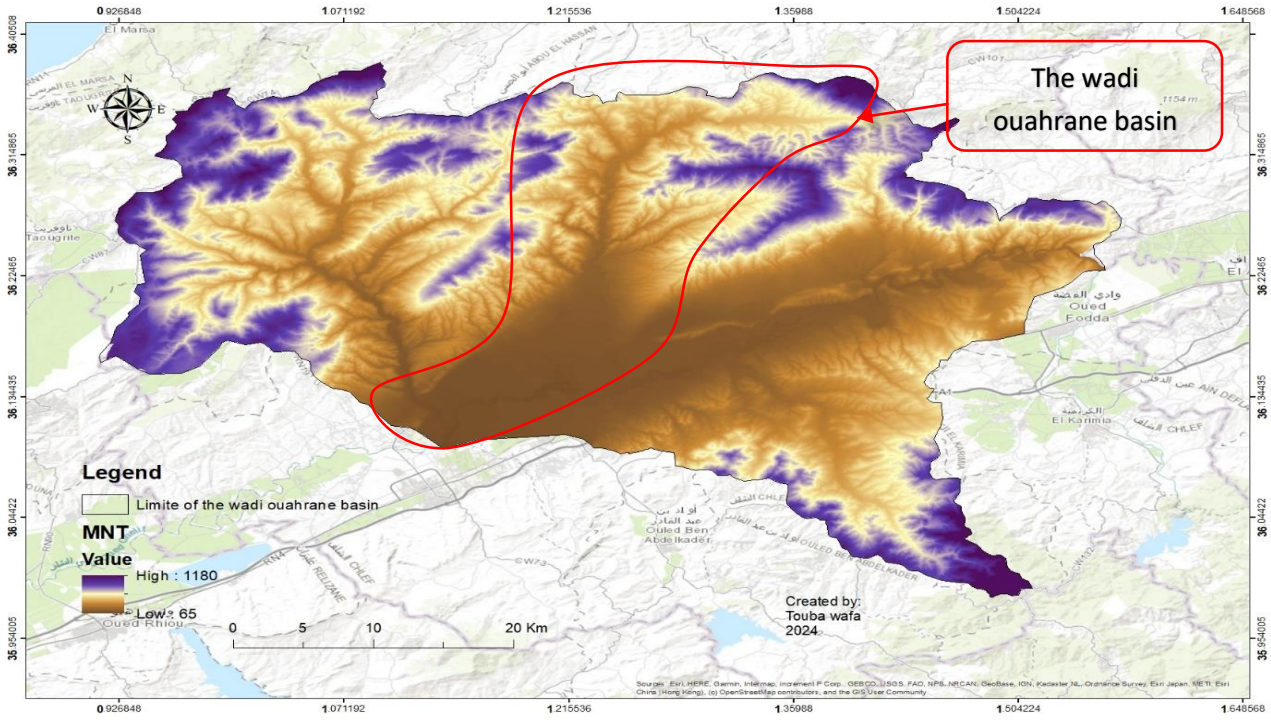

FigureIII.2: Digital Terrain Model of the Wadi Ouahrane Basin.

III.3.1.1.Area and perimeter

The basin of the Wadi Ouahrane covers a plan metric area of 270.7 km², bounded by a watershed line that represents the perimeter of the basin, which is estimated at 88 km (BENKHALED, 2006).

III.3.1.2.Shape of the basin

This element can be translated by the parameter K_G, known as the Gravelius compactness index, which has a definite influence on flow. The shape of the basin determines the shape of the flood hydrograph, where an elongated basin will not react in the same way as a compact basin. For the Oued Ouahrane basin, the Kc index was estimated at 1.66, indicating low compactness (elongated basin), which is confirmed by the dimensions of the equivalent rectangle. The length and width of the equivalent rectangle are 36.65 km and 7.37 km, respectively.

Dimensions of the Gravelius compactness index calculated by formulas:

$$K_G = \frac{P}{2\sqrt{\pi A}} \approx 0.28 \frac{P}{\sqrt{A}} \qquad \textbf{(III.1)}$$

With:

K_G: Gravelius compactness index.

A: Watershed area [km²].

P: Basin perimeter [km].

This index is calculated from a topographic map by measuring the perimeter and area of the watershed. It is close to 1 for a watershed with an almost circular shape, and greater than 1 for an elongated watershed. A circular watershed provides more efficient drainage compared to an elongated watershed.

Dimensions of the rectangle equivalent are calculated by formulas III.2 and III. 3:

$$L_r = \frac{K_G \cdot \sqrt{A}}{1.12}\left[1 + \sqrt{1 - \left(\frac{1.12}{K_G}\right)^2}\right] \quad (\mathbf{III.2})$$

$$l_r = \frac{K_G \cdot \sqrt{A}}{1.12}\left[1 - \sqrt{1 - \left(\frac{1.12}{K_G}\right)^2}\right] \quad (\mathbf{III.3})$$

Lr: Length of the equivalent rectangle [km], **lr:** Width of the equivalent rectangle [km].

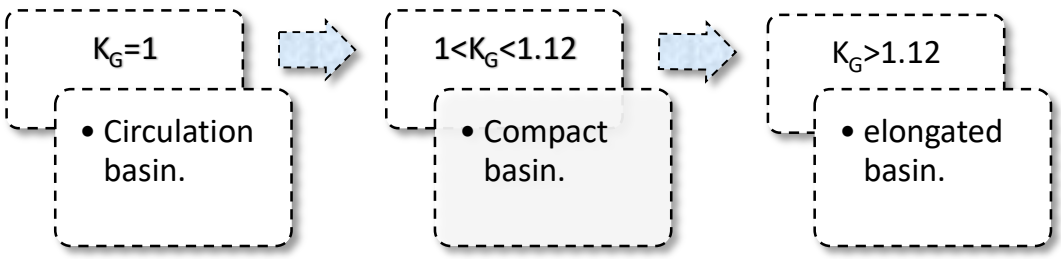

Figure III.3: The basin shapes associated with Gravelius coefficients.

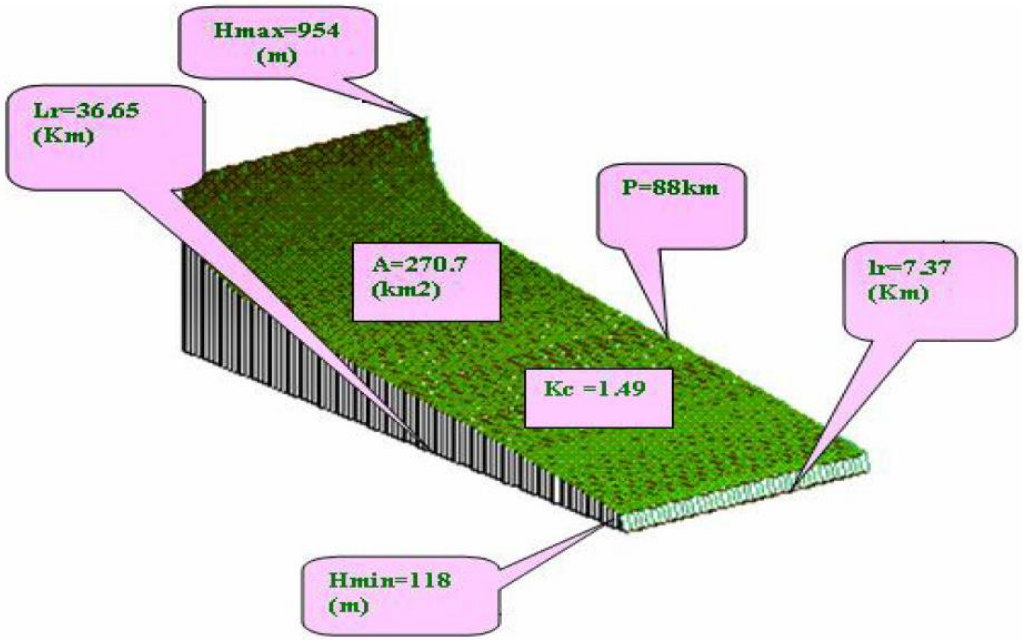

Figure III.4: Equivalent rectangle with three dimensions of wadi Ouahrane

(REMAOUN M. 2007).

III.3.1.3.Altitudes

The average elevation of the Oued Ouahrane basin is approximately 366.50 m.

$$H_{moy}=\frac{\sum Hi.Si}{\sum Si} \qquad (\textbf{III.4})$$

Therefore, areas with altitudes exceeding 600 m are limited in the basin, covering an area of 62.4 km², or approximately 23.05%, and correspond to the mountains located in the northern part of the basin (Dahra-Zaccar). Areas with altitudes ranging from 600 to 150 m cover 176.53 km², or about 65.21% of the total area. In contrast, areas with altitudes between 150 and 65 m cover an area of 31.73 km², or 11.72% of the total area, and largely encompass the valley of the Oued Ouahrane and its main tributaries.

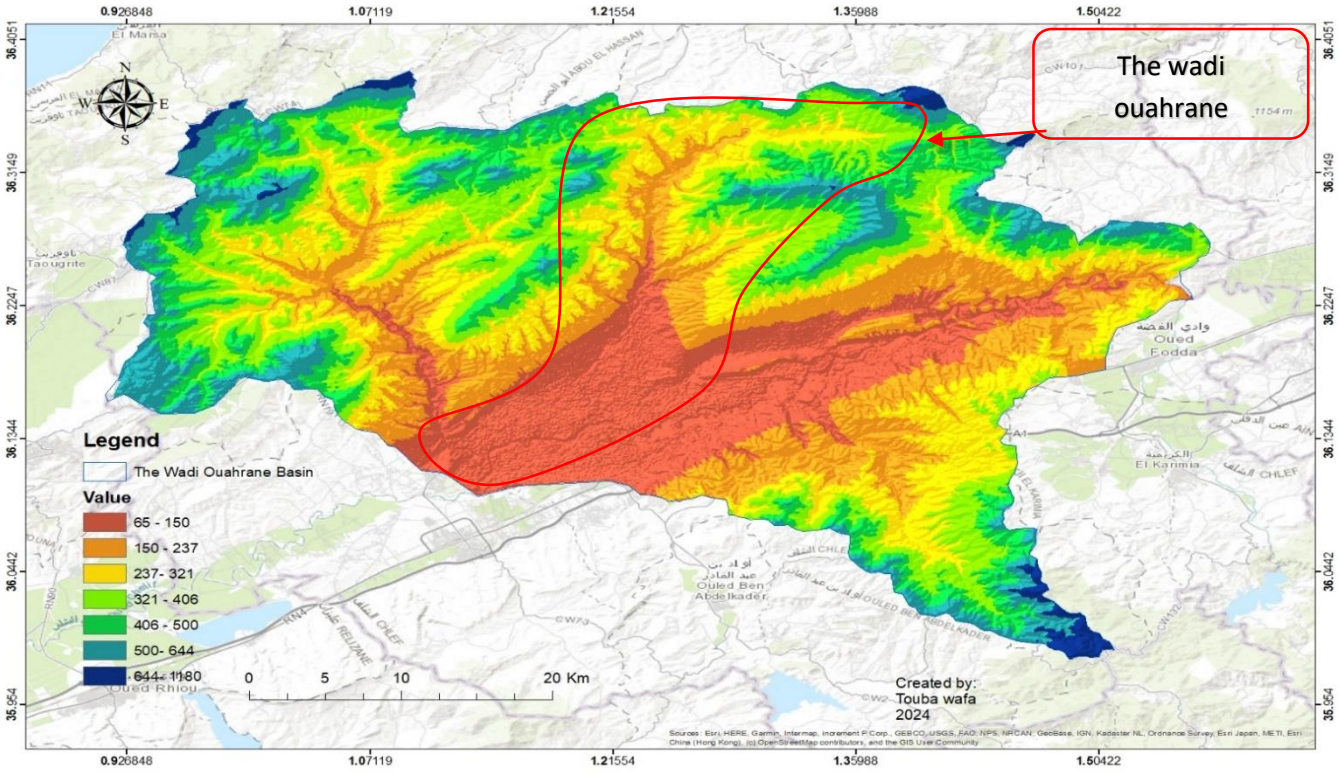

Figure III.5: Elevation map of the wadi Ouahrane basin.

III.3.1.4. Slope and relief indices

The relief plays a key role in the greater or lesser capacity for runoff.

III.3.1.4.1. Rock Slope index (I_P)

The Rock slope index is the average of the square root of slopes measured on the equivalent rectangle, weighted by the surfaces.

$$I_P = L_r^{\frac{1}{2}} \sum_{i=1}^{n} (a_i . d_i)^{\frac{1}{2}} \qquad \textbf{(III. 5)}$$

With:

L_r: length of the equivalent rectangle, **(a_i):** Fraction as a percentage of the area between two neighboring level curves distances from ($\mathbf{d_i}$).

III.3.1.4.2.Global Slope index (I_g)

It is the difference in altitude between the altitude exceeded by 5% of the surface area of the basin and that exceeded by 95% of the surface area, at the length of the equivalent rectangle

$$I_g = \frac{D}{L_r} = \frac{H_{95\%} - H_{5\%}}{L_r} \qquad (\mathbf{III.6})$$

The global slope index "Ig" is estimated at 11.31 m/km, which implies that the relief of the wadi Ouahrane basin is low (10 <Ig <20) according to the classification of the O.R.S.T.O.M (Office of Scientific and Technical Research Overseas).

III.3.1.4.3.The specific altitude difference (D_s)

To allow a comparison of the basins with each other from a relief point of view, we determine the specific height difference which serves as the basis for a classification proposed by O.R.S.T.O.M.

$$D_S = I_g . \sqrt{A} \qquad (\mathbf{III.7})$$

$$Ds = \frac{D}{L_r} . \sqrt{A} \qquad (\mathbf{III.8})$$

$$Ds = D. \sqrt{\frac{I_g}{L_r}} \qquad (\mathbf{III.9})$$

With:

Ig: Global Slope index [m/km].

A: Basin area [Km²].

Lr: Length of the equivalent rectangle [km].

Sub-classes of relief as defined by O.R.S.T.O.M. hydrologists. (IRD-Currently)

Table III.1: The sub-classes of relief as defined by O.R.S.T.O.M.

Ds <10m	Class R1	Very low relief
10 <Ds<25	Class R2	Low relief.
25<Ds<50	ClassR3	Fairly low relief.
50<Ds<100	ClassR4	moderate relief
100<Ds<250	ClassR5	fairly strong relief
250<Ds<500	ClassR6	strong relief
DS>500	ClassR7	Very strong relief.

So classify the relief of the Oued Ouahrane basin, it seems more reliable to rely on the specific relief (Ds) instead of the global slope (Ig), as the latter can only be significant in the case of basins larger than 25 km² in area. The value of Ds estimated at 428.71m reflects the importance of the mountainous volume, as well as the significant elevation differences, qualifying the relief of the Oued Ouahrane basin as strong relief (250m < Ds < 500m) according to the same classification by O.R.S.T.O.M.

III.3.1.4.4.Slope classes

The topographic slope expresses the inclination of the slopes in relation to the horizontal. It is an essential factor in surface runoff, as it tends to have more kinetic energy in the presence of steep slopes and elevation differences. Consequently, it ensures a rapid hydrological response and aggressive erosive dynamics. According to J. TRICART, the intensity of flow as a function of slope is described as follows:

- **Weak flow:** slope less than 10%.
- **Strong flow:** slope equal to 10%.
- **Very strong flow:** slope greater than 20%.

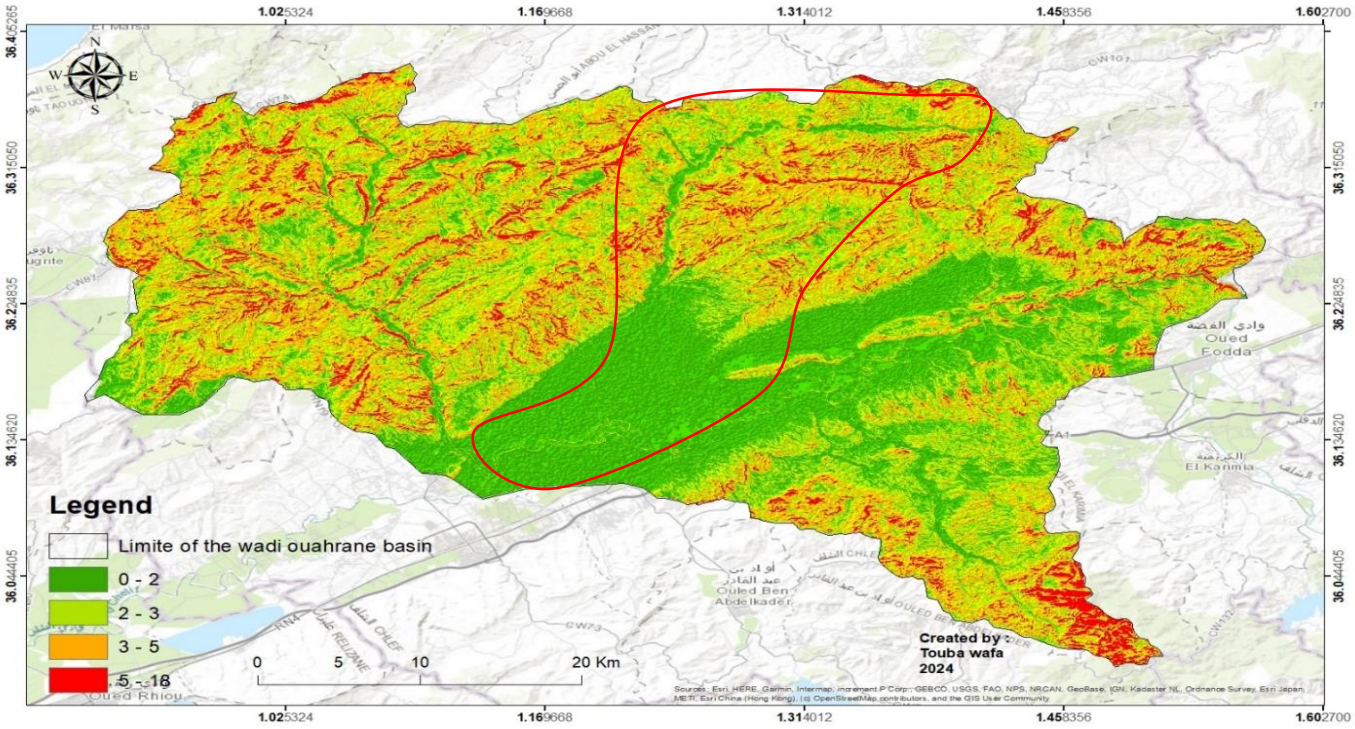

Figure III.6: Slope Map of the wadi ouahrane basin**.**

Slope (0-2%) and (2-3%), (3-5%): Areas with slopes less than 10%. This encompasses the regions colored in Green, light green, and orange. These areas are characterized by gentle slopes and are likely to have slower water flow, reducing the potential for rapid water movement.

Slope (5-18%): Areas with slopes around 10%. These regions are part of the Red areas, where the slope is on the higher end of the 5-18% range. Water flow in these areas is expected to be more vigorous, contributing to faster water movement

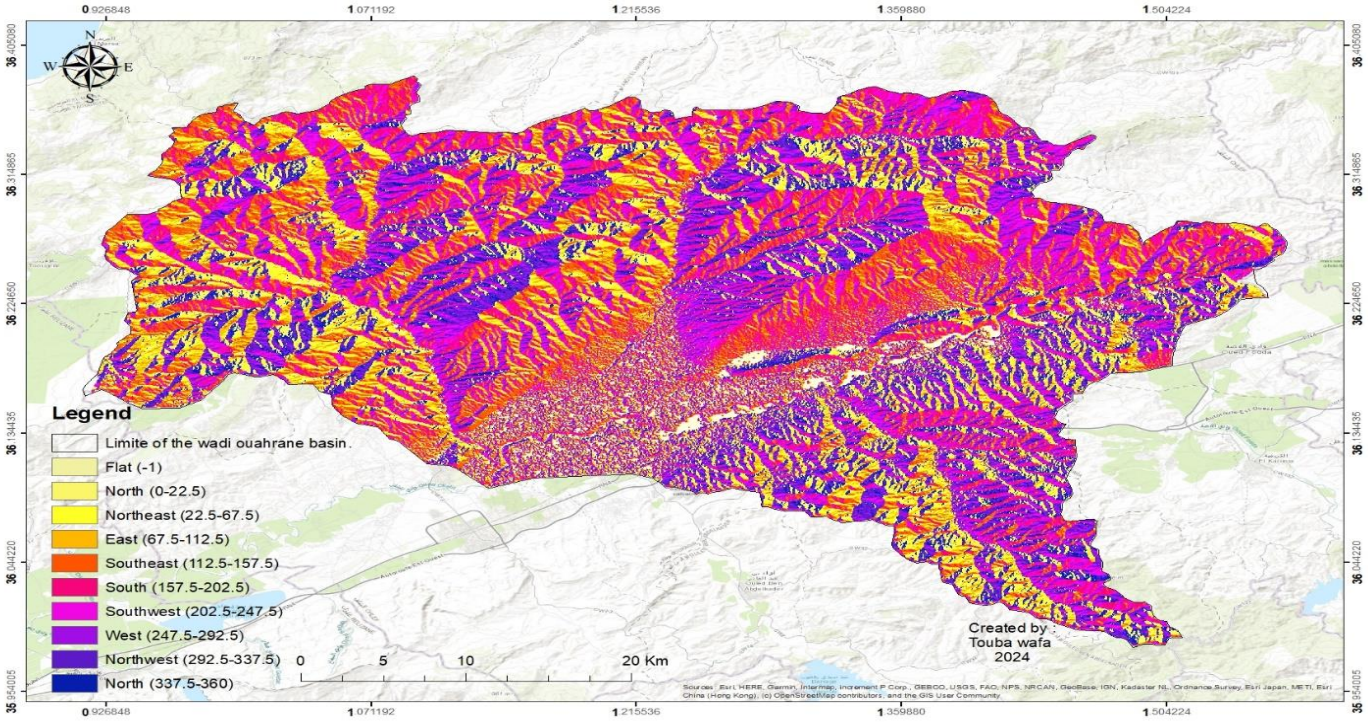

FigureIII.7: The Aspect map of the wadi ouahrane basin.

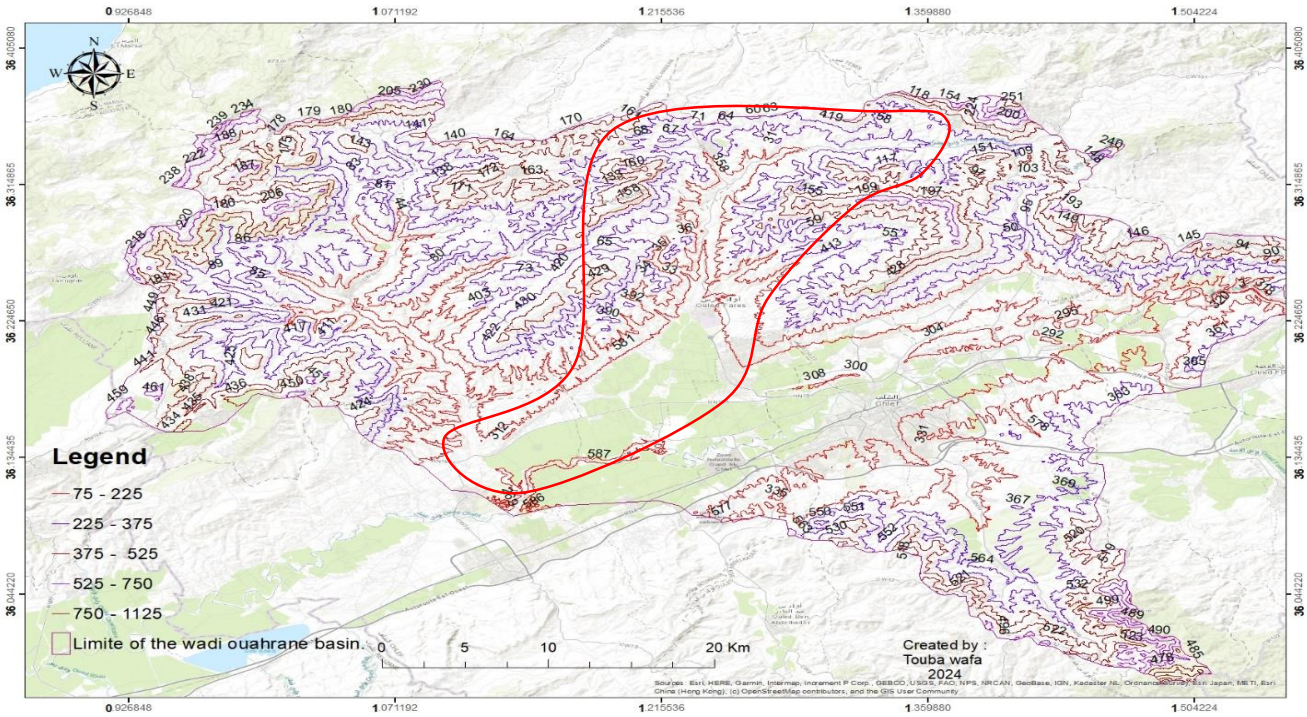

FigureIII.8: The Contour map of the wadi ouahrane basin.

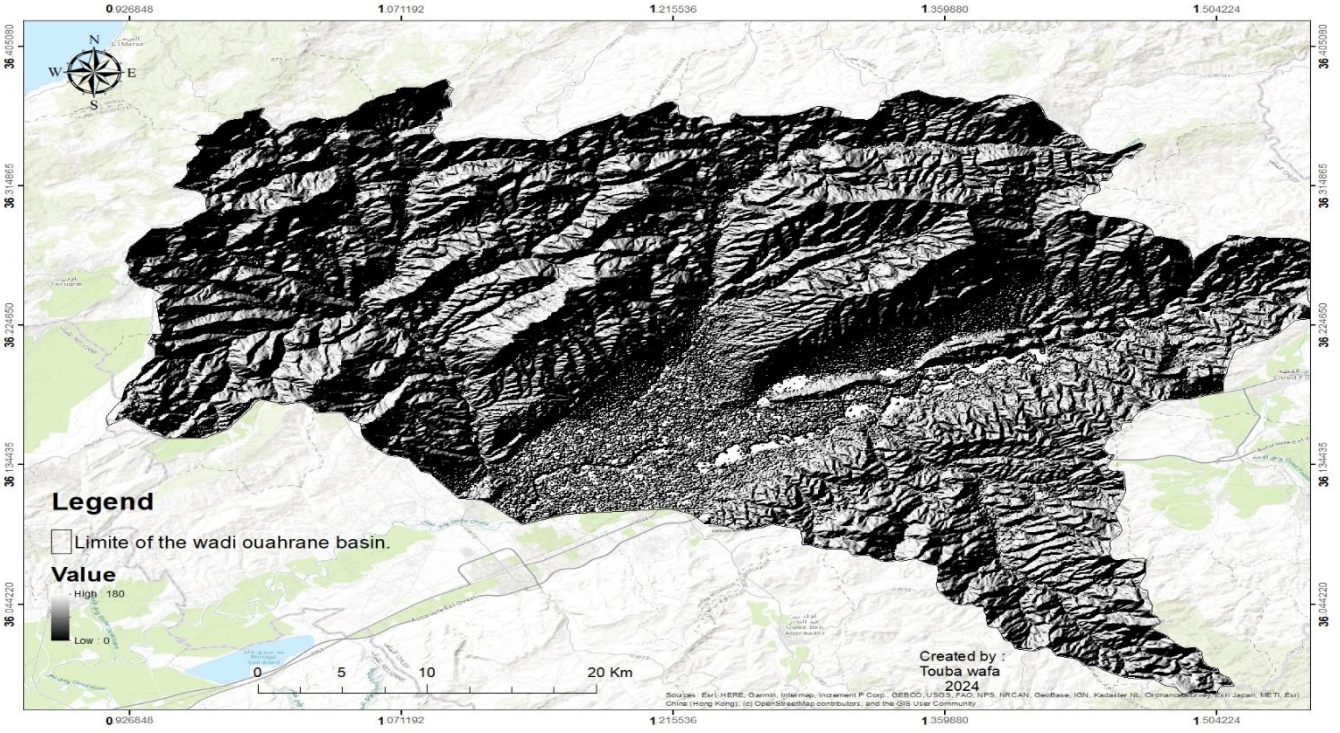

FigureIII.9: The Hill shade map of the wadi ouahrane basin.

III.3.2.Constitution of the hydrographic network

The drainage of the basin is provided by the Ouahrane Wadi, which belongs to the larger Chellif-Zahrez system. It receives on its left bank a relatively significant small tributary, as shown in which drains the area of conglomerates and sands (**BENKHALED 2006).**

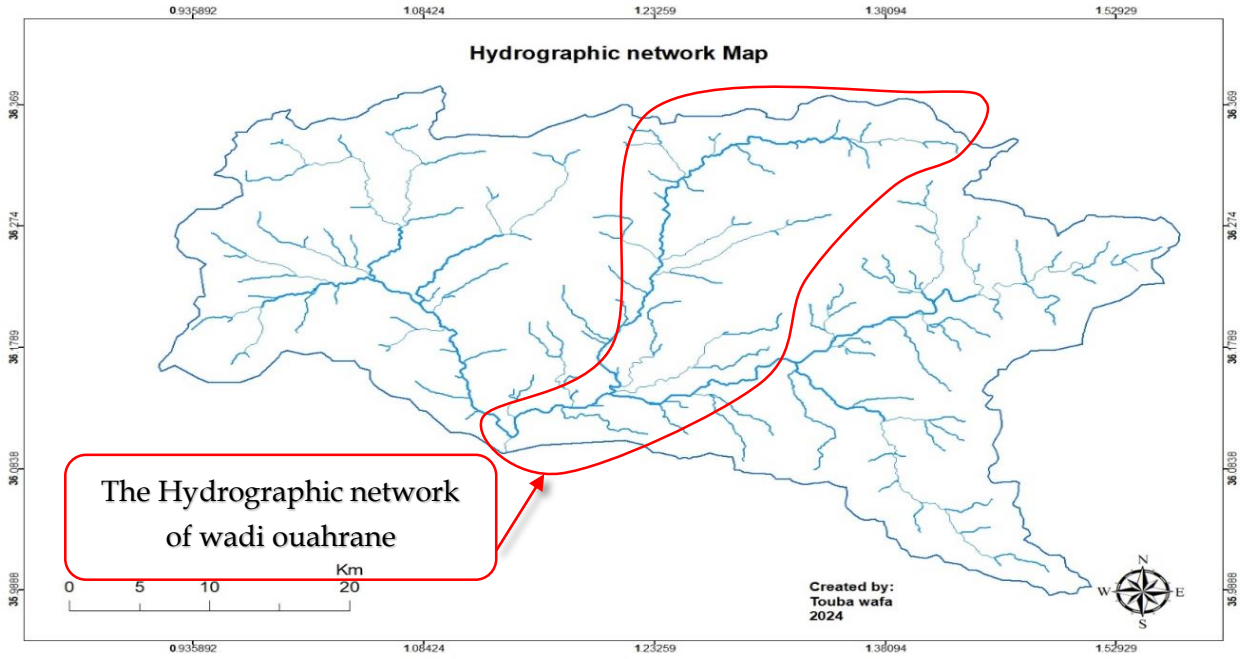

FigureIII.10: Hydrographic map of the wadi ouahrane basin.

III.3.3.Hydrographic network morphometric

The interaction of climate, lithology, and topography in the watershed has led to the formation of a particularly dense hydrographic network. This is reflected in an estimated drainage density (Dd) of 0.13 km/km². This high drainage density is unsurprising, given that the basin's concentration time, calculated according to the Giandotti law, does not exceed 10 hours. These values indicate that the rainfall will be converted into runoff, reaching the outlet (Chlef plain and city) in approximately 9.12 hours. Given the basin's extensive area of 270.7 km², this rapid water mobilization is noteworthy and is attributed to the physical characteristics of the basin previously discussed, which favor a significant hydrological response through substantial runoff.

III.4.Climatic factors

The climate of Chelif is characterized by hot, dry summers and mild, wet winters, and it can be described as semi-arid Mediterranean. We present a few climate factors defined based on statistical analysis of field data. Precipitation will be examined in more detail separately due to its importance as a key parameter in the study of water flow and especially flooding.

III.4.1.Temperatures

According to Peguy (**1970**), temperature is defined as a quality of the atmosphere rather than as a measurable physical quantity. Table III.1 below summarizes temperature observations from two stations in the basin. It highlights two distinct seasons: a cool season from October to April during the rainy season and a warm season from May to September during the dry season. These seasonal variations significantly affect the water balance, particularly potential evapotranspiration values (Benkhaled **2006;** Remaoun **2007**). At both stations, temperatures change monthly, reaching a low of 9.5°C in January and a high of around 30°C in July and August.

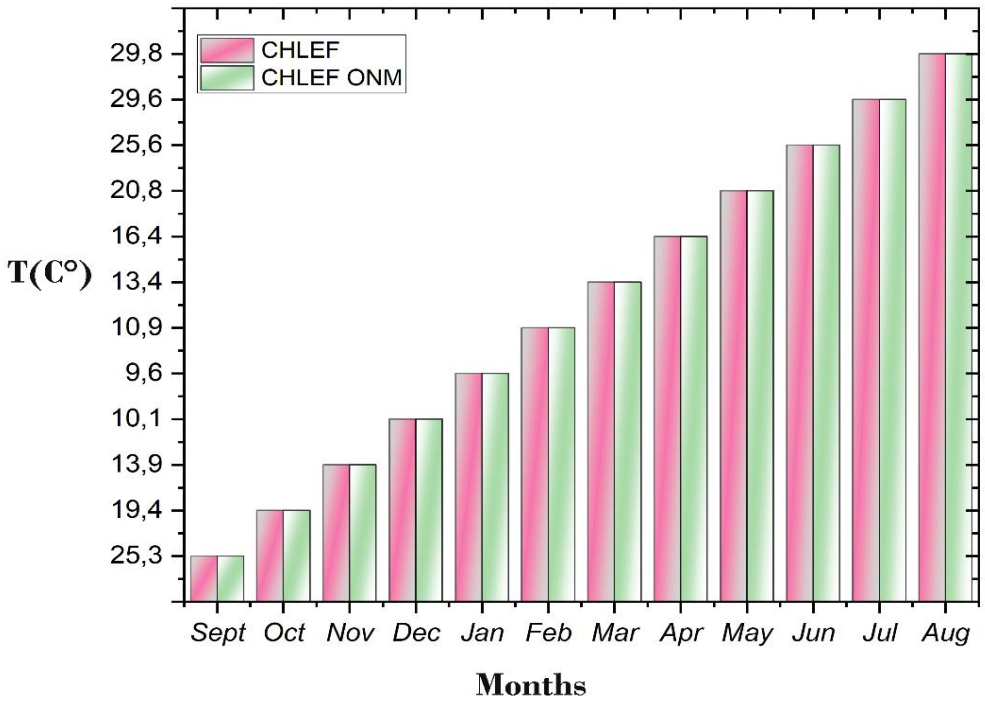

Figure III.11: Inter-annual mean temperatures in the wadi Ouahrane basin.

III.4.2. Evapotranspiration

The arid climate and the spatio-temporal irregularity of precipitation in the Oued Ouahrane basin cause significant fluctuations in evapotranspiration throughout the year. Evapotranspiration ranges from 40 mm in January to 240 mm in July (Table III.2).

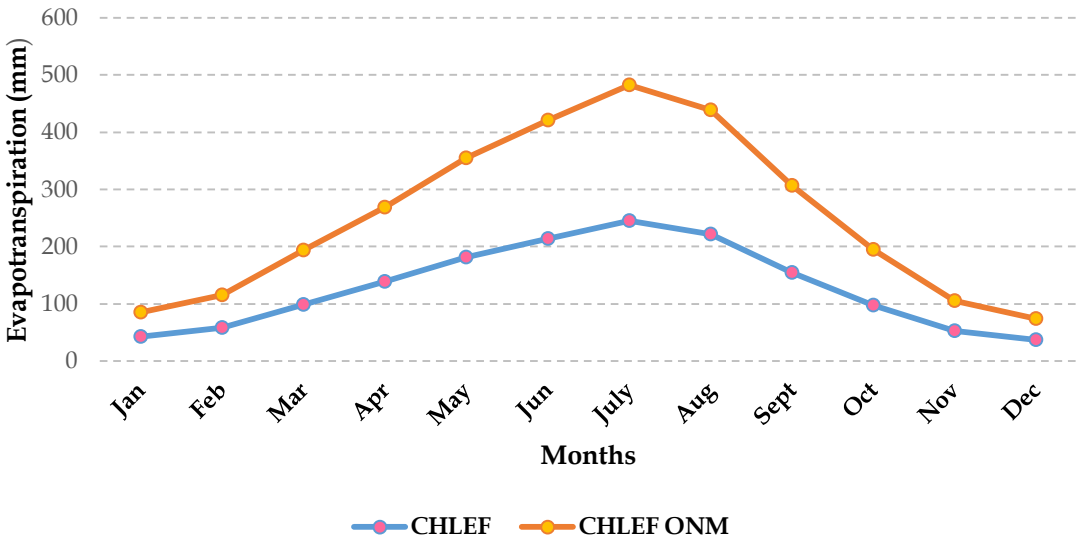

Figure III.12: Interannual averages of evapotranspiration from the wadi Ouahrane basin.

(**1998-2012**).

III.4.3. Relative humidity

February has the highest value of 83% and August has the lowest value of 32%. Relative humidity is a measure of the amount of water vapor present in the air relative to the maximum amount the air could hold at a given temperature.

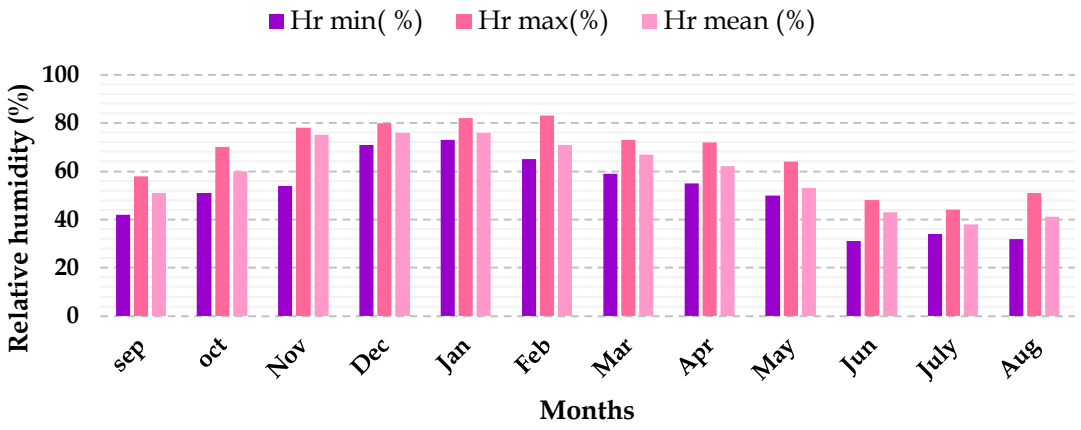

Figure III.13: Monthly relative humidity of the Chlef station. (**1998-2012**).

III.4.4.Wind Speed

The region predominantly experiences northwesterly winds, which tend to bring rain. In contrast, dry southerly winds, known as sirocco, occur during summer and are cold and desiccating in winter. The sirocco winds are present for approximately 17 days per year. The month of June holds the maximum value of average wind speeds with 3.22m / s against the month of January which is estimated at 2.31m / s.

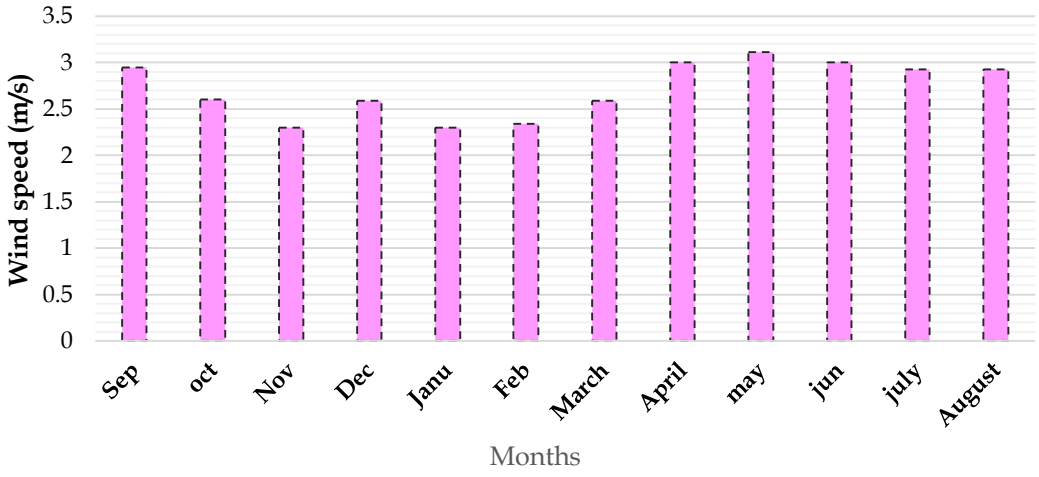

Figure III.14: Monthly average of mean wind speeds at Chlef station. (**1998-2012**).

III.4.5.The precipitations

The climate of Chlef is characterized by hot, dry summers with little storms and mild, wet winters and may be referred to as semi-arid Mediterranean (Troll et al. **1964**).The Wadi Wahrane basin belongs to the medium-temperate semi-arid bioclimate.

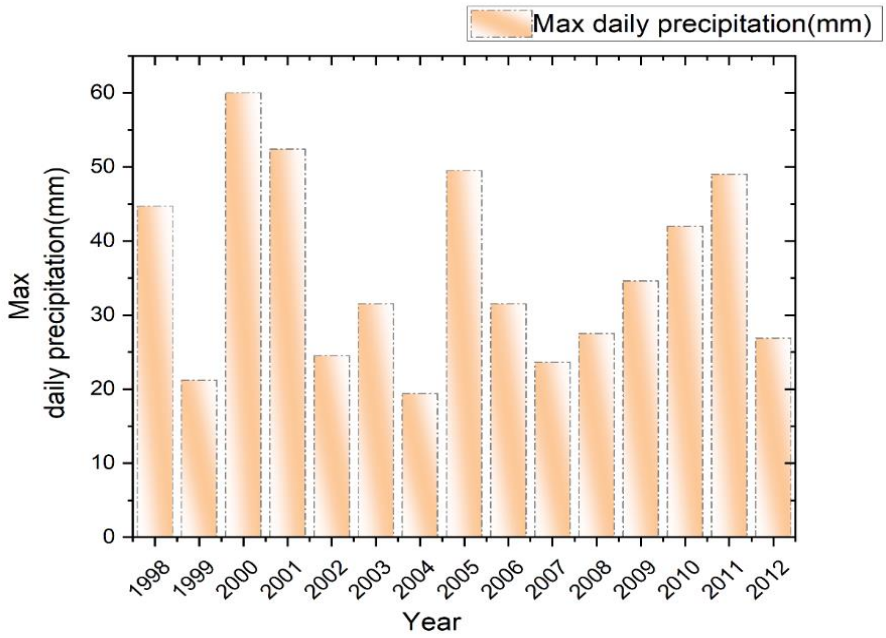

Figure III.15: Histogram of maximum daily rainfall distributions in Wadi ouahrane (**1998-2012**).

III.5.The Data Acquisition and Input Data Preparation

The hydrological data, including daily rainfall (mm) and runoff (m3/s), of the Wadi Ouahrane basin were collected from the National Agency of Water Resources (Agence National des Resources Hydrauliques – ANRH) in Belida, spanning from 1998 to 2012. Additionally, data from the Tropical Rainfall Measuring Mission (TRMM) were utilized as a source of satellite-estimated rainfall information for the Wadi Ouahrane basin during the same period. It was collected from the site: (https://disc.gsfc.nasa.gov/, s.d.)The TRMM satellite collects valuable data about rainfall patterns worldwide.

III.5.1.The choice of the Station Utilized in this Study

The Cheliff-Zahrez hydrographic region in Algeria is monitored through a comprehensive rainfall network consisting of 158 stations, which are managed by the National Agency for Hydraulic Resources (ANRH). These stations are strategically distributed across

various basins within the study region, providing crucial data for hydrological analyses. Accurate precipitation data is essential as it significantly influences hydrological studies, impacting everything from water resource management to flood predicting.

In Our study, we focused on the Wadi Ouahrane basin, examining data from six rainfall stations spanning the period from 1972 to 2018. Through severe testing of these stations, we identified three that were particularly reliable. Among these, the station located in CHLEF, designated by ANRH with the code 012219, was selected for its comprehensive and continuous data record from 1998 to 2012. This station's data was crucial for our analysis due to its consistency and reliability (see Figure III.16 for the station's location). In addition to rainfall data, Runoff data were also exactly collected following the same protocols. This dual approach of using both rainfall and runoff data enables a more robust understanding of the hydrological dynamics within the Wadi Ouahrane basin. The integration of these datasets allows for improved modeling and prediction of hydrological behaviors, essential for effective water resource management in the region.

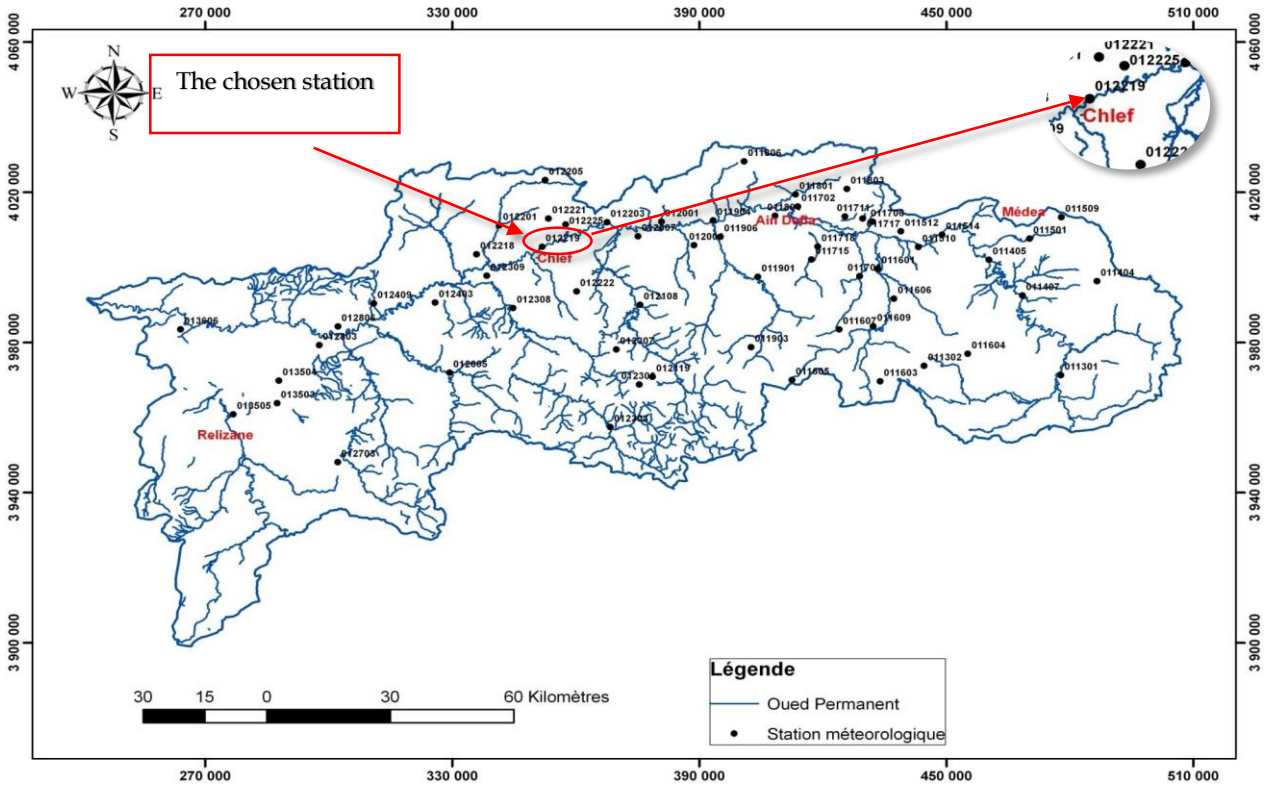

Figure III.16: Localization of Rainfall Stations of the low Cheliff basin.

III.5.2.The input selection

Input selection for data-driven rainfall-runoff is an important task. In this study two different input selection methods were used:

III.5.2.1.Rainfall-runoff as input

We initially used rainfall (pt) as the primary input variable and runoff Qt+1 (m^3/s) as a target in our data. This setup aimed to predict runoff based only on current rainfall data. Unfortunately, the initial results were disappointing, with correlation coefficients between the input rainfall and output runoff being extremely low, these low values indicated a poor relationship and predictive performance. Recognizing the need for a more sophisticated approach, we introduced lagged precipitation values. Specifically, we included rainfall data from the previous days [pt-1, pt-2, and pt-3] as additional input variables. The rationale was that past rainfall could have a delayed effect on current runoff, thereby potentially improving the accuracy, despite this enhancement the correlation coefficient improved only marginally, which was still insufficient for reliable predictions.

III.5.2.2.Runoff as an additional input

To refine our model we decided to incorporate runoff data as an additional input variable. Runoff which represents the portion of precipitation that flows over land surfaces can provide critical information on how rainfall translates into runoff. By adding runoff data from previous days as an input to our model, we observed a significant improvement in its performance. The correlation coefficient between the predicted and actual values increased to 0.96. This high correlation indicates that our model can now capture the Relationship between rainfall and runoff with greater accuracy, reflecting the dynamic nature of hydrological responses to precipitation. This improvement demonstrates the importance of considering multiple hydrological inputs. Here below a demonstration table with the input and output data.

Table III.2: The input selection in situ data with the output.

Models N°	Input vectors (features)	Output (Target)
M1	P_t	$Q_{t+1}(m^3/s)$
M2	Pt-1 , P_t	$Q_{t+1}(m^3/s)$
M3	Pt-2 ,Pt-1 , P_t	$Q_{t+1}(m^3/s)$
M4	Pt-3,Pt-2 ,Pt-1 , P_t	$Q_{t+1}(m^3/s)$
M5	Qt-1,Pt-3,Pt-2 ,Pt-1 , P_t	$Q_{t+1}(m^3/s)$
M6	Qt-2, Qt-1, Pt-3, Pt-2, Pt-1, P_t	$Q_{t+1}(m^3/s)$
M7	Qt-3,Qt-2,Qt-1,Pt-3,Pt-2 ,Pt-1 , P_t	$Q_{t+1}(m^3/s)$
M8	Qt-4,Qt-3,Qt-2,Qt-1,Pt-3,Pt-2 ,Pt-1 , P_t	$Q_{t+1}(m3/s)$
M9	Qt-5,Qt-4,Qt-3,Qt-2,Qt-1,Pt-3,Pt-2 ,Pt-1 , P_t	$Q_{t+1}(m3/s)$

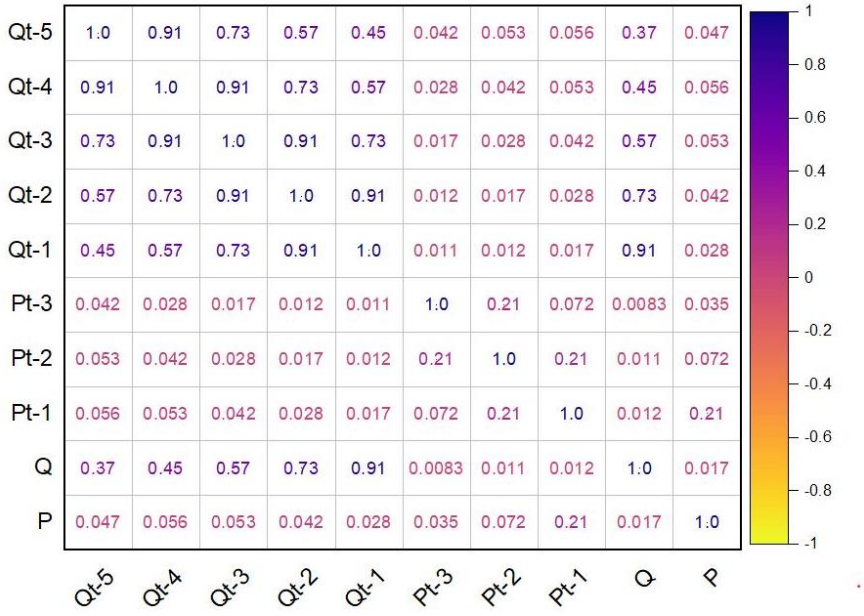

Figure III.17: Correlation plot for the input and target variables in situ-data.

The correlation plot for the input and target variables is shown in Figure III.14 in this figure the diagonal elements of the matrix, all equal to 1.0, represent the perfect correlation of each variable with itself. Off-diagonal elements indicate the degree of correlation between different variables. For example, there is a high positive correlation between the runoff values from successive days, such as Qt-5 and Qt-4 (0.91) and Qt-4 and Qt-3 (0.91), indicating that runoff on consecutive days is strongly related. In contrast, the correlations between precipitation values and runoff values are much lower, such as Pt-3 and Qt-1 (0.011) and Pt-2 and Qt-3 (0.017), suggesting weaker relations

III.6.Integration of TRMM Data

Integrating TRMM data into runoff prediction models can provide valuable insights into rainfall patterns and intensity. Incorporating detailed time-series data, such as $P_{(TRMM)\ t-1}$, $P_{(TRMM)\ t-2}$, $P_{(TRMM)\ t-3}$, etc., as input variables into these models can enhance their accuracy. The output variable, typically represented as Q (runoff), remains consistent and has been utilized in various studies (Su et al**.** **2008;** Habib et al. **2009;** Scheele et al. **2011**). TRMM data is particularly useful for studies on urban hydrology, where high-resolution time-scale data is essential for modeling and design. Among the TRMM rainfall products, types such as 3B40, 3B41, and 3B42 are available, with 3B42 offering the highest spatial (0.25 x 0.25 degree) and temporal (3 hours) resolution. Incorporating TRMM data into runoff prediction models involves combining satellite-based precipitation data with other rainfall data sources to create

a comprehensive and accurate representation of precipitation patterns over a given area. The TRMM data enhances the accuracy of predictions by offering a more comprehensive and spatially distributed depiction of precipitation patterns and by identifying areas of high rainfall variability. This information can then be used to adjust model parameters and improve the accuracy of predictions. By comparing predicted runoff with observed TRMM rainfall data, the integration of TRMM data into runoff prediction models facilitates improved model calibration and validation. This approach not only enhances the accuracy of runoff predictions but also enables a more thorough evaluation of the model's performance. Integrating TRMM data supports model calibration and validation, ensuring that models accurately reflect real-world conditions. This, in turn, enhances our ability to predict runoff behavior and provides decision-makers with actionable insights for sustainable water resource management and infrastructure planning. Ultimately, this contributes to more resilient and adaptive water systems in response to changing environmental conditions.

Table III.3: The input selection in TRMM data with the output.

Models N°	Input vectors (features)	Output (Target)
M1	$P_{(TRMM)t}$	$Q_{t+1}(m^3/s)$
M2	$P_{(TRMM)\ t-1}$, $P_{(TRMM)t}$	$Q_{t+1}(m^3/s)$
M3	$P_{(TRMM)\ t-2}$, $P_{(TRMM)\ t-1}$, $P_{(TRMM)t}$	$Q_{t+1}(m^3/s)$
M4	$P_{(TRMM)\ t-3}$, $P_{(TRMM)\ t-2}$, $P_{(TRMM)\ t-1}$, $P_{(TRMM)t}$	Q_{t+1} (m^3/s)
M5	Qt-1, $P_{(TRMM)\ t-3}$, $P_{(TRMM)\ t-2}$, $P_{(TRMM)\ t-1}$, $P_{(TRMM)t}$	$Q_{t+1}(m^3/s)$
M6	Qt-2, Qt-1, $P_{(TRMM)\ t-3}$, $P_{(TRMM)\ t-2,}$ $P_{(TRMM)\ t-1}$, $P_{(TRMM)t}$	$Q_{t+1}(m^3/s)$
M7	Qt-3, Qt-2, Qt-1, $P_{(TRMM)\ t-3}$, $P_{(TRMM)\ t-2}$, $P_{(TRMM)\ t-1}$, $P_{(TRMM)t}$	$Q_{t+1}(m^3/s)$
M8	Qt-4,Qt-3,Qt-2,Qt-1, $P_{(TRMM)t-3}$,$P_{(TRMM)t-2}$,$P_{(TRMM)t-1}$,$P_{(TRMM)t}$	$Q_{t+1}(m3/s)$
M9	Qt-5,Qt-4,Qt-3,Qt-2,Qt-1, $P_{(TRMM)t-3}$,$P_{(TRMM)t-2}$,$P_{(TRMM)t-1}$,$P_{(TRMM)t}$	$Q_{t+1}(m3/s)$

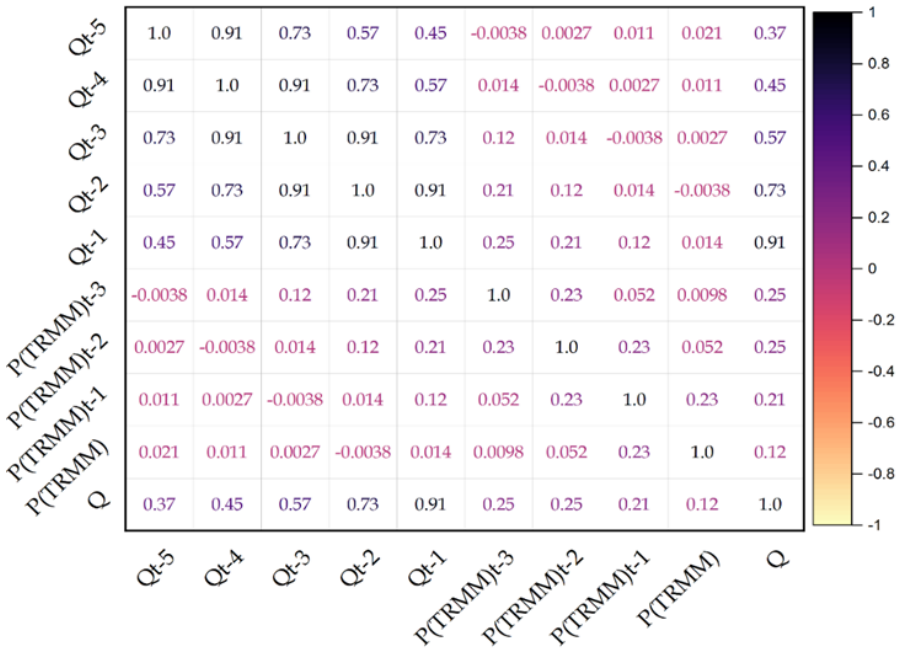

Figure III.18: Correlation plot for the input and target variables in TRMM data.

The correlation plot for the input and target variables is shown in Figure III.15 provides a detailed analysis of the relationships between various runoff and precipitation variables over a period of days. The variables include runoff from the previous five days (Qt-5, Qt-4, Qt-3, Qt-2, Qt-1), precipitation from the previous three days ($P_{(TRMM)t-3}$, $P_{(TRMM)t-2}$, $P_{(TRMM)t-1}$), current runoff (Q), and current precipitation (P(TRMM)). The matrix reveals that there is a strong positive correlation between runoff values on successive days. For instance, the correlation coefficient between Qt-5 and Qt-4 is 0.91, and between Qt-4 and Qt-3 is also 0.91, indicating that runoff on one day is highly predictive of runoff on the following day.

The dataset used in this study comprises 5114 values spanning a period of 14 years. For training purposes, approximately 3573 values, were utilized, accounting for 70% of the dataset. The remaining 1533 values, were allocated for the testing phase, representing 30% of the dataset. The division method chosen, with 30% for validation and 70% for training, aligns with the commonly employed approach in current studies This division ratio strikes a balance between utilizing a sufficiently large dataset for training and ensuring a robust validation process to assess the performance of the algorithms accurately.

III.7.PACF &ACF for the input selection data

Autocorrelation Function (ACF), measures the correlation between observations of a time series separated by different lags. It's a way of identifying the extent to which the current values of the series are related to its past values.

The Partial Autocorrelation Function (PACF) helps to measure the correlation between observations of a time series separated by a specific lag but with the linear influence of intervening lags removed. It provides a clearer picture of the direct relationship between values separated by that lag, without indirect effects.

Here below the PACF & ACF for the datasets

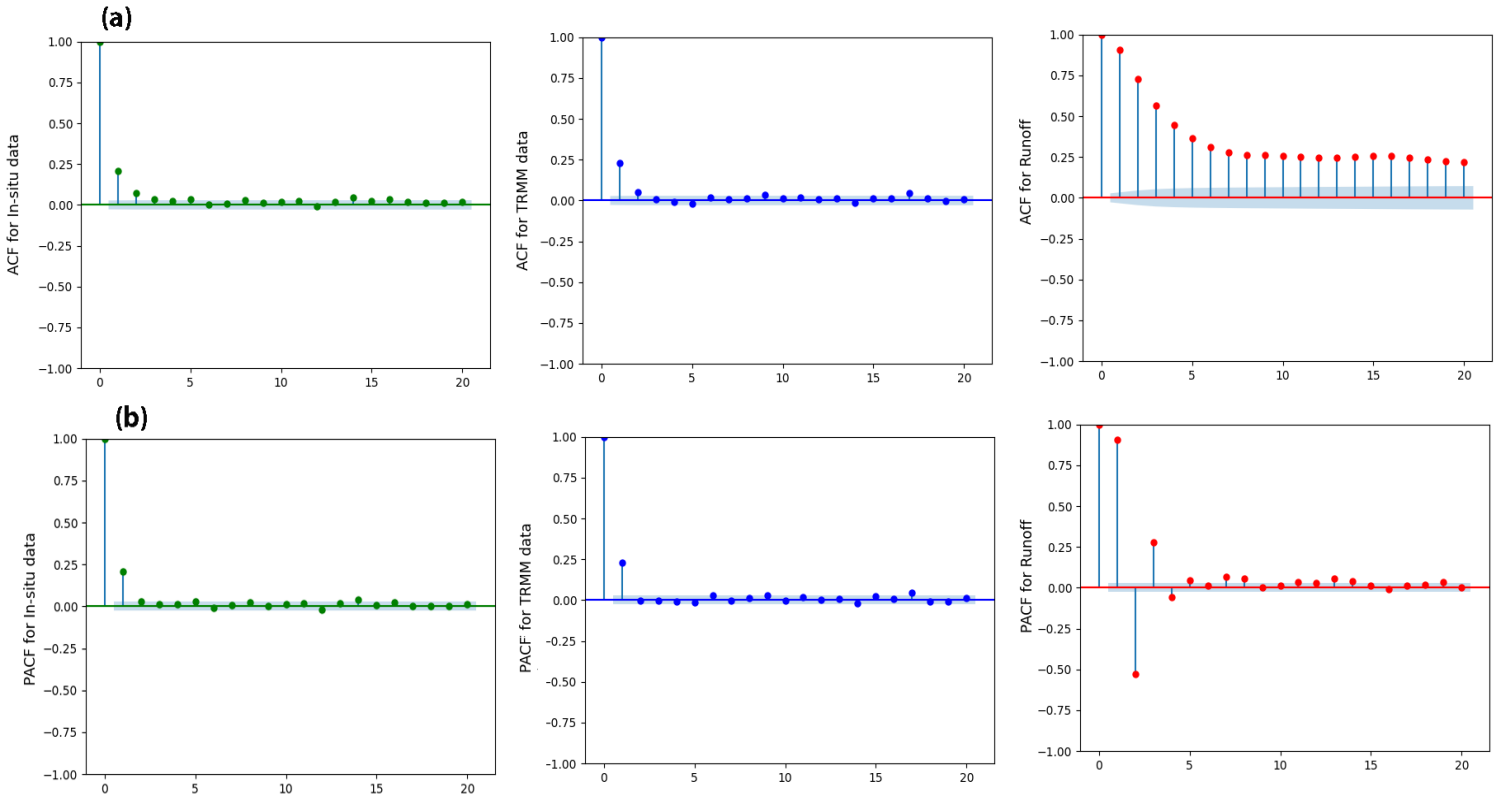

Figure III.19: (a): The ACF Plots for In-Situ, TRMM, and Runoff Data, (b): the PACF Plots for In-Situ, TRMM, and Runoff Data.

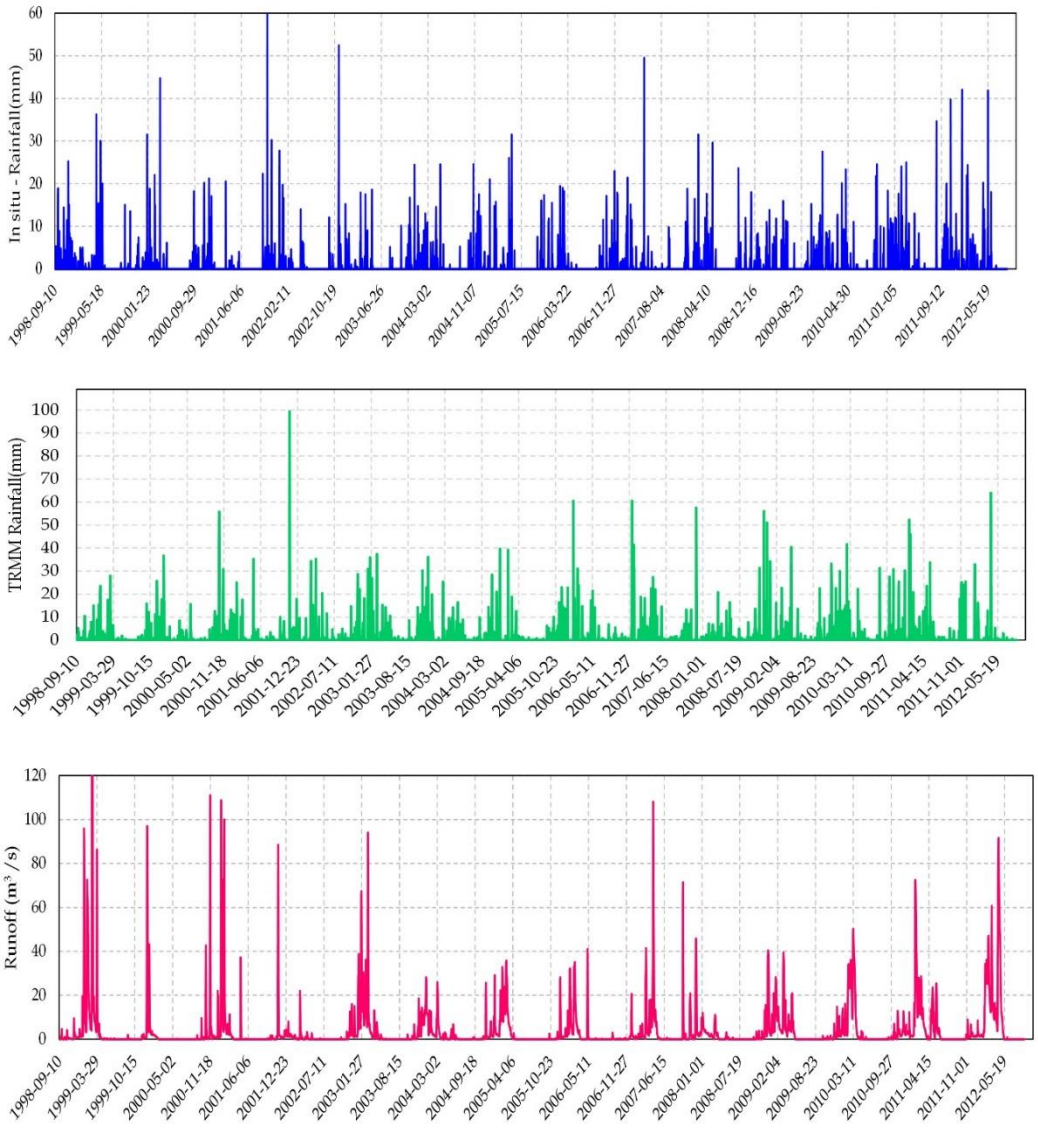

FigureIII.20: Time series of the In-situ rainfall, TRMM, Runoff datasets.

Table III.4: Statistical characteristics of daily TRMM rainfall, in situ rainfall, and runoff data used in the analyse.

Databases		Mean	Max	Min	STD	Var	CV
Rainfall	Train	0.897	60.00	0.00	3.585	12.851	3.997
	Test	1.10	42.00	0.00	3.73	13.93	3.402
TRMM	Train	1.156	99.394	0.00	4.703	22.117	4.069
	Test	1.382	64.006	0.00	5.382	28.971	3.896
Runoff	Train	3.600	186.750	0.00	11.874	140.982	3.298
	Test	5.277	91.600	0.00	11.033	121.724	2.091

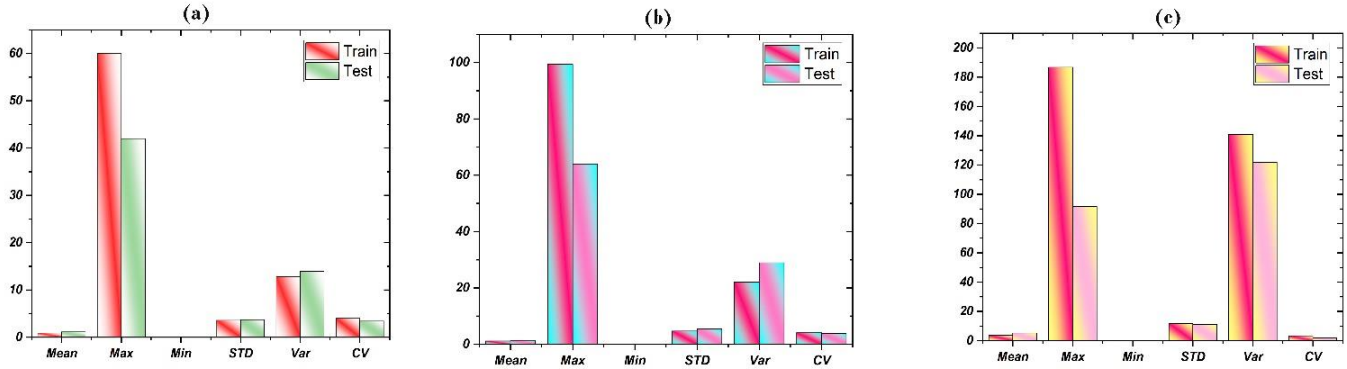

Figure III.21: Statistical characteristics of Databases: (a) in situ rainfall, (b); TRMM and(c), runoff data used in the analyse.

III.8.Machine learning methods

Machine learning models are algorithms that can learn patterns from data and make predictions or decisions without being explicitly programmed. These models can be broadly categorized into supervised learning, unsupervised learning, and reinforcement learning. Here, we'll introduce three specific types of machine-learning models:

III.8.1.Long Short -Term Memory Neural Network- (LSTM)

The LSTM network is a variation of the recurrent neural network (RNN) that uses a directed cycle structure to transfer the output of a hidden layer back to the same hidden layer. This approach helps identify features and time series (Salehinejad et al **2017**), information from the signals of previous time series. Hochreiter and Schmidhuber (Hochreiter et al. **1997**), introduced LSTM to overcome the issue of gradient disappearance by using memory cells. The cell states are updated through gating regulations consisting of three gates: the input gate determines which information will update the current block state and which new datasets will be included as inputs; the forget gate controls which information should be preserved or discarded; and the output gate decides which outputs to generate. The advantage of LSTM lies in its ability to learn from long-term dependencies in time series data, making it successful in various fields such as rainfall-runoff modeling in hydrology.

LSTM consists of a chain of repeating LSTM cells, each transferring the memory cell (C) and hidden state (h) to the next LSTM cell. Each LSTM cell is contains a forget gate (f-t), an input gate (i-t), and output gate (o-t). The architecture of an LSTM cell is shown in Figure below.

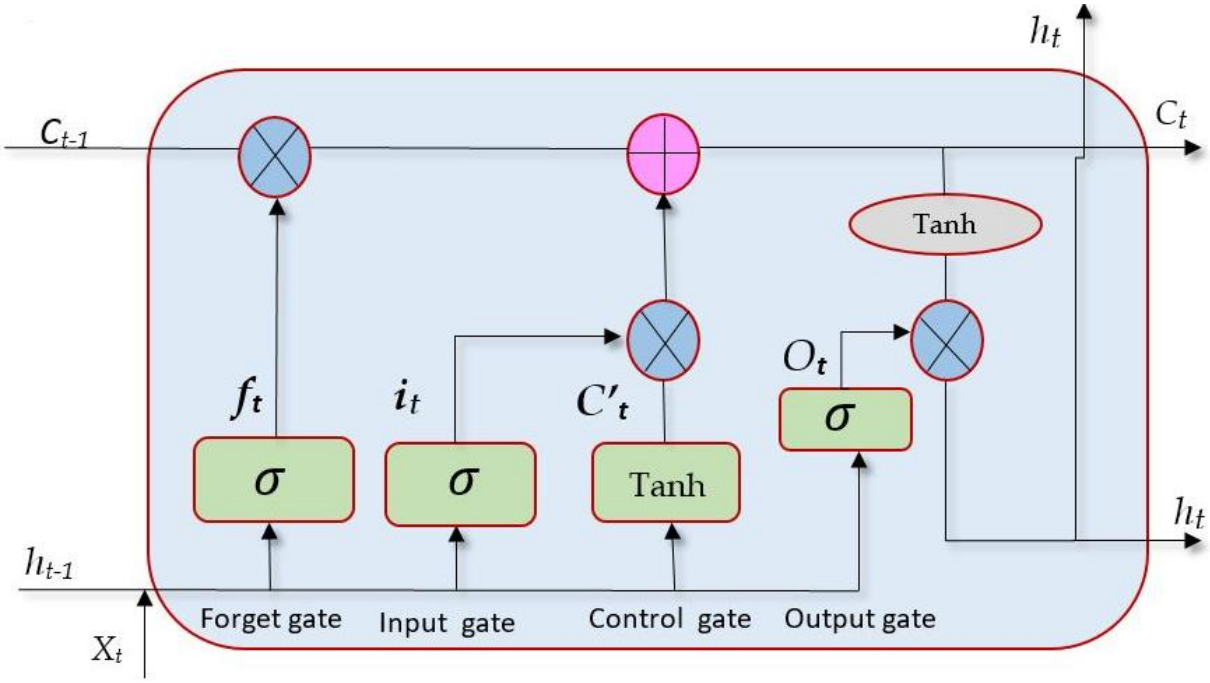

Figure III.22: The basic structure of LSTMNN.

The following equations were used in LSTM:

The input gate, it, is designed to add new information for updating memory cell, Ct. defined as:

$$it = \sigma(Wi\,.\,[ht-1, x\_t\,] + bi) \quad \textbf{(III.10)}$$

Where σ is the sigmoid activation function, which constrains the output of the gate between 0 and 1. $\boldsymbol{W_i}$ is the weight matrix for the input gate. $\boldsymbol{[h_{t-1}, x_t]}$, is the concatenated input vector, including the previous hidden state $\boldsymbol{h_{t-1}}$and the current input x_t. $\boldsymbol{b_i}$ is the bias term for the input gate.

The forget gate, *ft*, determines the extent to which information is discarded for the Memory cell, C, defined as:

$$ft = \sigma(Wf\,.\,[ht-1, xt] + bf \quad \textbf{(III.11)}$$

Where $\boldsymbol{\sigma}$ is the sigmoid activation function, which ensures the forget gate's output is a value between 0 and 1.and $\boldsymbol{W_f}$ is the weight matrix for the forget gate. , $\boldsymbol{[ht-1, xt]}$ is the concatenated

input vector, including the previous hidden state $h_{t-1}$and the current input $x_{t.}$, b_f is the bias term for the forget gate.

The output gate *ot***,** outputs the value at each moment ***t*.** The formula for obtaining the output gate is as follows

$$ot = \sigma(Wo \cdot [ht - 1, xt] + bo) \quad \textbf{(III.12)}$$

Where $\boldsymbol{\sigma}$ is the sigmoid activation function, which ensures the output gate's output is a value between 0 and 1. $\boldsymbol{W_o}$ is the weight matrix for the output gate. $\boldsymbol{[h_{t-1}, xt]}$ is the concatenated input vector, including the previous hidden state $\boldsymbol{h_{t-1}}$and the current input $\boldsymbol{x_t}$. $\boldsymbol{b_o}$ is the bias term for the output gate.

The memory cell state $\boldsymbol{C_t}$, at time step t is updated by considering the previous memory cell state $\boldsymbol{C_{t-1}}$, the input gate $\boldsymbol{i_t}$, and the forget gate $\boldsymbol{f_t}$. The update process for the memory cell state, defined as:

$$Ct \ = \ ft \, . Ct - 1 \ + \ it . Ct' \quad \textbf{(III.13)}$$

$$Ct' \ = \ tanh \, (Wc \, . [ht - 1, xt] \ + \ b \quad \textbf{(III.14)}$$

Where *tanh* represents the hyperbolic tangent activation function. The subscripts *i* and *c* denote the input gate and new candidate value, C_t', respectively.

The output Vectors, $\boldsymbol{o_t}$, and memory cell, $\boldsymbol{C_t}$, determines the hidden state, ht, which is expressed as:

$$ht \ = \ ot \, . Tanh \, (Ct) \quad \textbf{(III.15)}$$

III.8.2.Extreme Gradient Boosting- (XGBoost)

XGBoost, which stands for eXtreme Gradient Boosting, is a powerful and popular machine-learning algorithm primarily used for supervised learning tasks such as classification and regression. Proposed by Chen and Guestrin in 2016, it is an improvement from the gradient-boosting decision tree algorithm (GBDT). XGBoost is rapid and precise learning making it a superior machine-learning model in data sciences, including hydro-meteorological modeling. XGBoost is an ensemble learning method that combines

predictions from multiple models (usually decision trees) to minimize the loss function of the last tree (Yang et al. 2020).

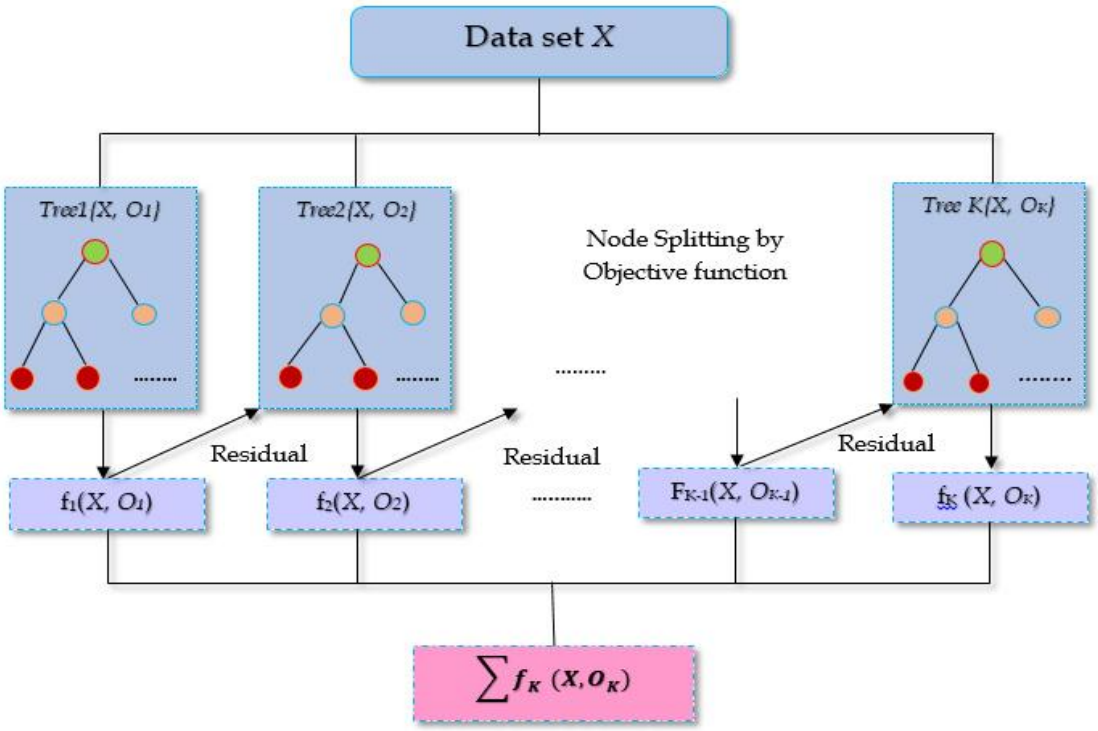

Figure III.23: A general architecture of XGBoost.

XGBoost is a tree ensemble model using K additive models, and its predicted values can be written as

$$y = \sum_{K=1}^{K} fk(x) \quad \textbf{(III.16)}$$

Where *fk* corresponds to a tree structure with T leaves and leaf weights,ω.

A major difference between XGBoost and GBDT is that they use different objective Functions. A regularization term is added for the XGBoost model, expressed as:

$$Obj = \sum_{i=1}^{N} l(yi\,, di\,) + \sum_{K=1}^{K} \Omega(fk) \quad \textbf{(III.17)}$$

Where l is the loss function measuring the distance between the predicted value, y, and Target value, d, such as the mean-square error used in this study. The second-order Taylor Expansion is performed in the loss function to ensure its accuracy. The second Term, $\sum_{K=1}^{K} \Omega(fk)$ Sums up the complexity of each base function, f, to avoid overfitting, defined as:

$$\Omega(f) = \gamma T + \frac{1}{2}\lambda \, \|\omega\|^2 \quad \textbf{(III.18)}$$

Where γ and λ are penalty parameters, controlling the number of leaves, T, and the $L2$ norm of the leaf weights, w, respect

III.8.3.Multi-layer Perceptron Neural Network- (MLPNN)

MLP is a sort of artificial neural network that is made up of several layers of linked nodes, or neurons (Gardner et al. 1998), since it is a feed-forward neural network, data goes from the input layer to the hidden layers and finally to the output layer. Each neuron in the MLP conducts a weighted sum of its inputs, applies an activation function to the sum, and then transmits the outcome to the neurons in the next layer. An MLP consists of three layers: the input layer contains n input values; the hidden layer, positioned between the input and output layers, varies in size depending on the problem type; and the output layer, which sums the results of the MLP network.

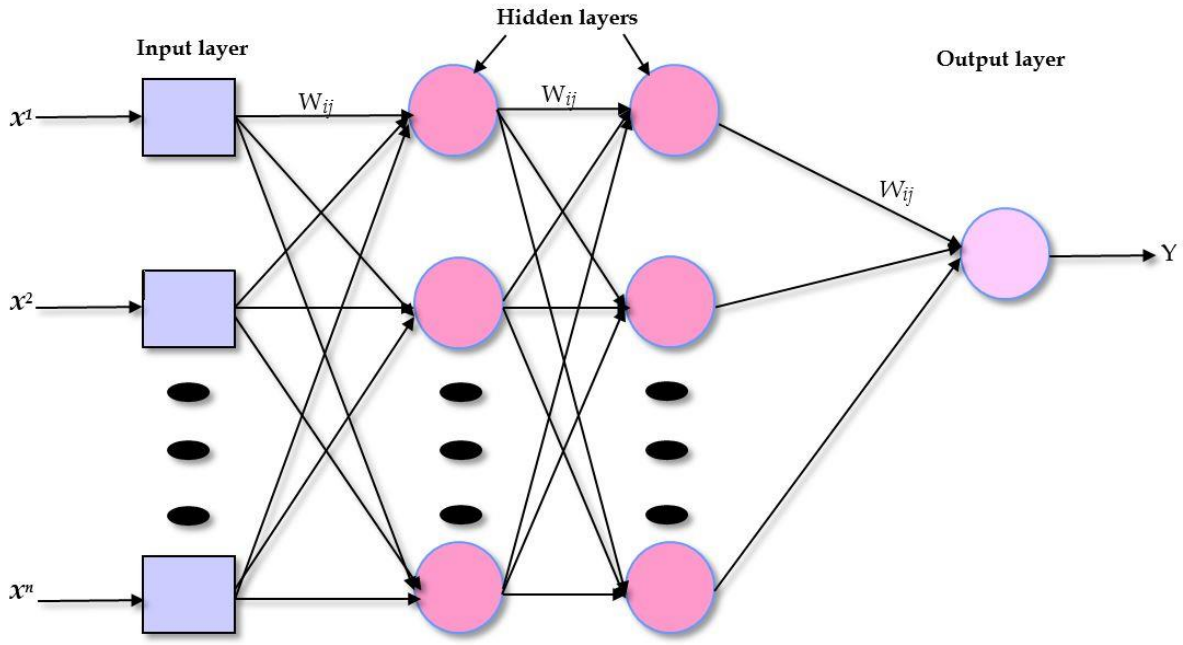

Figure III.24: Multilayer perceptron (MLP) architecture with two hidden layers and one prediction output.

The input layer simply passes the input features to the next layer. The input to the neural network is represented as a vector, where n is the number of input features.

$$x = [x^1, x^2, \ldots . x^n] \quad \textbf{(III.19)}$$

A Hidden layer consists of multiple neurons. The output of each neuron in a hidden layer can be calculated using the equation:

$$zj = i = \sum_{j=1}^{n} wjixi + bj \quad \textbf{(III.20)}$$

Where zj: represents the weighted sum of inputs for neuron j, wji: means the weight connecting input ii to neuron j, xi: is the input feature ii. And bj: is the bias term for neuron j. After calculating the weighted sum, the neuron applies an activation function to introduce non-linearity:

$$aj = \sigma(zj) \quad \textbf{(III.21)}$$

Where aj is the output of the j-th neuron in the hidden layer, and $\sigma$is the activation function (e.g., ReLU, Sigmoid, or Tanh).

The output layer of an MLP produces the final predictions or outputs of the network. The number of neurons in the output layer depends on the task being performed, each neuron in the output layer receives input from the neurons in the last hidden layer and applies an activation function. The output layer calculates the final output using the same process as the hidden layers. The activation function applied in the output layer for regression tasks, a linear activation function may be calculated using the equation:

$$ak = zk \quad \textbf{(III.22)}$$

The loss function serves as a guide for the network during training, quantifying the disparity between predicted outputs and actual target values. Its choice depends on the nature of the task at hand. For instance, in regression tasks, the Mean Squared Error (MSE) is commonly used.

III.9.Optimization Parameter

Hyper-parameter optimization in machine learning is to find the best hyper-parameters for a given machine learning algorithm which gives the best performance when evaluated on a validation set. Hyper-parameter optimization is expressed in the form of the equation as:

$$X^* = argmin\ f(x) \quad \textbf{(III.23)}$$

Here f(x) represents an objective score to minimize that is evaluated in the validation set; x_ is a set of hyper-parameters that yields the lowest score value, and x can take any value in the X domain. In simple terms, we want to find the model hyperparameter that give the best score on the validation set metric. The issue with hyper-parameter optimization is that it is extremely costly to evaluate the objective function to find the score.

III.9.1. LSTM hyper parameter tuning

Table III.5: List of hyperparameter values LSTM.

Hyper parameters	Value (Rang)	Description
Epoch	500	Is the number of times the entire dataset is passed forward and backward through the neural network.
Batch size	32	The batch size determines the number of samples that will be propagated through the network before updating the model parameters.
Optimizer solver	Adam	The solver defines the optimization algorithm used for training the mode
Learning rate	0.001	Controls the step size during the optimization process.
Verbose	2	This parameter controls the amount of information printed during the training process

III.9.2. XGBoost hyperparameter tuning

Several researchers found that hyperparameter values greatly impact the model accuracy (Zhang.w, et al, .2021). Therefore, optimal hyperparameter, which may be found by hyperparameter tuning, are required. Grid search, random search, and Bayesian optimization are the three most common methods to optimize hyper parameters.

Table III.6: List of hyperparameter values XGBoost.

Hyperparameter	Value (Rang)	Description
Max depth	[3,10,0]	Maximum depth of a tree increasing the value makes the model more complex
Learning rate (eta)	[0.1,0.01,0.001]	Controls the step size at each iteration to prevent overfitting, lower value requires more trees
Col-sample-bytree	[0.8,0.9,1]	Fraction of features sampled for each tree. Similar to max-features in Random forest

n-estimators	[10,200,300]	Number of boosting rounds or trees to build too many leads to overfitting

III.9.3.MLP hyperparameter tuning

Hyperparameter tuning task in MLP include solving optimization problems. It involves adjusting the values of hyperparameter such as the number of hidden layers, the number of nodes in each layer, and the learning rate…e.g,

Table III.7: List of hyperparameter values of MLP**.**

Hyperparameter	Value (Range)	Description
Hidden –layer-size	[100-50]	This parameter specifies the number and size of hidden layers in the neural network. It includes the number of hidden layers and the number of units (neurons) in each layer.
Solver	Levnberg-Marquardt	The solver defines the optimization algorithm used for training the model
Max-iter	1000	Specifies the maximum number of iterations (epochs) the training algorithm will go through.
Learning –rate-int	0.001	Controls the step size at each iteration to prevent overfitting, lower value requires more trees.

III.10.Evaluation Metrics

Evaluation metrics are essential tools in assessing the performance of models. So several performance metrics were utilized to assess model effectiveness, including Mean Absolute Error

(MAE), Root Mean Square Error (RMSE), Nash-Sutcliffe Efficiency (NSE), and the Correlation Coefficient (R). Below are concise explanations of each performance measure.

- ✓ **Mean Absolute Error (MAE):**

  The Mean Absolute Error metrics measures the average absolute difference between predicted and actual values.

$$MAE = \frac{1}{N}\sum_{i=1}^{N}\|(Qo,i) - (Qs,i)\|, \quad 0 \le MAE \le +\infty \qquad (\mathbf{III.24})$$

- ✓ **Root Mean Square Error (RMSE):**

  The RMSE is introduced as an index that shows the absolute error between observed and simulated values. The value of this index varies between [0, 1]. The best value for this indices is 0, in general, the minimal this value, the optimum the

$$RMSE = \sqrt{\frac{1}{N}\sum_{i=1}^{N}\left[(Q_{o,i}) - (Q_{s,i})\right]^2}, \quad 0 \le RMSE \le +\infty \qquad (\mathbf{III.25})$$

- ✓ **Nash-Sutcliffe Efficiency (NSE):**

  The Nash–Sutcliffe (NSE) coefficient is one of the most common indices used to evaluate the efficiency of hydrological activities.

$$NSE = 1 - \frac{\sum_{i=1}^{N}\left[(Q_{o,i}) - (Q_{s,i})\right]^2}{\sum_{i=1}^{N}\left[Q_{o,i} - \overline{Q_o}\right]^2}, \qquad -\infty \le NSE \le +1 \qquad (\mathbf{III.26})$$

- ✓ **Correlation Coefficient (R):**

  The coefficient of determination (R) varies from 1 to 0 and the optimum amount is 1, and this is the case when the simulation amount is exactly the same as the accorded amount.

$$R = \frac{\sum_{i=1}^{N}(Q_{o,i} - \overline{Q_o})\,(Q_{s,i} - \overline{Q_s})}{\sqrt{\sum_{i=1}^{N}(Q_{obs,i} - \overline{Q_{obs}})^2 \;\sum_{i=1}^{N}(Q_{s,i} - \overline{Q_s})^2}}, \quad -1 \le R \le +1 \qquad (\mathbf{III.27})$$

In these equations, $Q_{o,i}$ *and* $Q_{s,i}$ represent the observed and simulated observations, respectively. N is the sample size of the time series. $\overline{Q_o}$ And,$\overline{Q_s}$, represent the mean values and standard deviation of the observed and simulated observations, respectively.

III.11. Conclusion

In this Third chapter, we provided a detailed analysis of the study area's geomorphological and climatic features, essential for understanding the region's hydrological dynamics. The integration of TRMM data and advanced machine learning models (LSTMNN, XGBoost, and MLP) demonstrates a sophisticated approach to data analysis and prediction. By meticulously selecting and optimizing input data and parameters, the study aims to enhance the accuracy and reliability of hydrological predictions. The findings from this chapter lay a solid foundation for further research and practical applications in hydrology and environmental management, showcasing the importance of combining traditional geographical studies with modern data-driven techniques.

Chapter IV: Results and Discussion

Chapter IV: Results and discussion

IV.1.Introduction

In this chapter, we examine the results of applying machine learning algorithms to in situ data and TRMM rainfall-runoff data. Our analysis focuses on evaluating the performance of three algorithms: XGBoost, MLP Network, and LSTM Neural Network. By exploring the RMSE values in the test phases for each algorithm, we aim to assess their accuracy and reliability in modeling the data sets. Additionally, we compare the outcomes across the in situ and TRMM data to identify the most effective approaches for each context. This analysis helps us understand the strengths and limitations of different machine learning methods for predicting key variables in these data sets.

IV.2.Results analysis from In Situ Data & TRMM in ML Approach

In this particular section, the outcomes derived from implementing XGBoost, MLP, and LSTM on both datasets are presented. These algorithms have been employed to predict runoff discharge in our study area. The effectiveness of each algorithm is evaluated based on various statistical measures and their ability to capture the complex connections between input and output variables is compared.

IV.2.1.Results of the in situ – data

IV.2.1.1.Extreme Gradient Boosting-XGBoost

The Examination of the NSE for the training and test datasets offers insights into the performance of XGBoost models, M1 through M9. As models progress through the iterations, improvements in predictive ability become obvious.

The training set shows a steady increase in NSE values across the nine models, indicating improvement in accuracy. Notably, Models M8 and M9, stand out with the highest NSE values of 0.9425 and 0.9441, respectively. These positive values indicate that Models M8 and M9 are good at capturing the observed variability within the training data, highlighting an excellent ability to predict. On the other hand, in the test set, the NSE values present a contrast to those in the training set, as models M1 to M4 yield negative NSE values of -0.0209 and -0.0194, respectively, which indicate a less effective performance compared to the training set. However, Models M5 to M9 maintain positive NSE values, indicating that these models

keep some predictive efficiency when working with new data. Among them, model M9 stands out with the highest NSE value of 0.8959. This means relative preservation of predictive efficiency on unseen data, with M9 maintaining a notable capacity to represent the underlying patterns. The negative NSE values for other models in the test set indicate room for improvement, suggesting that further model modification may increase their generalization capabilities. Therefore, the NSE analysis highlights the robust predictive efficiency of Models M8 and M9 on both the training and test datasets, while the others might need some improvements.

The RMSE Analysis reveals a consistent trend of accuracy across the XGBoost models M1 to M9 in both training and test datasets. In the training set, model performance, peaked with Models M8 and M9, which achieved remarkably low RMSE values of 2.849 and 2.809, respectively. These values signify the exceptional accuracy of these models in predicting the target variable on familiar data. The strong performance of M8 and M9 extends to the test set, where they continue to excel with the lowest RMSE values. These models demonstrate an impressive ability to generalize effectively to new, unseen data. Although other models in the test set exhibit slightly higher RMSE values, the overall narrative highlights the reliability and robust predictive accuracy of Models M8 and M9.In essence, the RMSE analysis tells an engaging story of precision, with these top models M8 and M9 consistently providing accurate predictions on both familiar and new datasets.

The MAE analysis provides valuable insights into the predictive accuracy of the XGBoost models M1 to M9 across both training and test datasets. In the Training set, there is a clear pattern of decreasing MAE values across the models, reaching a peak with Models M8 and M9, which achieve impressively low MAE values of 0.964 and 0.942, respectively. These values reflect the exceptional precision in capturing the absolute errors between predicted and actual values on the training data, positioning Models M8 and M9 as standout performers in minimizing discrepancies. Moving to the test set, the trend continues, with Models M8 and M9 maintaining the smallest MAE values. This underscores their ability to deliver accurate predictions on familiar data, while also highlighting their flexibility in keeping precision when faced with previously unseen observations. While other models may exhibit slightly higher MAE values in the test set like M5 and M6 low values of 1.5050 and 1.4880, respectively. The overall narrative underscores the reliability and superior predictive accuracy of Models M8 and M9. In summary, the MAE analysis is defined as a compelling story of precision, with

Models M8 and M9 consistently highlighting exceptional accuracy on both training and test datasets.

The analysis of R and the R^2 values for the XGBoost models from M1 to M9 across both the training and test datasets provides a comprehensive view of the models' ability to establish linear relationships and explain variability. In the training set, R values show a consistent increase across models, peaking with Models M8 and M9, which highlights a significant correlation with the target variable. These high R values indicate a strong linear fit to the training data. Similarly, R^2 values steadily increase, reaching their highest points again with Models M8 and M9, representing an increasing amount of explained variability. This signifies that these models not only establish strong linear relationships but also effectively capture a significant portion of the data's variability. The compelling story extends effortlessly to the test set, where Models M8 and M9 maintain their power with the highest R and R^2 values. This consistency underscores their resilience in preserving strong linear relationships and explanatory power when confronted with unseen data. While other models may exhibit slightly lower R and R^2 values in the test set like M3 and M4 lower values of R 0.0880 and 0.0820 respectively, and for R^2 0.0077 and 0.0067 respectively, the overarching theme highlights the reliability and strength of Models M8 and M9 in establishing and maintaining strong linear correlations. In essence, the R and R^2 analysis tells a compelling level of strong linear relationships and high descriptive power, With Models M8 and M9 taking the lead roles in both the training and test datasets. Here is the radar plot of the performance parameters.

Table IV.1: Performance criteria of XGBoost during train and test phases.

		NSE	RMSE	MAE	R	R^2
M1	**Train**	0.0010	11.8790	5.1720	0.0590	0.0035
	Test	-0.0209	11.1580	6.0090	0.0890	0.0079
M2	**Train**	0.0115	11.8160	5.1400	0.1380	0.0190
	Test	-0.0170	11.1370	5.9710	0.0880	0.0078
M3	**Train**	0.0159	11.7890	5.1380	0.1610	0.0258
	Test	-0.0161	11.1310	5.9630	0.0880	0.0077
M4	**Train**	0.0561	11.5460	4.9400	0.4480	0.2008
	Test	-0.0194	11.1490	5.9380	0.0820	0.0067
M5	**Train**	**0.7871**	**5.4840**	**1.6270**	**0.8900**	**0.7920**
	Test	**0.9022**	**3.4540**	**1.5050**	**0.9540**	**0.9106**
M6	**Train**	0.9238	3.2810	1.0730	0.9610	0.9240
	Test	0.8928	3.6150	1.4880	0.9510	0.9050
M7	**Train**	0.9297	3.1500	1.0460	0.9640	0.9303
	Test	0.8974	3.5370	1.4610	0.9530	0.9090
M8	**Train**	0.9425	2.8490	0.9640	0.9710	0.9430

	Test	0.8961	3.5600	1.4580	0.9520	0.9062
M9	**Train**	0.9441	2.8090	0.9420	0.9720	0.9447
	Test	0.8959	3.5630	1.4750	0.9540	0.9093

In the XGBoost, the performance metrics for Model 5 on both the training and test datasets display its extraordinary predictive capabilities. In the training set, Model 5 achieves an NSE of 0.7871, indicating a strong ability to capture the variability in the observed data. The RMSE of 5.4840 and MAE of 1.6270 further emphasize the model's accuracy in minimizing prediction errors. The *R* stands at 0.8900, indicating a strong linear relationship between predicted and actual values, while the R^2 reaches 0.7920, indicating that Model 5 explains a substantial portion of the variance in the target variable. The generalization abilities of Model 5 to unseen data are impressive, as evidenced by its performance on the test set. The NSE increases to 0.9022, signifying higher predictive efficiency on new observations. The RMSE decreases to 3.4540, and the MAE drops to 1.5050, indicating a successful adaptation of the model to the test set with minimized errors. The high values of *R* at 0.9540 and R^2 at 0.9106 highlight the model's ability to establish strong linear relationships and explain a significant proportion of the Variability in the test data

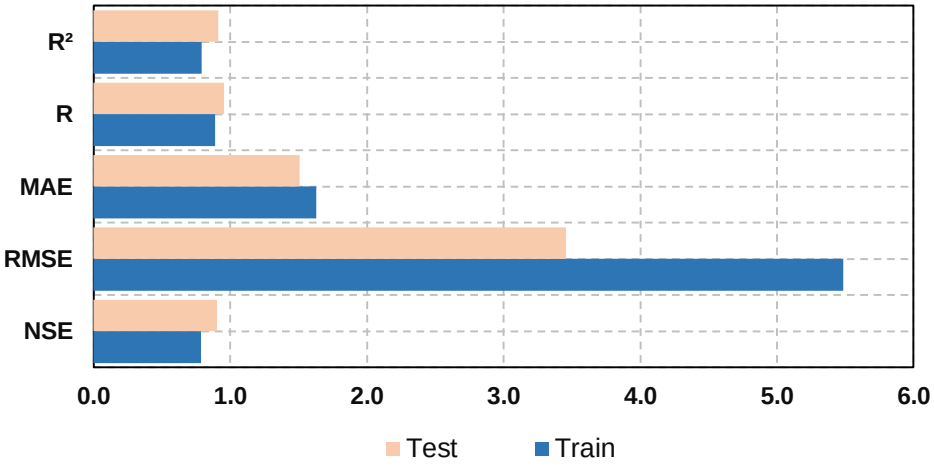

Figure IV.1: Bar graph representation of the performance parameter for model 5.

In conclusion, XGBoost Model 5 emerges as the best-performing model based on the provided metrics, highlighting its efficacy in both training and test datasets. Its strong predictive performance and generalization capabilities make it a standout choice for applications requiring accurate and reliable predictions.

IV.2.1.2.Multi-layer Perceptron Network -MLP

The NSE analysis provides a comprehensive evaluation of the MLP models (M1 to M9) across both training and test datasets. In the training set, NSE values vary, with Models M5 to

M9 showing significantly higher proficiencies. Models M5 and M9 stand out with NSE values of 0.7870 and 0.8630, respectively, demonstrating their adeptness at capturing underlying patterns in the training data. These models exhibit precise predictions, while Models M1 to M4 have lower NSE values of 0.0010 and 0.0120, suggesting areas for improvement in their predictive abilities on the training set. Turning attention to the test set, Models M5 to M9 maintain their superior predictive efficiencies, with Model 5 continuing to display outstanding performance with an NSE of 0.9221. Models M6 to M9 also demonstrate commendable NSE values on the test set, signifying their ability to generalize effectively to new data. Attractively, Models M7 to M9 improve in NSE on the test set 0.9420 and 0.9268, respectively, which shows an extensive comparison to the training set, highlighting their adaptability and strong predictive abilities. However, the NSE analysis highlights the models' changing degrees of predictive efficiency, with Models M5 to M9 indicating a notable strength, particularly on the test set. Model 5 emerges as a consistent standout, highlighting its potential for accurate predictions on both familiar and new datasets.

The RMSE Analysis for the MLP models M1 to M9 across both training and test datasets provides key insights into the models' prediction accuracy. In the training set, RMSE values show a range across models, with Models M5 to M9 showcasing consistently lower errors 5.4840 and 4.3920 respectively, indicating their ability in minimize prediction discrepancies. Particularly, Model 5 stands out with an RMSE of 5.4840, highlighting its precision in predicting the target variable on the training data. Similarly, Models M1 to M4 exhibit comparatively higher RMSE values 11.8770 and 11.8140 respectively, suggesting potential areas for improvement in their accuracy on the training set. Shifting the focus to the test set, Models M5 to M9 maintain their excellence in minimizing errors, with Model 5 continuing to display outstanding performance with an RMSE of 3.0830. Models M6 to M9 also demonstrate commendable RMSE values on the test set, highlighting their ability to generalize effectively to new and unseen data. Notably, Models M7 to M9 display substantial improvements in RMSE on the test set compared to the training set, indicating their adaptability and accuracy in novel scenarios. Well, the RMSE analysis underscores the varying degrees of accuracy in predictions, with Models M5 to M9 showcasing notable strengths, particularly on the test set. Model 5 emerges as a consistent standout, emphasizing its potential for precise predictions on both familiar and new datasets.

The analysis of MAE values for the training and test datasets provides a comprehensive understanding of the accuracy of the MLP models from M1 to M9. In the training set, MAE

values display a range across models, with Models M5 to M9 consistently showcasing lower absolute errors 1.5490 and 1.2910 respectively, indicating their effectiveness in minimizing discrepancies between predicted and actual values. Model 5, in particular, stands out with a remarkably low MAE of 1.5490, emphasizing its precision in predicting the target variable on the training data. Equally, Models M1 to M4 exhibit comparatively higher MAE values 5.1820 and 5.1450 respectively, signifying opportunities for improvement in their accuracy on the training set. Transitioning to the test set, Models M5 to M9 maintain their excellence in minimizing absolute errors, with Model 5 continuing to exhibit outstanding performance with an MAE of 1.2860. Models M6 to M9 also demonstrate commendable MAE values on the test set, highlighting their ability to simplify effectively to new and unseen data. Particularly, Models M7 to M9 display substantial improvements in MAE on the test set compared to the training set, indicating their adaptability and improved accuracy in novel scenarios. The MAE analysis highlights the changing degrees of accuracy in predictions, with Models M5 to M9 highlighting notable strengths, particularly on the test set. Model 5 occurs as a consistent standout, highlighting its potential for precise predictions with minimized absolute errors on both familiar and new datasets.

The Investigation of the R and the R^2, values for the MLP models M1 to M9 in both the training and test datasets provides insights into the models' abilities to establish linear relationships and explain variability. In the training set, R values display variability across models, with Models M5 to M9 demonstrating higher correlations 0.8870 and 0.7870 respectively, signifying their efficiency in establishing stronger linear relationships with the target variable. Model 5, in particular, stands out with an R-value of 0.8870, suggesting a strong linear correlation in the training data. On the other hand, Models M1 to M4 exhibit comparatively lower R-values 0.0350 and 0.115 respectively, indicating potential room for improvement in capturing linear relationships on the training set. Turning to the test set, Models M5 to M9 sustain their excellence in linear relationships, with Model 5 continuing to exhibit outstanding performance with an R-value of 0.6300. Models M6 to M9 also demonstrate commendable R-values on the test set, emphasizing their ability to maintain strong linear correlations even with new and unseen data. Remarkably, Models M7 to M9 display extensive improvements in R-values on the test set compared to the training set, highlighting their adaptability and enhanced linear relationships in new scenarios. Regarding the R^2, the trend follows a similar pattern, with Models M5 to M9 achieving higher values in both the training and test datasets. Particularly, Model 5 stands out with an R^2 value of 0.7870

in the training set and 0.9274 in the test set, indicating its superior ability to explain the variability in the target variables. Therefore, the analysis of R and R^2 values underscores the varying degrees of linear relationships and explanatory power across the models. Models M5 to M9 exhibit notable strengths, particularly in maintaining strong linear correlations and explaining variability, with Model 5 consistently emerging as a standout performer on both familiar and novel datasets.

Table IV.2: Performance criteria of MLP during train and test phases.

		NSE	RMSE	MAE	R	R^2
M1	**Train**	0.0010	11.8770	5.1820	0.0350	0.0010
	Test	-0.0179	11.1420	6.0170	0.0764	0.0058
M2	**Train**	0.0040	11.8600	5.2330	0.0630	0.0040
	Test	-0.0087	11.0910	6.0450	0.1006	0.0101
M3	**Train**	0.0070	11.8400	5.2260	0.0880	0.0080
	Test	-0.0092	11.0940	6.0420	0.0899	0.0081
M4	**Train**	0.0120	11.8140	5.1450	0.1150	0.0130
	Test	-0.0144	11.1220	6.0080	0.0750	0.0056
M5	**Train**	0.7870	5.4840	1.5490	0.8870	0.7870
	Test	0.9221	3.0830	1.2860	0.6300	0.9274
M6	**Train**	0.8740	4.2140	1.3270	0.9350	0.8740
	Test	0.9171	3.1790	1.4340	0.9679	0.9368
M7	**Train**	**0.8750**	**4.2080**	**1.3390**	**0.9350**	**0.8750**
	Test	**0.9420**	**2.6590**	**1.1780**	**0.9715**	**0.9439**
M8	**Train**	0.8710	4.2630	1.3380	0.9340	0.8720
	Test	0.9352	2.8120	1.2560	0.9706	0.9421
M9	**Train**	0.8630	4.3920	1.2910	0.9300	0.8660
	Test	0.92675	2.989	1.269	0.9717	0.9442

In the MLP framework, Model M7 demonstrates an excellent performance in both the training and test datasets. In the training set, the model achieves an NSE of 0.8750, indicating its strong ability to capture the variability in the observed data. It also shows precision in prediction with an RMSE of 4.2080 and an MAE of 1.3390. The model's R stands at a high 0.9350, showing a strong linear relationship between predicted and actual values. Additionally, the R^2 is 0.8750, indicating that Model M7 effectively explains a significant portion of the variance in the target variable during training. The simplification abilities of Model M7 exhibit strong performance on unseen data, as demonstrated by its results on the test set. The model's NSE rises to an exceptional 0.9420, indicating enhanced predictive accuracy on new observations. Its RMSE and MAE decrease to 2.6590 and 1.1780, respectively, showing successful adaptation to the test set with minimal errors. The high values of R 0.9715

and R^2 0.9439 emphasize the model's ability to form strong linear relationships and explain a substantial proportion of the variability in the test data within the MLP framework.

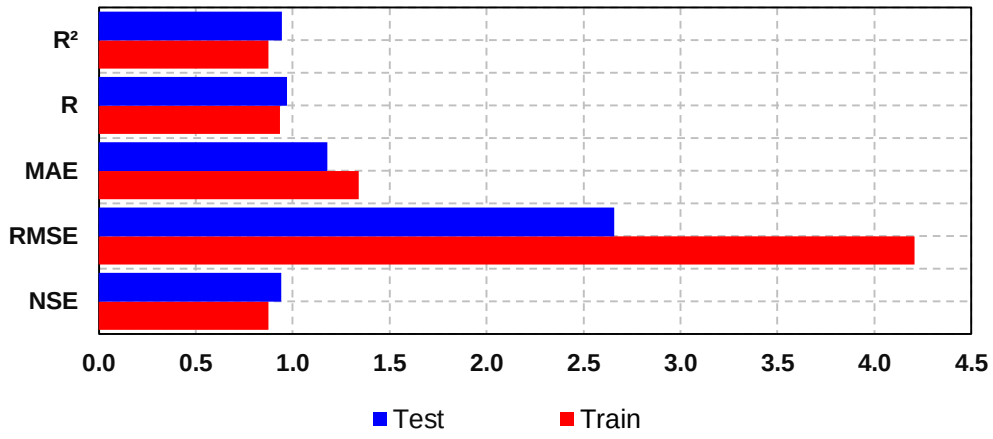

Figure IV.2: Bar graph representation the performance parameter for model 7.

In the end, Model M7 in the MLP framework stands out as the top-performing model based on the given metrics. Its outstanding predictive performance and strong generalization capabilities make it an excellent choice for applications needing precise and reliable predictions within the context of MLP.

IV.2.1.3.Long Short-Term Memory Neural Network -LSTM

The Investigation of the NSE values for LSTM models M1 to M9 in both the training and test datasets provides important insights into their predictive abilities. Models M5 to M9 consistently show higher NSE values in the training set, with Model 5 standing out with an impressive NSE of 0.7860, indicating its proficiency in capturing the variability within the training data. Conversely, Models M1 to M4 show relatively lower NSE values, suggesting potential areas for improvement in their predictive accuracy on the training set. Turning to the test set, Models M5 to M9 maintain their superior predictive efficiency, with Model 5 continuing to show outstanding performance with an NSE of 0.9208. Models M6 to M9 also show commendable NSE values on the test set, highlighting their ability to generalize effectively to new and unseen data. Remarkably, Models M7 to M9 showcase significant improvements in NSE on the test set compared to the training set, underscoring their adaptability and improved predictive abilities in new scenarios. The NSE analysis underlines the changing degrees of predictive efficiency among LSTM models, with Models M5 to M9 showcasing notable strengths, particularly on the test set. Model 5 consistently emerges as a

standout performer, suggesting its potential for accurate predictions on both familiar and new datasets in the context of LSTM architectures.

The examination of RMSE values for the LSTM models M1 to M9 in both the training and test datasets offers valuable insights into the accuracy of predictions. In the training set, RMSE values vary across models, with Models M5 to M9 consistently exhibiting lower errors, indicating their effectiveness in minimizing prediction discrepancies. Model 5, in particular, stands out with an RMSE of 5.4928, emphasizing its precision in predicting the target variable on the training data. Conversely, Models M1 to M4 show comparatively higher RMSE values, suggesting opportunities for improvement in their accuracy on the training set. Transitioning to the test set, Models M5 to M9 preserve their excellence in minimizing errors, with Model 5 continuing to demonstrate outstanding performance with an RMSE of 3.1080. Models M6 to M9 also highlight commendable RMSE values on the test set, highlighting their ability to generalize effectively to new and unseen data. Especially, Models M7 to M9 show substantial improvements in RMSE on the test set compared to the training set, indicating their adaptability and enhanced accuracy in new scenarios. In summary, the RMSE analysis underscores the varying degrees of accuracy in predictions, with Models M5 to M9 showcasing notable strengths, particularly on the test set. Model 5 consistently emerges as a standout performer, highlighting its potential for precise predictions with minimized errors on both familiar and new datasets in the context of LSTM architectures.

The investigation of MAE values for the LSTM models M1 to M9 in both the training and test datasets provides crucial insights into the accuracy of predictions. In the training set, MAE values show a range across models, with Models M5 to M9 consistently showcasing lower MAE, signifying their effectiveness in minimizing differences between predicted and actual values. Model 5, in particular, stands out with a remarkably low MAE of 1.4160, highlighting its accuracy in predicting the target variable on the training data. On the other hand, Models M1 to M4 show comparatively higher MAE values, suggesting opportunities for improvement in their accuracy on the training set. Shifting the focus to the test set, Models M5 to M9 continue their excellence in minimizing absolute errors, with Model 5 continuing to exhibit outstanding performance with an MAE of 1.1740. Models M6 to M9 also demonstrate commendable MAE values on the test set, underscoring their ability to generalize effectively to new and unseen data. Especially, Models M7 to M9 display significant improvements in MAE on the test set compared to the training set, indicating their adaptability and improved accuracy in new scenarios. The MAE analysis underlines the varying degrees of accuracy in

predictions, with Models M5 to M9 highlighting important strengths, particularly on the test set. Model 5 consistently emerges as a standout performer, highlighting its potential for precise predictions with minimized absolute errors on both familiar and novel datasets in the context of LSTM architectures

The examination of the R and the R^2 values for the LSTM models M1 to M9 in both the training and test datasets sheds light on the models' ability to establish a linear relationship and explain variability. In the training set, R-values show diversity across models, with Models M5 to M9 consistently showing higher correlations, signifying their efficiency in finding stronger linear relationships with the target variable. Model 5, in particular, stands out with an R-value of 0.8870, indicating a strong linear correlation in the training data. Equally, Models M1 to M4 show relatively lower R-values, suggesting a potential opportunity for improvement in capturing linear relationships on the training set. Turning attention to the test set, Models M5 to M9 conserve their excellence in linear relationships, with Model 5 continuing to show outstanding performance with an R-value of 0.9620. Models M6 to M9 also display commendable R-values on the test set, underlining their ability to maintain strong linear correlations even with new and unseen data. Especially, Models M7 to M9 showcase extensive improvements in R-values on the test set compared to the training set, highlighting their adaptability and improved linear relationships in new scenarios. About the R^2, the development follows a similar pattern, with Models M5 to M9, achieving higher values both in the training and test datasets. Especially, Model 5 stands out with an R^2 value of 0.7868 in the training set and 0.9255 in the test set, indicating its superior ability to explain the variability in the target variable. In summary, the analysis of R and R^2 values underscores the varying degrees of linear relationships and explanatory power across LSTM models. Models M5 to M9 show outstanding strength, particularly in maintaining strong linear correlations and explaining variability, with Model 5 consistently emerging as a standout performer on both familiar and new datasets.

Table IV.3: Performance criteria of LSTM during train and test phases.

		NSE	RMSE	MAE	R	R^2
M1	**Train**	-0.0010	11.8880	4.9140	0.0160	0.0003
	Test	-0.0311	11.2140	5.8380	0.0740	0.0055
M2	**Train**	0.0010	11.8803	5.2670	0.0230	0.0005
	Test	-0.0152	11.1260	6.0800	0.0560	0.0031
M3	**Train**	-0.0040	11.9069	4.6210	0.0340	0.0012
	Test	-0.0462	11.2950	5.6600	0.0680	0.0047

M4	**Train**	0.0010	11.8765	5.0310	0.0370	0.0014
	Test	-0.0230	11.1690	5.9200	0.0630	0.0040
M5	**Train**	0.7860	5.4928	1.4160	0.8870	0.7868
	Test	0.9208	3.1080	1.1740	0.9620	0.9255
M6	**Train**	0.7860	5.4928	1.4160	0.8870	0.7870
	Test	0.9198	3.1270	1.2670	0.9660	0.9322
M7	**Train**	**0.8750**	**4.2080**	**1.4100**	**0.9360**	**0.8752**
	Test	**0.9335**	**2.8470**	**1.3220**	**0.9680**	**0.9375**
M8	**Train**	0.8770	4.1655	1.3900	0.9370	0.8773
	Test	0.9252	3.0210	1.3530	0.9650	0.9317
M9	**Train**	0.8750	4.2012	1.3740	0.9360	0.8768
	Test	0.93	2.921	1.276	0.966	0.9335

The estimation of Model M7 within the LSTM framework shows its exemplary predictive ability on both the training and test datasets. In the training set, Model M7 reaches a commendable NSE of 0.8750, suggesting its strong capacity to capture the variability in the observed data. The RMSE of 4.2080 and MAE of 1.4100 underline the model's precision in minimizing prediction errors during training. The R impressively stands at 0.9360, indicating a strong linear relationship between predicted and actual values. Furthermore, the Coefficient of Determination R^2 reaches an excellent 0.8752, confirming that Model M7 explains a significant portion of the variance in the target variable during training within the LSTM architecture. The simplification abilities of Model M7 to unseen data are equally important, as verified by its performance on the test set. The NSE increases to an impressive 0.9335, signifying improved predictive efficacy on new observations. The RMSE decreases to 2.8470, and the MAE drops to 1.3220, indicating a successful adaptation of the model to the test set with minimal errors. The high values of R 0.9680 and R^2 0.9375 underscore the model's ability to find strong linear relationships and explain a significant proportion of the variability in the test data within the LSTM architecture.

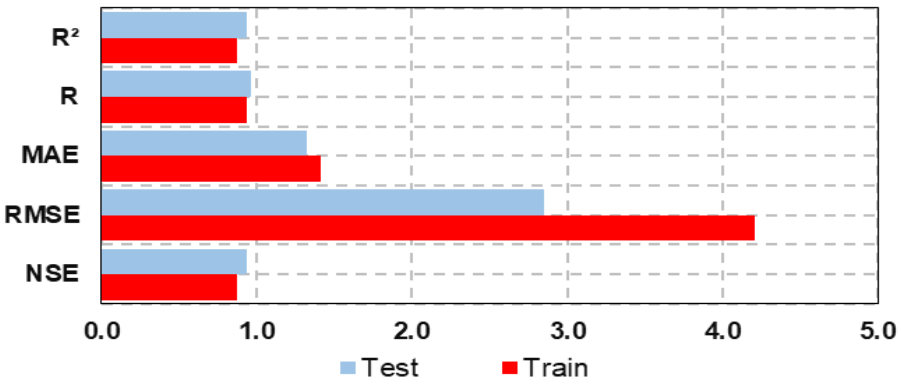

Figure IV.3: Bar graph representation the performance parameter for model 7.

In the end, Model M7, applied in the LSTM framework, stands out as the best-performing model based on the provided metrics. Its exceptional predictive performance, both in training and on unseen test data, positions it as a compelling choice for applications requiring accurate and reliable predictions within the context of Long Short-Term Memory networks.

IV.2.2.Results for the TRMM data

IV.2.2.1.Extreme Gradient Boosting-XGBoost

The investigation of NSE values for the XGBoost models M1 to M9 in both the training and test datasets provides a crucial understanding of their predictive capabilities.

In the training set, the NSE values vary across models, with Models M5 to M9 consistently showing higher NSE values. Model 5 stands out with an NSE of 0.9320, indicating its proficiency in capturing the observed variability in the training data. On the other hand, Models M1 to M4 show relatively lower NSE values, suggesting potential areas for improvement in their predictive accuracy on the training set. Shifting attention to the test set, Models M5 to M9 maintain their superior predictive efficiency, with Model 5 continuing to demonstrate outstanding performance with an NSE of 0.8635. Models M6 to M9 also display commendable NSE values on the test set, highlighting their ability to generalize effectively to new and unseen data. Remarkably, Models M7 to M9 showcase substantial improvements in NSE on the test set compared to the training set, highlighting their adaptability and enhanced predictive capabilities in novel scenarios. Overall the NSE analysis highlights the varying degrees of predictive efficiency among XGBoost models, with Models M5 to M9 showcasing notable strengths, particularly on the test set. Model 5 consistently emerges as a standout performer, suggesting its potential for accurate predictions on both familiar and new datasets in the XGBoost algorithms.

The Examination of RMSE values for the XGBoost models M1 to M9 in both the training and test datasets provides valuable insights into the accuracy of predictions. In the training set, RMSE values vary across models, with Models M5 to M9 consistently showing lower errors, showing their effectiveness in minimizing prediction discrepancies. Model 5, in particular, stands out with an RMSE of 3.0900, highlighting its precision in predicting the target variable on the training data. Equally, Models M1 to M4 display comparatively higher RMSE values, suggesting opportunities for improvement in their accuracy on the training set. Transitioning to the test set, Models M5 to M9 conserve their excellence in minimizing errors,

with Model 5 continuing to show outstanding performance with an RMSE of 4.080. Models M6 to M9 also highlight commendable RMSE values on the test set, highlighting their ability to generalize effectively to new and unseen data. Especially, Models M7 to M9 display an important improvement in RMSE on the test set compared to the training set, indicating their adaptability and improved accuracy in new scenarios. The RMSE analysis highlights the changing degrees of accuracy in predictions, with Models M5 to M9 displaying important strengths, particularly on the test set. Model 5 consistently emerges as a standout performer, highlighting its potential, for precise predictions with minimized errors on both familiar and new datasets in the XGBoost algorithms.

The examination of MAE values for the XGBoost models M1 to M9 in both the training and test datasets provides a crucial understanding of the accuracy of predictions. In the training set, MAE values display a variety across models, with Models M5 to M9 consistently showcasing lower absolute errors, indicating their effectiveness in minimizing differences between predicted and actual values. Model 5, in particular, stands out with a remarkably low MAE of 1.0150, emphasizing its precision in predicting the target variable on the training data. Conversely, Models M1 to M4 show comparatively higher MAE values, suggesting opportunities for improvement in their accuracy on the training set. Shifting the focus to the test set, Models M5 to M9 maintain their excellence in minimizing absolute errors, with Model 5 continuing to exhibit outstanding performance with an MAE of 1.6900. Models M6 to M9 also demonstrate commendable MAE values on the test set, underscoring their ability to generalize

Effectively to new and unseen data. Notably, Models M7 to M9 display substantial improvements in MAE on the test set compared to the training set, representing their adaptability and improved accuracy in new scenarios. The MAE analysis underlines the varying degrees of accuracy in predictions, with Models M5 to M9 displaying an extraordinary strength, particularly on the test set. Model 5 consistently emerges as a standout performer, highlighting its potential for precise predictions with minimized absolute errors on both familiar and novel datasets in the context of XGBoost algorithms.

The analysis of the R and the R^2 values for the XGBoost models M1 to M9 in both the training and test datasets provides a critical understanding of the models' ability to establish linear relationships and explain variability. In the training set, R-values show diversity across models, with Models M5 to M9 consistently displaying higher correlations, suggesting their effectiveness in establishing stronger linear relationships with the target variable. Model 5, in

particular, stands out with an R-value of 0.9660, indicating a strong linear correlation in the training data. Equally, Models M1 to M4 show relatively lower R-values, suggesting potential opportunities for improvement in capturing linear relationships on the training set. Turning attention to the test set, Models M5 to M9 conserve their excellence in linear relationships, with Model 5 continuing to demonstrate outstanding performance with an R-value of 0.9290. Models M6 to M9 also display commendable R-values on the test set, highlighting their ability to conserve strong linear correlations even with new and unseen data. Notably, Models M7 to M9 showcase significant improvements in R-values on the test set compared to the training set, highlighting their adaptability and improved linear relationships in new scenarios. Regarding the R^2, the trend follows a similar pattern, with Models M5 to M9 achieving higher values in both the training and test datasets. Remarkably, Model 5 stands out with an R^2 value of 0.9330 in the training set and 0.8637 in the test set, indicating its superior ability to explain the variability in the target variable. The analysis of R and R^2 values underlines the changing degrees of linear relationships and descriptive power across XGBoost models. Models M5 to M9 display extraordinary strengths, particularly in preserving strong linear correlations and explaining variability, with Model 5 consistently emerging as a standout performer on both familiar and new datasets. Here is the radar plot of the performance parameters.

Table IV.4: Performance criteria of XGBoost during train and test phases.

		NSE	RMSE	MAE	R	R^2
M1	**Train**	0.0270	11.7210	5.0630	0.2810	0.0790
	Test	-0.0120	11.1090	5.9580	0.1070	0.0114
M2	**Train**	0.0740	11.4350	4.8890	0.3060	0.0940
	Test	0.0223	10.9190	5.8190	0.2010	0.0404
M3	**Train**	0.1630	10.8710	4.5980	0.4360	0.1900
	Test	0.0370	10.837	5.7260	0.2510	0.0630
M4	**Train**	0.1780	10.7730	4.6200	0.5070	0.2570
	Test	0.0501	10.763	5.7540	0.2580	0.0666
M5	**Train**	0.9320	3.0900	1.0150	0.9660	0.9330
	Test	0.8635	4.080	1.6900	0.9290	0.8637
M6	**Train**	0.9490	2.6910	0.9220	0.9740	0.9490
	Test	0.8885	3.688	1.5480	0.9460	0.8940
M7	**Train**	0.9520	2.5980	0.8850	0.9760	0.9530
	Test	0.8964	3.554	1.4830	0.9500	0.9018
M8	**Train**	0.9520	2.5970	0.8970	0.9760	0.9530
	Test	0.8980	3.527	1.4810	0.9510	0.9053
M9	**Train**	**0.9570**	**2.4510**	**0.8590**	**0.9790**	**0.9580**
	Test	**0.8981**	**3.525**	**1.4680**	**0.9500**	**0.9030**

In the XGBoost framework, Model M9 demonstrates exceptional predictive performance on both the training and test datasets. In the training set, it achieves an NSE of 0.9570, highlighting its strong ability to capture the variability in the observed data. The model's RMSE of 2.4510 and MAE of 0.8590 underline its precision in minimizing prediction errors during training. Its R is remarkably high at 0.9790, indicating a strong linear relationship between predicted and actual values. Additionally, the R^2 reaches a commendable 0.9580, confirming that Model M9 explains an important portion of the variance in the target variable during training within the XGBoost framework. The simplification abilities of Model M9 to unseen data are equally compelling, as shown by its performance on the test set. The NSE remains high at 0.8981, signifying a higher predictive efficiency on new observations. The RMSE decreases to 3.525, and the MAE drops to 1.4680, indicating a successful adaptation of the model to the test set with minimal errors. The high values of R 0.9500and R^2 0.9030 underline the model's ability to found a strong linear relationships and explain an important proportion of the variability in the test data within the XGBoost architecture.

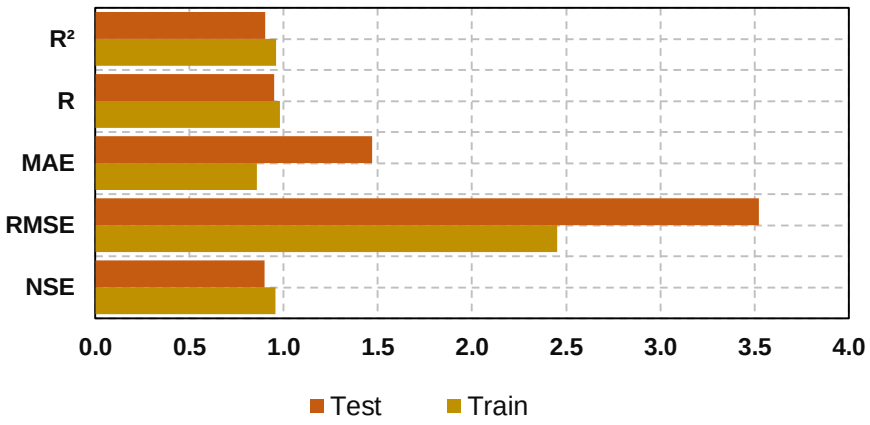

Figure IV.4: Bar graph showing the performance parameter for model 9

In the end, Model M9, applied in the XGBoost framework, emerges as the best-performing model based on the provided metrics. Its excellent predictive performance, both in training and on unseen test data, positions it as a compelling choice for applications requiring accurate and reliable predictions within the XGBoost algorithms

IV.2.2.2.Multi-layer Perceptron Network-MLP

The Examination of NSE values for the MLP models from M1 to M9 in both the training and test datasets offers an understanding of the models' predictive capabilities. In the training set, NSE values vary from 0.0150 to 0.1420, with Models M5 to M9 consistently signifying

higher efficiency. Model 5, in particular, stands out with an NSE of 0.8280, demonstrating its ability to capture observed variability in the training data. Similarly, Models M1 to M4 display comparatively lower NSE values, signifying opportunities for improvement in their predictive performance on the training set. Transitioning to the test set, Models M5 to M9 preserve their superior predictive efficiency, with Model 5 continuing to display outstanding performance with an NSE of 0.9361. Models M6 to M9 also highlight estimable NSE values on the test set, highlighting their ability to simplify successfully to new and unseen data. Remarkably, Models M7 to M9 show advancements in NSE on the test set compared to the training set, indicating their adaptability and improved predictive abilities in new scenarios. The NSE analysis highlights the varying degrees of predictive efficiency among MLP models, with Models M5 to M9 highlighting important strengths, particularly on the test set. Model 5 consistently emerges as a standout performer, suggesting its potential for accurate predictions on both familiar and new datasets in the context of MLP algorithms.

The Investigation of RMSE values for the MLP models M1 to M9 in both the training and test datasets provides an important understanding of the accuracy of predictions. In the training set, RMSE values range from 3.6610 to 4.9300, with Models M5 to M9 consistently showing lower errors, showing their effectiveness in minimizing prediction differences. Model 5 stands out with a remarkably low RMSE of 4.9300, highlighting its accuracy in predicting the target variable on the training data. Equally, Models M1 to M4 display comparatively higher RMSE values, suggesting areas for improvement in their accuracy on the training set. Shifting the focus to the test set, Models M5 to M9 keep their excellence in minimizing errors, with Model 5 continuing to prove outstanding performance with an RMSE of 2.792. Models M6 to M9 also highlight estimable RMSE values on the test set, highlighting their ability to generalize effectively to new and unseen data. Especially, Models M7 to M9 display improvements in RMSE on the test set compared to the training set, indicating their adaptability and enhanced accuracy in novel scenarios. In summary, the RMSE analysis underscores the varying degrees of accuracy in predictions, with Models M5 to M9 showcasing notable strengths, particularly on the test set. Model 5 consistently emerges as a standout performer, suggesting its potential for precise predictions with minimized errors on both familiar and novel datasets in the context of MLP algorithms.

The analysis of MAE values for the MLP models from M1 to M9 in both the training and test datasets provides an important understanding of the accuracy of predictions. In the training set, MAE values range from 1.1280 to 1.4230, with Models M5 to M9 consistently

showing lower absolute errors. Model 5 particularly stands out with a remarkably low MAE of 1.4230, highlighting its precision in predicting the target variable on the training data. Equally, Models M1 to M4 display relatively higher MAE values, indicating areas for improvement in their accuracy on the training set. Transitioning to the test set, Models M5 to M9 keep their excellence in minimizing absolute errors, with Model 5 continuing to display outstanding performance with an MAE of 1.2440. Models M6 to M9 also highlight commendable MAE values on the test set, highlighting their ability to generalize effectively to new and unseen data. Remarkably, Models M7 to M9 display improvements in MAE on the test set compared to the training set, indicating their adaptability and improved accuracy in new scenarios. The MAE analysis highlights the changing degrees of accuracy in predictions, with Models M5 to M9 highlighting important strengths, particularly on the test set. Model 5 consistently emerges as a standout performer, highlighting its potential for precise predictions with minimized absolute errors on both familiar and new datasets in the MLP algorithms.

The analysis of R and the R^2 values for the MLP models from M1 to M9 in both the training and test datasets sheds light on the models' ability to find linear relationships and explain variability. In the training set, R-values vary between 0.9380 and 0.9560, with Models M7 to M9 consistently showing higher correlations, signifying their efficiency in establishing strong linear relationships with the target variable. Model 9, in particular, stands out with an R-value of 0.9560, indicating a strong linear correlation in the training data. Conversely, Models M1 to M4 display relatively lower R-values, suggesting potential opportunities for improvement in capturing linear relationships on the training set. Turning attention to the test set, Models M5 to M9 keep their excellence in linear relationships, with Model 5 continuing to show outstanding performance with an R-value of 0.9683. Models M6 to M9 also show estimable R-values on the test set, highlighting their ability to keep strong linear correlations even with new and unseen data. Particularly, Models M7 to M9 showcase improvements in R-values on the test set compared to the training set, indicating their adaptability and improved linear relationships in new scenarios. Regarding the R^2, the trend follows a similar pattern, with Models M5 to M9 achieving higher values in both the training and test datasets. Particularly, Model 5 stands out with an R^2 value of 0.9376 in the test set, indicating its superior ability to explain the variability in the target variable. The analysis of R and R^2 values underlines the varying degrees of linear relationships and explanatory power across MLP models. Models M5 to M9 show important strengths, particularly in

keeping strong linear correlations and explaining variability, with Model 5 consistently emerging as a standout performer on both familiar and new datasets.

Table IV.5: Performance criteria of MLP during train and test phases.

		NSE	RMSE	MAE	R	R^2
M1	**Train**	0.0150	11.7930	5.0030	0.1240	0.0150
	Test	-0.0038	11.0640	5.8760	0.1365	0.0186
M2	**Train**	0.0600	11.5230	4.8300	0.2460	0.0600
	Test	0.0329	10.860	5.7220	0.2310	0.0534
M3	**Train**	0.1030	11.2580	4.5580	0.3200	0.1030
	Test	0.0528	10.7480	5.6030	0.2864	0.0820
M4	**Train**	0.1420	11.0100	4.4040	0.3770	0.1420
	Test	0.0910	10.5280	5.4690	0.3428	0.1175
M5	**Train**	0.8280	4.9300	1.4230	0.9100	0.8280
	Test	0.9361	2.7920	1.2440	0.9683	0.9376
M6	**Train**	0.8790	4.1340	1.2670	0.9380	0.8810
	Test	0.9388	2.7320	1.1960	0.9710	0.9428
M7	**Train**	0.9140	3.4930	1.1280	0.9560	0.9140
	Test	0.9415	2.6710	1.1850	0.9712	0.9432
M8	**Train**	**0.9050**	**3.6610**	**1.2380**	**0.9530**	**0.9090**
	Test	**0.9494**	**2.4850**	**1.1580**	**0.9748**	**0.9503**
M9	**Train**	0.8770	4.1660	1.2990	0.9380	0.8810
	Test	0.9235	3.0550	1.3720	0.9697	0.9404

Model M8 in the MLP framework shows excellent predictive capabilities in both the training and test datasets. In the training set, it achieves an NSE of 0.9050, highlighting its strong ability to capture the variability in the observed data. The model's RMSE of 3.6610 and MAE of 1.2380 underline the model's precision in minimizing prediction errors during training. The R stands impressively high at 0.9530, demonstrating a strong linear relationship between predicted and actual values. Furthermore, the R^2 reaches an estimable 0.9090, affirming that Model M8 explains an important portion of the variance in the target variable during training within the MLP architecture. The simplification abilities of Model M8 to unseen data are equally compelling, as demonstrated by its performance on the test set. The NSE remains high at 0.9494, indicating improved predictive efficiency on new observations. The RMSE decreases to 2.485, and the MAE drops to 1.1580, indicating a successful adaptation of the model to the test set with minimal errors. The very high values of R 0.9748 and R^2 0.9503

highlight the model's ability to establish strong linear relationships and explain an important proportion of the variability in the test data within the MLP architecture.

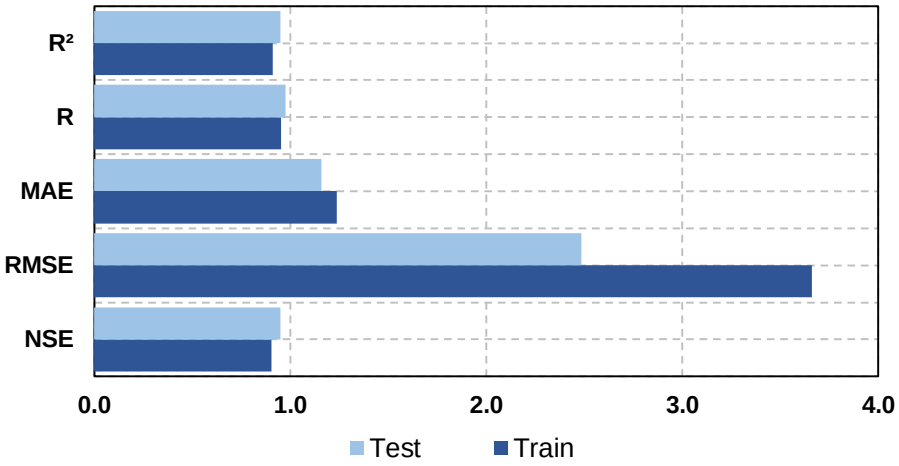

Figure IV.5: Bar graph showing the performance parameter for model 8.

In conclusion, Model M8, implemented in the MLP framework, emerges as the best-performing model based on the provided metrics. Its excellent predictive performance, both in training and on unseen test data, positions it as a compelling choice for applications requiring accurate and reliable predictions within the context of Multilayer Perceptron networks.

IV.2.2.3.Long Short-Term Memory Neural Network-LSTM

The Examination of the NSE values for the LSTM models from M1 to M9 in both the training and test datasets provides valuable understanding of the models' predictive performance. In the training set, NSE values range from 0.0110 to 0.8950, highlighting the varying degrees of efficacy in capturing observed variability in the target variable. Models M5 to M9 consistently display higher NSE values, with Model 9 standing out with an impressive NSE of 0.8950, indicating its proficiency in predicting the target variable on the training data. Equally, Models M1 to M4 display relatively lower NSE values, suggesting opportunities for improvement in their predictive capabilities on the training set. Transitioning to the test set, Models M5 to M9 keep their superior predictive efficiency, with Model 5 continuing to show outstanding performance with an NSE of 0.9348. Models M6 to M9 also highlight commendable NSE values on the test set, highlighting their ability to generalize effectively to new and unseen data. Remarkably, Models M7 to M9 show improvements in NSE on the test set compared to the training set, indicating their adaptability and enhanced predictive capabilities in new scenarios. The NSE analysis highlights the changing degrees of predictive

efficiency between LSTM models, with Models M5 to M9 highlighting important strengths, particularly on the test set. Model 5 consistently emerges as a standout performer, suggesting its potential for accurate predictions on both familiar and new datasets in the LSTM algorithms.

The Examination of RMSE values for the LSTM models from M1 to M9 in both the training and test datasets offers crucial understanding of the accuracy of the model's predictions. In the training set, RMSE values range from 3.8560 to 11.8200, displaying varying levels of accuracy in capturing the discrepancies between predicted and observed values. Models M5 to M9 consistently show lower RMSE values, with Model 9 displaying the lowest at 3.8560, indicating its precision in predicting the target variable on the training data. Equally, Models M1 to M4 demonstrate relatively higher RMSE values, suggesting potential areas for improvement in accuracy on the training set. Shifting to the test set, Models M5 to M9 keep their excellence in minimizing errors, with Model 5 continuing to highlight outstanding performance with an RMSE of 2.8210. Models M6 to M9 also display commendable RMSE values on the test set, highlighting their ability to generalize effectively to new and unseen data. Particularly, Models M7 to M9 show improvements in RMSE on the test set compared to the training set, indicating their adaptability and improved accuracy in new scenarios. In summary, the RMSE analysis highlights the changing degrees of accuracy in predictions among LSTM models, with Models M5 to M9 highlighting important strengths, particularly on the test set. Model 5 consistently emerges as a standout performer, emphasizing its potential for precise predictions with minimized errors on both familiar and new datasets in the LSTM algorithms.

The analysis of MAE values for the LSTM models M1 to M9 in both the training and test datasets provides understanding of the accuracy and precision of the model's predictions. In the training set, MAE values vary from 1.2650 to 5.0030, indicating the absolute average errors between predicted and observed values. Models M5 to M9 consistently show lower MAE values, with Model 9 displaying the lowest at 1.2650, suggesting superior precision in predicting the target variable on the training data. Equally, Models M1 to M4 show relatively higher MAE values, implying areas for improvement in accuracy on the training set. Transitioning to the test set, Models M5 to M9 keep their excellence in minimizing absolute errors, with Model 5 continuing to highlight outstanding performance with a MAE of 1.3640. Models M6 to M9 also display commendable MAE values on the test set, highlighting their ability to generalize effectively to new and unseen data. Remarkably, Models M7 to M9 show

improvements in MAE on the test set compared to the training set, indicating their adaptability and improved accuracy in new scenarios. The MAE analysis highlights the changing degrees of accuracy and precision in predictions among LSTM models, with Models M5 to M9 showcasing outstanding strengths, particularly on the test set. Model 5 consistently emerges as a standout performer, highlighting its potential for accurate and precise predictions with minimized absolute errors on both familiar and novel datasets in the context of LSTM algorithms.

The analysis of R and the R^2 values for the LSTM models from M1 to M9 in both the training and test datasets provides insights into the models' ability to find linear relationships and explain variability. In the training set, R values range between 0.9420 and 0.9470, with Models M8 and M9 exhibiting strong linear correlations, indicating their effectiveness in establishing strong relationships with the target variable. Model 5 also displays a commendable R-value of 0.9110, suggesting a significant linear relationship. Models M1 to M4 display slightly lower R-values, indicating room for improvement in capturing linear relationships on the training set. Turning to the test set, Models M5 to M9 maintain their excellence in linear relationships, with Model 5 continuing to demonstrate outstanding performance with an R-value of 0.9690. Models M6 to M9 also display commendable R-values on the test set, highlighting their ability to preserve strong linear correlations even with new and unseen data. Models M7 to M9 show improvements in R-values on the test set compared to the training set, indicating their adaptability and improved linear relationships in new scenarios. About the R^2, the trend follows a similar pattern, with Models M5 to M9 achieving higher values in both the training and test datasets. Remarkably, Model 5 stands out with an R^2 value of 0.9380 in the test set, indicating its superior ability to explain the variability in the target variable. The analysis of R and R^2 values underlines the changing degrees of linear relationships and clarifying power across LSTM models. Models M5 to M9 show important strengths, particularly in keeping strong linear correlations and explaining variability, with Model 5 consistently emerging as a standout performer on both familiar and new datasets.

Table IV.6: Performance criteria of LSTM during train and test phases.

		NSE	RMSE	MAE	R	R^2
M1	**Train**	0.0110	11.8200	4.7070	0.1130	0.0130
	Test	-0.0238	11.1740	5.6830	0.1180	0.0139
M2	**Train**	0.0530	11.5670	5.2460	0.2330	0.0540
	Test	0.0322	10.8640	6.0200	0.2100	0.0440
M3	**Train**	0.1050	11.2440	4.5270	0.3240	0.1050

	Test	0.0258	10.8990	5.5990	0.2550	0.0650
M4	**Train**	0.1470	10.9740	4.8130	0.3850	0.1480
	Test	0.0713	10.6420	5.7640	0.3060	0..939
M5	**Train**	**0.8300**	**4.9040**	**1.5450**	**0.9110**	**0.8300**
	Test	**0.9348**	**2.8210**	**1.3640**	**0.9690**	**0.9380**
M6	**Train**	0.8880	3.9840	1.2650	0.9420	0.8880
	Test	0.9304	2.9140	1.2730	0.9690	0.9384
M7	**Train**	0.8900	3.9350	1.5840	0.9450	0.8930
	Test	0.9326	2.8670	1.5270	0.9680	0.9372
M8	**Train**	0.8890	3.9590	1.7590	0.9450	0.8930
	Test	0.9306	2.9100	1.6950	0.9690	0.9382
M9	**Train**	0.8950	3.8560	1.5110	0.9470	0.8970
	Test	0.9266	2.9910	1.5210	0.9650	0.9313

In the LSTM framework, Model M5 shows notable predictive capabilities on both the training and test datasets, making it the optimal model based on the provided metrics. In the training set, Model M5 achieves an important NSE of 0.8300, representing its strong ability to capture the variability in the observed data. The RMSE of 4.9040 and MAE of 1.5450 highlight the model's precision in minimizing prediction errors during training. The R stands at a commendable 0.9110, representing a strong linear relationship between predicted and actual values. Furthermore, the R^2 reaches 0.8300, confirming that Model M5 explains a considerable portion of the variance in the target variable during training within the LSTM architecture. The simplification abilities of Model M5 to unseen data are highly impressive, as confirmed by its performance on the test set. The NSE increases significantly to 0.9348, suggesting improved predictive efficiency on new observations. The RMSE decreases to 2.8210, and the MAE drops to 1.3640, indicating a successful adaptation of the model to the test set with minimal errors. The very high values of R 0.9690 and R (0.9380) underscore the model's ability to establish robust linear relationships and explain a significant proportion of the variability in the test data within the LSTM architecture.

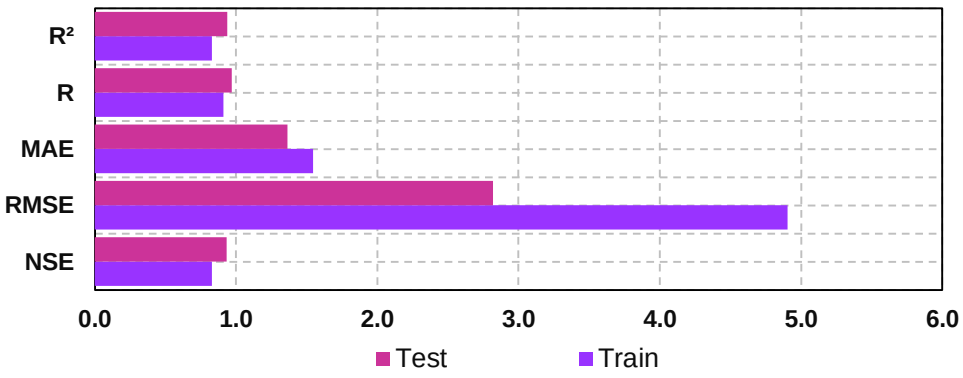

Figure IV.6: Bar graph showing the performance parameter for model 5.

Based on the given metrics, Model M5, implemented in the LSTM framework, stands out as the best-performing model based on the provided metrics. Its exceptional predictive performance, both in training and on unseen test data, positions it as a compelling choice for applications requiring accurate and reliable predictions within the context of Long Short-Term Memory networks.

IV.3.Summary of the results

IV.3.1.In situ-data results

In the XGBoost, the performance metrics for Model 5 on both the training and test datasets display its extraordinary predictive capabilities. Similarly, in the MLP framework, Model M7 demonstrates excellent performance on both the training and test datasets. Additionally, the estimation of Model M7 within the LSTM framework shows its exemplary predictive ability on both the training and test datasets. The figure below illustrates the performance criteria for the test phase of all the models.

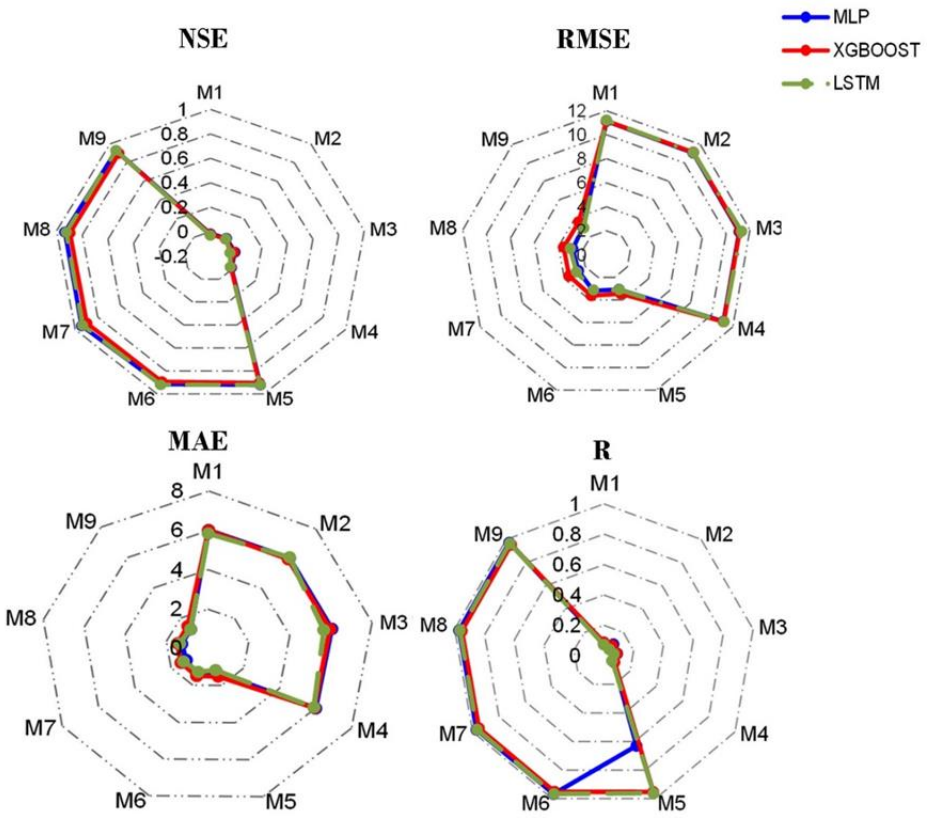

Figure IV.7: Radar plot representation of performance parameters during the test phase for each algorithm using in situ data.

As we can see in the violent plot, the M7 stands out as the most accurate in the LSTM algorithm, as shown in Figure IV.8. Similarly, the M5 model is the most accurate in the

XGBoost algorithm, while the M7 model is the most accurate in The MLP algorithm. These models are closer to the observed data compared to other computing models.

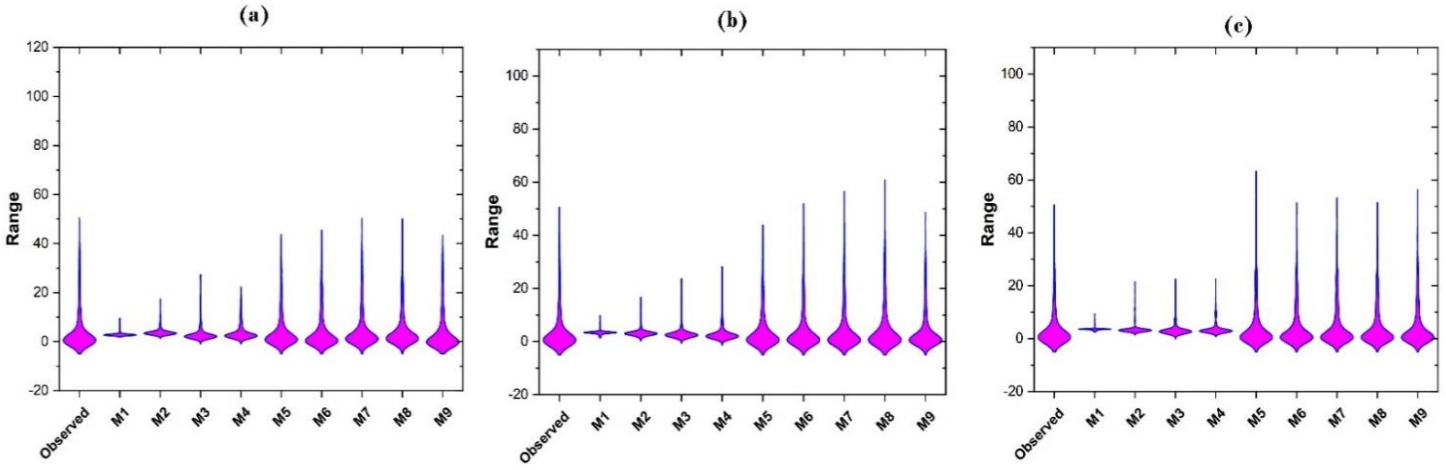

Figure IV.8: Violin plot representation of models using in situ data for each algorithm:

(a) LSTM, (b) MLP, (c) XGBoost in the test phase.

According to the results, among all 9 models within each algorithm, such as LSTM, the M7 model stands out as the most accurate, as illustrated in Figure IV.9 similarly, in the XGBoost algorithm, the M5 model is the most accurate, and in the MLP algorithm, M7 is the most accurate. These models are closer to the reference point (observed daily runoff) compared to other soft computing models.

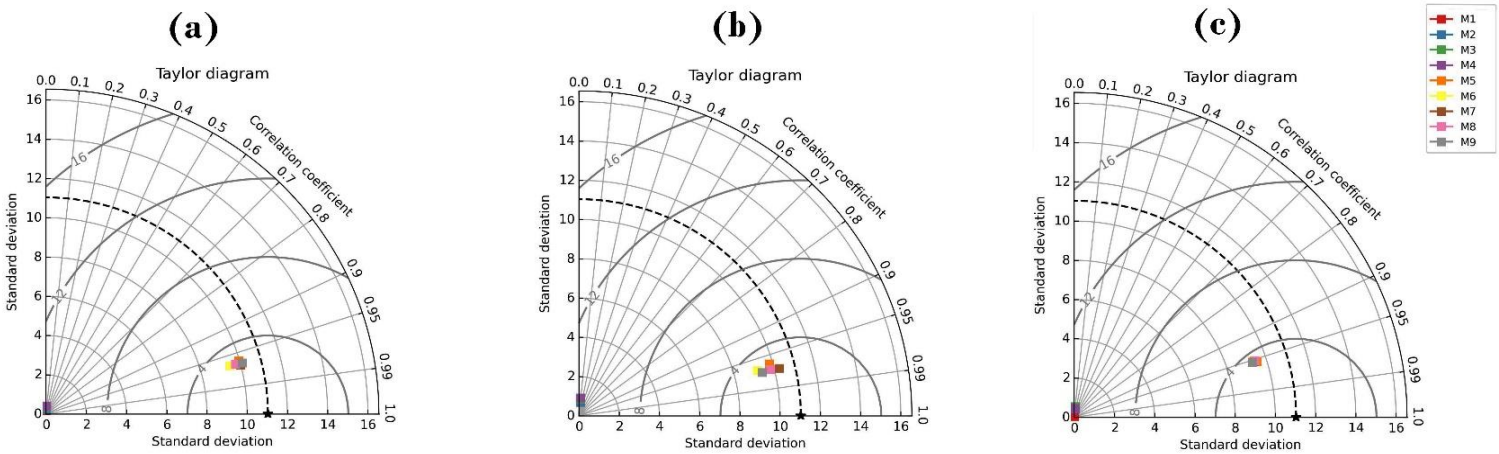

Figure IV.9: Taylor diagram representation of models using in situ data in each algorithm:

(a) LSTM, (b) MLP, (c) XGBoost in the test phase.

IV.3.2.TRMM data results

In the XGBoost, the performance metrics for Model 9 on both the training and test datasets display its extraordinary predictive capabilities. Similarly, in the MLP framework, Model M78 demonstrates excellent performance on both the training and test datasets. Additionally, the estimation of Model M5 within the LSTM framework shows its exemplary predictive ability on both the training and test datasets. The figure below illustrates the performance criteria for the test phase of all the models.

.

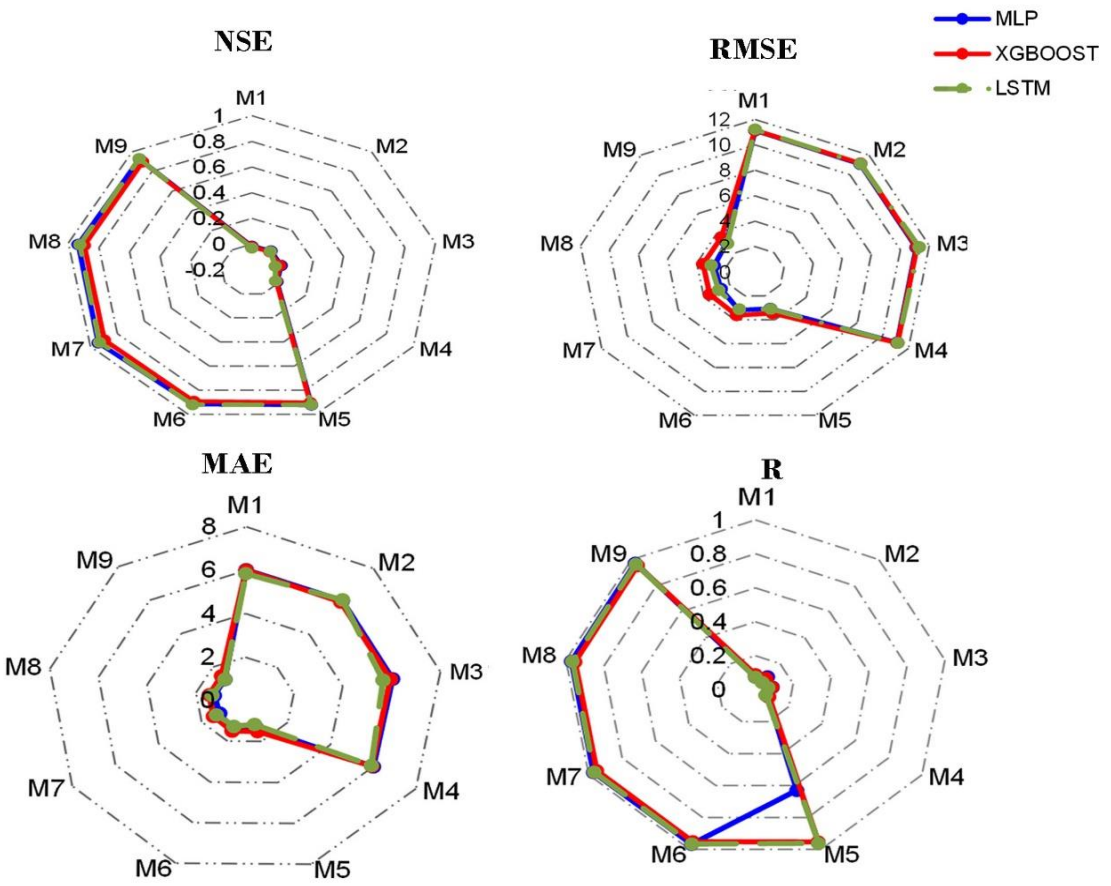

Figure IV.10: Radar plot representation of performance parameters during the test phase for each algorithm using TRMM data.

The M7 model stands out as the most accurate in the LSTM algorithm, as shown in Figure IV.11. Similarly, the M5 model is the most accurate in the XGBoost algorithm, while the M7 model is the most accurate in the MLP algorithm. These models are closer to the observed data compared to other computing models.

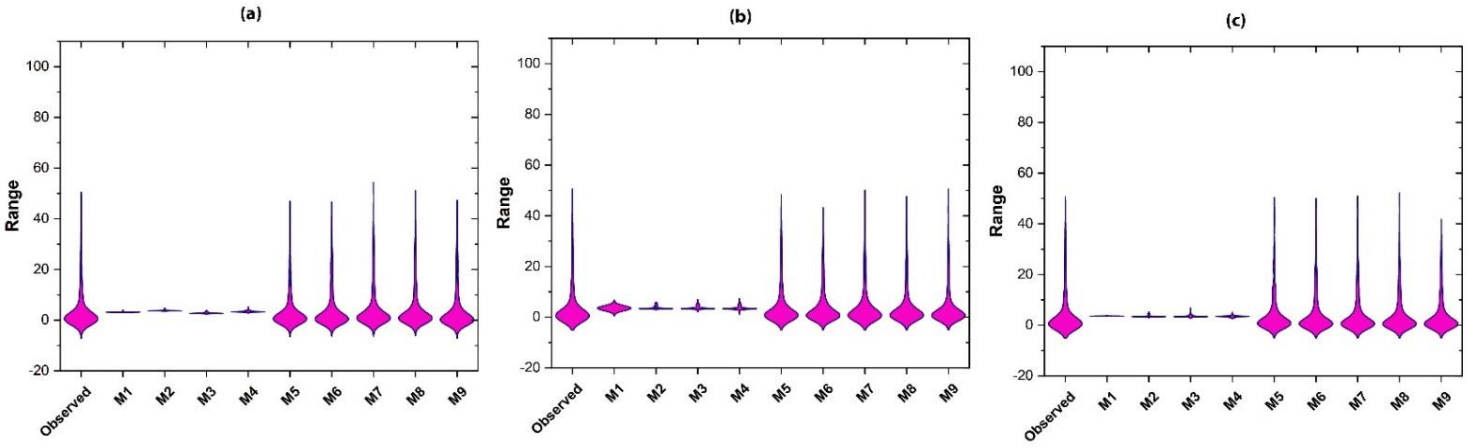

Figure IV.11: violin plot representation of models using in TRMM data in each algorithm:

(a) LSTM, (b) MLP, (c) XGBoost in the test phase.

On the other hand, in TRMM data analysis, the outcomes reveal that among all nine models within each algorithm, Model M5 in the LSTM algorithm stands out as the most accurate, as illustrated in Figure IV.12. Similarly, in the XGBoost algorithm, Model M9 is the most accurate, and in the MLP algorithm, Model M8 holds that distinction. These models are closer to the reference point (observed data) compared to other soft computing models.

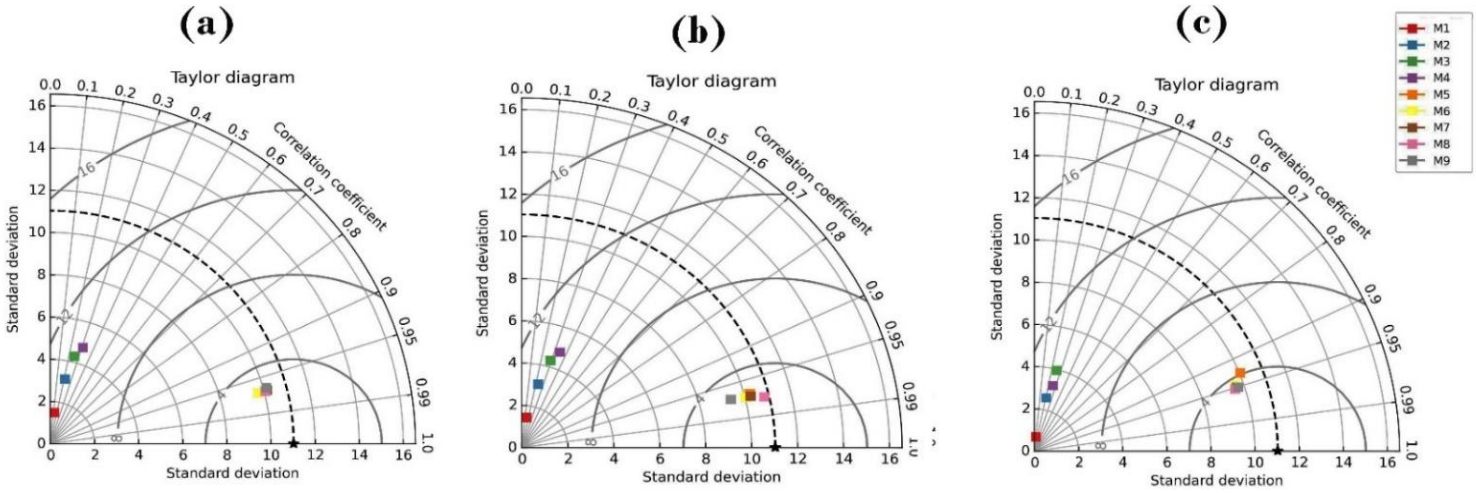

Figure IV.12: Taylor diagram representation of models using TRMM data in each algorithm:

(a) LSTM, (b) MLP, (c) XGBoost in the test phase.

The simulation results shown in Figure IV.13 were obtained during the in-situ data test phase, the time series graphs compare observed runoff with simulated daily runoff over time. The closer the red line (simulated daily runoff) tracks the blue line (observed daily runoff), the higher the accuracy for each algorithm. The data sets also include scatter plots that assess model accuracy by plotting observed values against simulated ones. Points closer to the diagonal line indicate a better match between observed and simulated data. The coefficient of

determination, or R^2 value, quantifies how well the model fits the data. For example, the MLP model achieves a high accuracy with an R^2 of 0.9439, Compared to the XGBoost model has an R^2 of 0.9106, and the LSTM model has an R^2 of 0.9375.

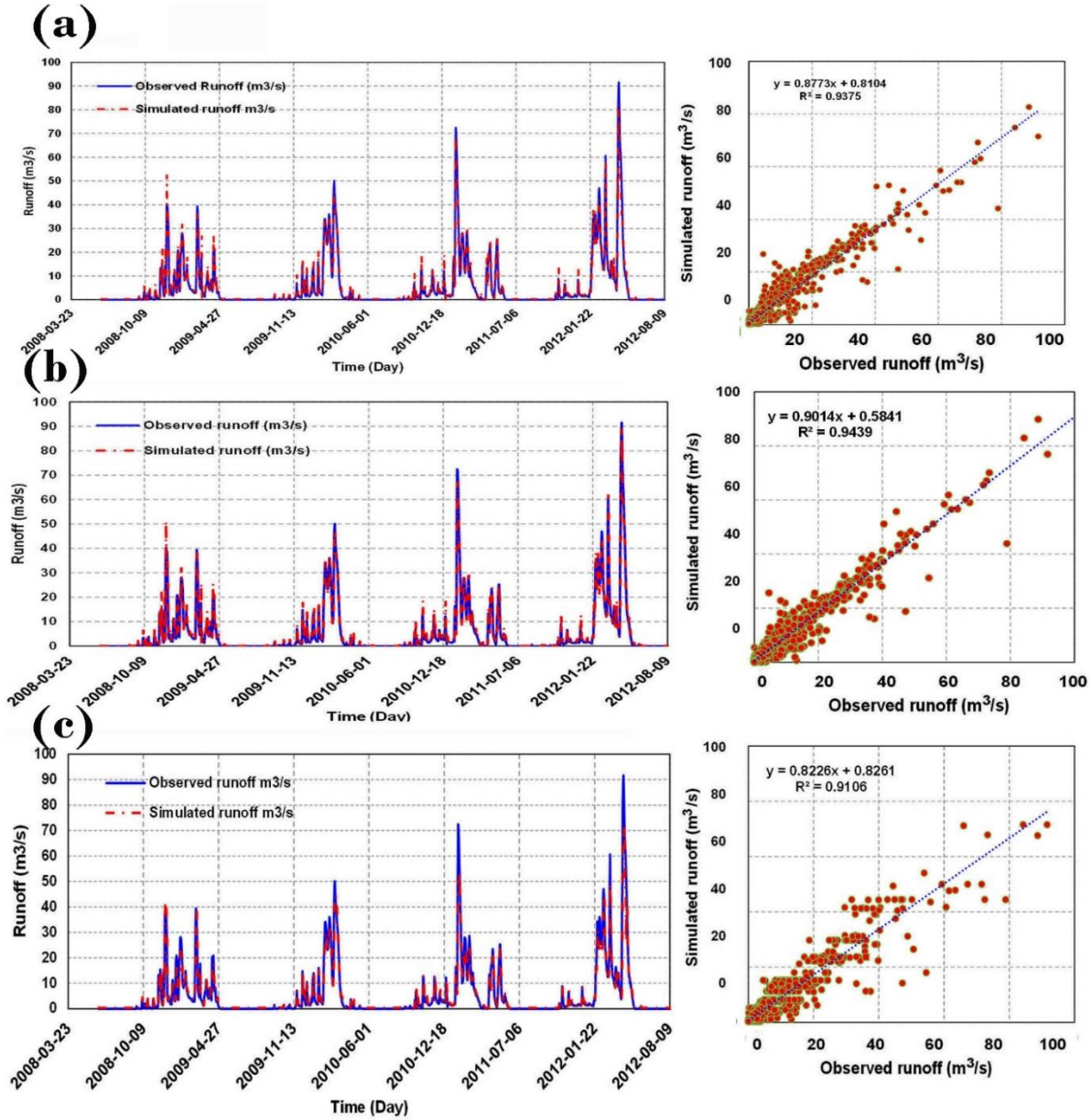

Figure IV.13: Observed and simulated daily runoff using: (a) LSTM, (b) MLP, and (c) XGBoost models with in-situ data during the test phase.

The figure below highlights how each algorithm's top-performing model fares in terms of specific performance parameters, By focusing on the test phase, The MLP M7 achieved an R of approximately 0.9715, an MAE of around 1.178, an RMSE of about 2.659, and an NSE of approximately 0.942. The LSTM M7 demonstrated better performance with an R-value of around 0.968, an MAE of approximately 1.322, an RMSE of about 2.847, and an NSE of approximately 0.9335. In contrast, the XGBoost M9 had an R-value of around 0.954, an MAE

of about 1.505, an RMSE of approximately 3.454, and an NSE of about 0.9022. Among the three, the LSTM model exhibited the best overall performance, as indicated by its higher correlation coefficient and NSE, suggesting it provides more accurate predictions compared to the MLP and XGBoost models.

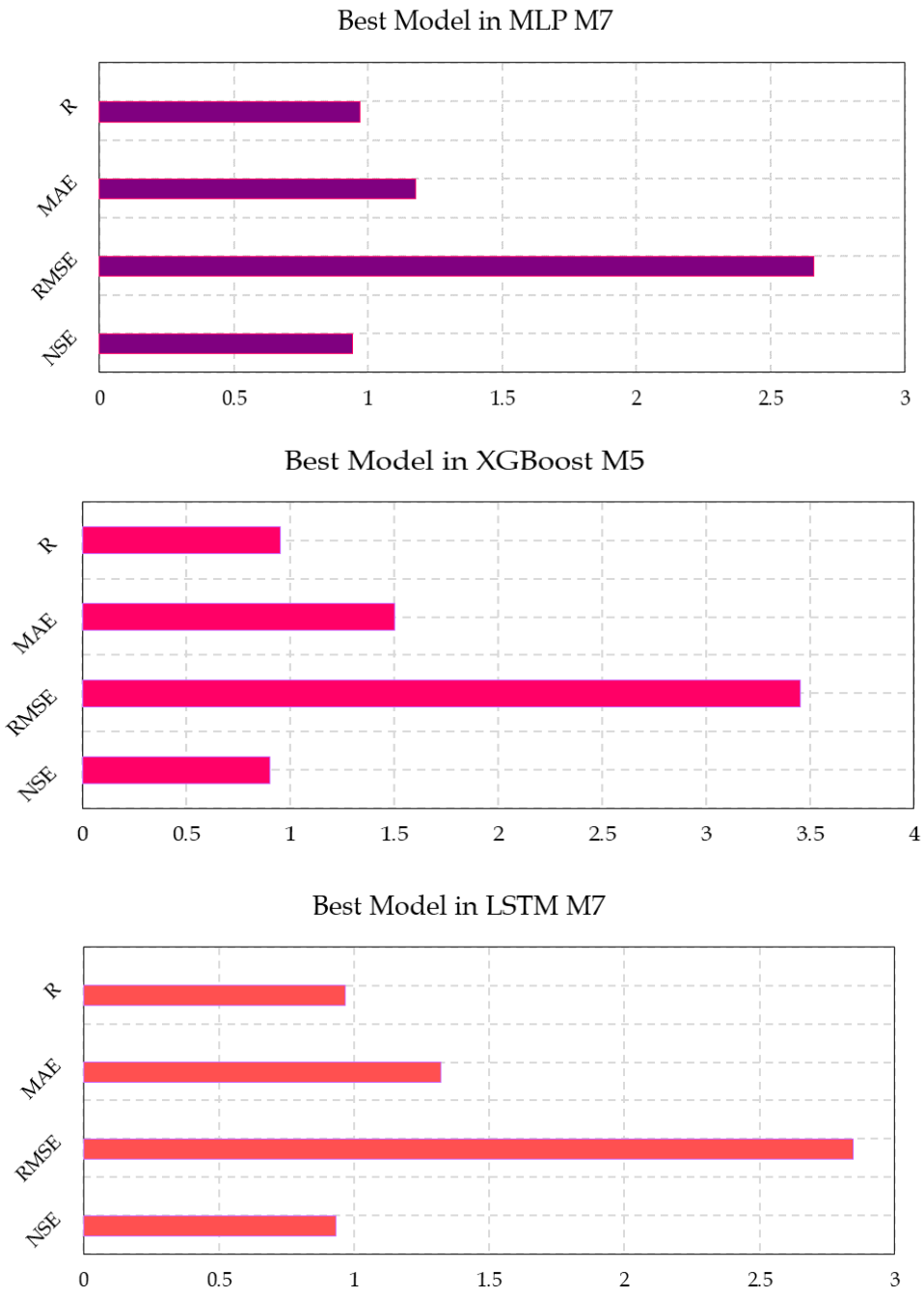

Figure IV.14: Bar graph showing the performance parameter for best models in each algorithm for the test phase in situ data.

The simulation results in Figure IV.15 are from the TRMM data test phase, where various algorithms were used to model runoff. The time series graphs compare observed runoff with simulated daily runoff over time. A closer match between the red line (simulated daily runoff) and the blue line (observed daily runoff) indicates a higher accuracy for each algorithm. The same sets also contain scatter plots that evaluate model accuracy by plotting observed values against simulated ones. Points closer to the diagonal line signify a better correlation between the two data sets. Furthermore, the R^2 value, or coefficient of determination, quantifies how well the model fits the data. For instance, the MLP model achieves high accuracy with an R^2 of 0.9503, compared with the XGBoost Model has an R^2 of 0.9030, and the LSTM model has achieved an R^2 of 0.9380.

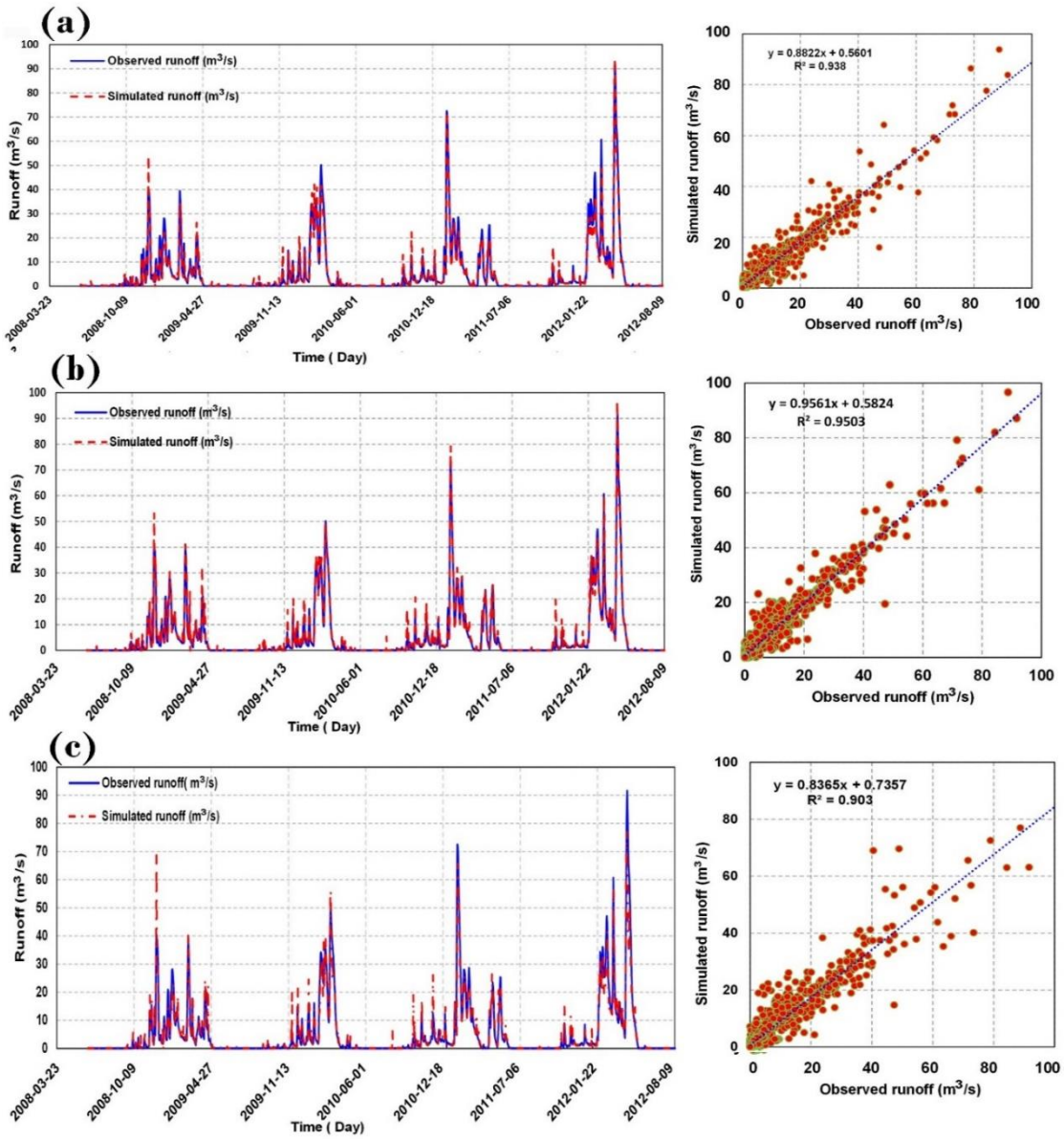

Figure IV.15: Observed and simulated daily runoff using: (a) LSTM, (b) MLP, and (c) XGBoost models with TRMM data during the test phase.

The figure below it's a bar graphs that illustrate the performance metrics for the best models of three algorithms—MLP, LSTM, and XGBoost—during the test phase using TRMM data.

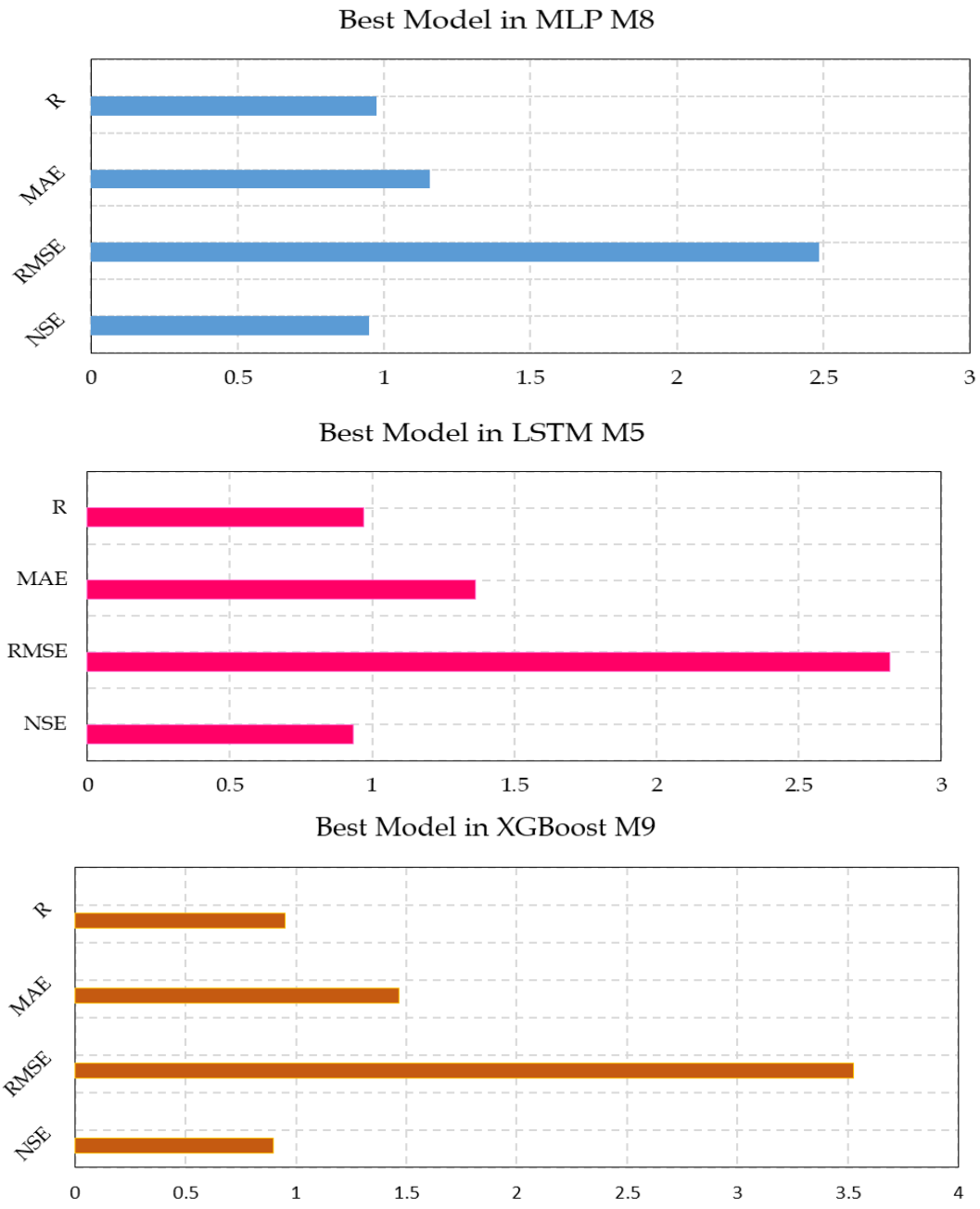

Figure IV.16: Bar graph showing the performance parameter for best models in each algorithm for the test phase in TRMM data.

IV.3.3.The Best Models in both datasets

The results of the anlysis illusrtate that the MLP shows notbale performance in both datasets, with Model M7 excelling for the in situ data and Model M8 for TRMM data. These

findings are summerized in the table below, which presents a comparative analysis of the performance metrics of Multi-Layer Perceptron (MLP) models using two different datasets: in situ data and TRMM data. The MLP models were evaluated based on their ability to simulate observed values during both the training and testing phases. Key statistical metrics, including mean, maximum, minimum, STD, Var, and CV, are reported for both the observed and simulated data.

Table IV.7: Performance metrics of best model in MLP In Situ and TRMM Data.

			Mean	Max	Min	STD	Var	cv
MLP-in situ data M7	**Train**	**Observed**	3.608	186.75	0	11.884	141.236	3.294
		Simulated	3.772	193.737	-0.313	11.286	127.373	2.992
	Test	**Observed**	5.284	91.6	0	11.038	121.846	2.089
		Simulated	5.347	89.805	-0.410	10.915	104.900	1.915
MLP –in TRMM data M8	**Train**	**Observed**	3.608	186.75	0	11.884	141.236	3.294
		Simulated	3.95	188.484	-1.768	11.935	142.44	3.022
	Test	**Observed**	5.284	91.6	0	11.038	121.846	2.089
		Simulated	5.634	96.617	-0.5602	10.826	117.211	1.921

To clarify, here is a representation of the best models for each algorithm:

For the in-situ data, we provide a visual representation of the performance of different algorithms during the test phase. This includes a Taylor diagram that compares how closely the simulated data from the LSTM, MLP, and XGBoost algorithms match the observed data. The diagram shows that the MLP model is very close to the observed data, indicating a strong match between the model's predictions and the actual measurements. This model exhibits the highest correlation and least bias compared to the observed data. On the other hand, the rain cloud plot and the violin plot reveal some variability in the model's predictions. The MLP model tends to have tighter distributions around the observed data, suggesting it may be the most reliable model among XGBoost and LSTM.

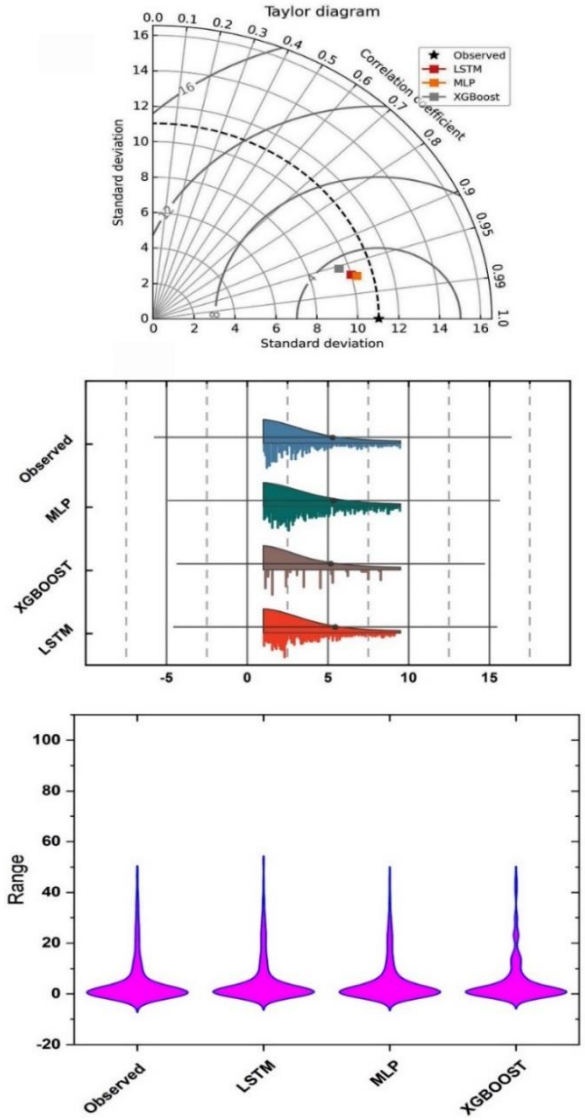

Figure IV.17: Representation of the best models from each algorithm using in situ data during the test phase, Presented using a Taylor diagram, Raincloud plot, and violin plot respectively

For the TRMM data, we provide a visual representation of the performance of different algorithms using in situ data during the test phase. It includes a Taylor diagram that compares how closely the simulated data from the LSTM, MLP, and XGBoost algorithms match the observed data. The diagram shows that the MLP model is very close to the observed data, indicating a strong match between the model's predictions and the actual measurements. This model exhibits the highest correlation and least bias compared to the observed data. On the other hand, the rain cloud plot and the violin plot reveal some variability in the model's predictions. The MLP model tends to have tighter distributions around the observed data, suggesting it may be the most reliable model between XGBoost and LSTM.

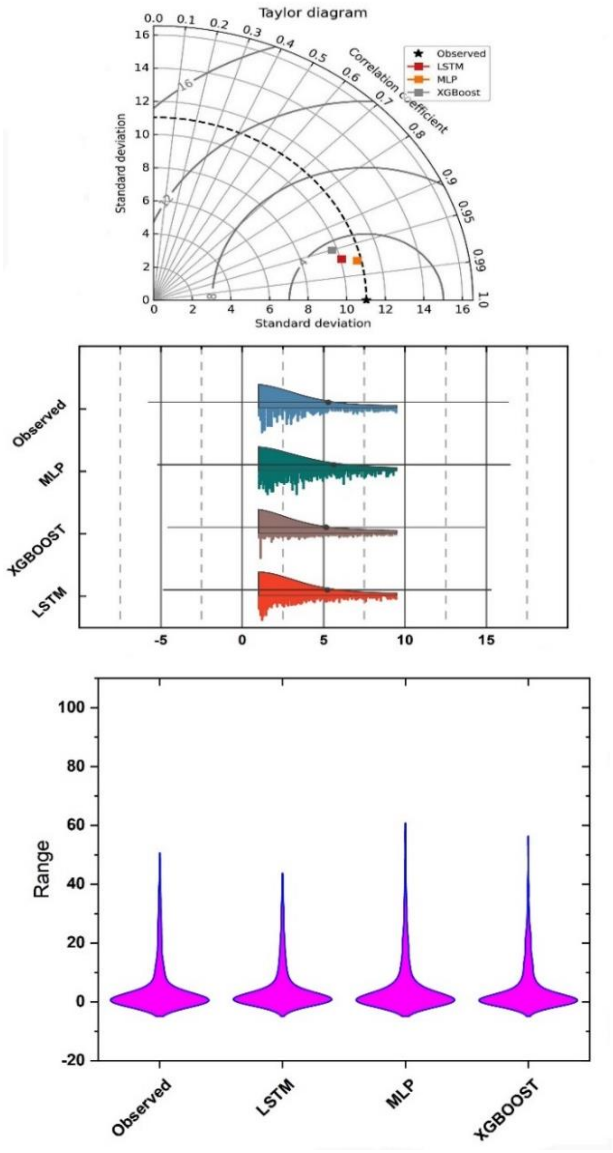

Figure IV.18: Representation of the best models from each algorithm using TRMM data during the test phase, presented using a Taylor diagram, Raincloud plot, and violin plot respectively.

IV.4.Comparison between situ-data and TRMM

An examination comparative of the performance metrics between "**in-situ data**" and "**TRMM data**" shows important differences in both training and testing environments. In terms of NSE, which measures predictive effectiveness, the TRMM dataset consistently displays higher values. Both the training (0.905) and testing (0.94936) sets indicate higher model performance in replicating observed data compared to the in-situ dataset. When examining the RMSE representing the overall accuracy of the models, the TRMM dataset also shows lower values in both training 3.661 and test 2.485 sets, suggesting higher accuracy in

predicting observed values compared to the in-situ dataset. The MAE additionally supports the superiority of the TRMM dataset, highlighting lower values in both training 1.238 and test 1.158 sets. Importantly, the R and R^2 values regularly favor the TRMM dataset, indicating stronger positive correlations and indicating a stronger alignment between predicted and observed values, which means a better model fit. Overall, the comprehensive analysis highlights the commendable predictive efficiency of Models M5 to M9 with the TRMM dataset, as a more strong and accurate choice for hydrological modeling when compared to the in-situ dataset. These findings are pivotal for decision-makers. (See the figure IV.20)

Table IV.8: Performance criteria of during train and test phases. For the best models in both TRMM and in situ data in the MLP algorithms.

		NSE	RMSE	MAE	R	R^2
in-situ data M7	**Train**	0.875	**4.208**	1.339	0.935	0.874225
	Test	0.94201	**2.659**	1.178	0.9715	0.94381225
TRMM data M8	**Train**	0.905	**3.661**	1.238	0.953	0.908209
	Test	0.94936	**2.485**	1.158	0.9748	0.95023504

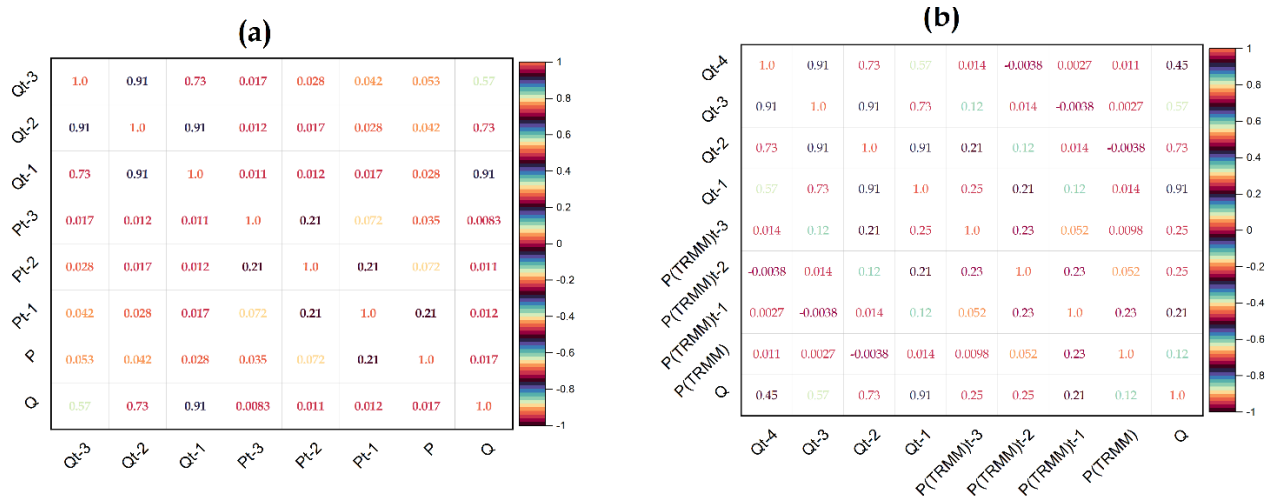

Figure IV.19: Representation of the correlation plot for the input and target variables data in the best model by: (a) in situ data, (b) TRMM.

In Figure IV.19, we can see the correlation plots for input and target variables in the best model, comparing in situ data (a) and TRMM data (b). Panel (a) shows strong correlations among discharge variables (Qt-3, Qt-2, Qt-1, and Q) and moderate correlations between past discharges and current precipitation (P). Panel (b), which includes TRMM precipitation data (P_{TRMM}), demonstrates similarly strong correlations among discharge variables and significant correlations between TRMM precipitation and discharge. Both datasets reveal important

precipitation-discharge relationships, with TRMM data providing additional valuable information for understanding these dynamics.

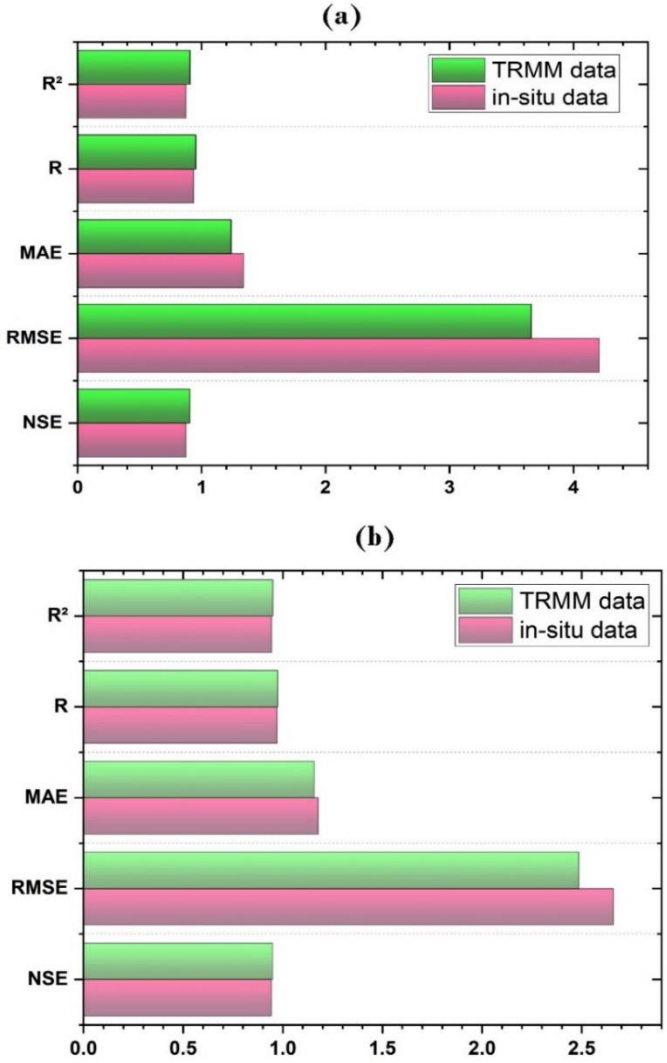

Figure IV.20: Representation of the performance parameters in best models using the in-situ and TRMM data by: (a) Train phase, (b) Test phase.

Figure IV.21, presents a comprehensive evaluation of the best MLP models for in situ data during the test phase, using a Taylor diagram, a raincloud plot, and a violin plot. The Taylor diagram at the top shows the standard deviation, correlation coefficient, and centered RMSE of the models. Here, the MLP model using in situ data, demonstrates a high correlation coefficient and a standard deviation relatively close to the observed data, indicating good performance with moderate RMSE. The raincloud plot in the middle combines density plots, box plots, and scatter plots to display the distribution of observed data and predictions from the MLP models. The in situ data model's distribution closely aligns with the observed data, suggesting accurate predictions. The violin plot at the bottom further compares the range and density of the data across observed values, MLP in situ data, and MLP TRMM data. Both MLP

models exhibit a distribution similar to the observed data, confirming their capability to capture the variability and range of the observed phenomenon. Collectively, these plots demonstrate that the MLP model using in situ data performs well in replicating observed data, highlighting its reliability and accuracy.

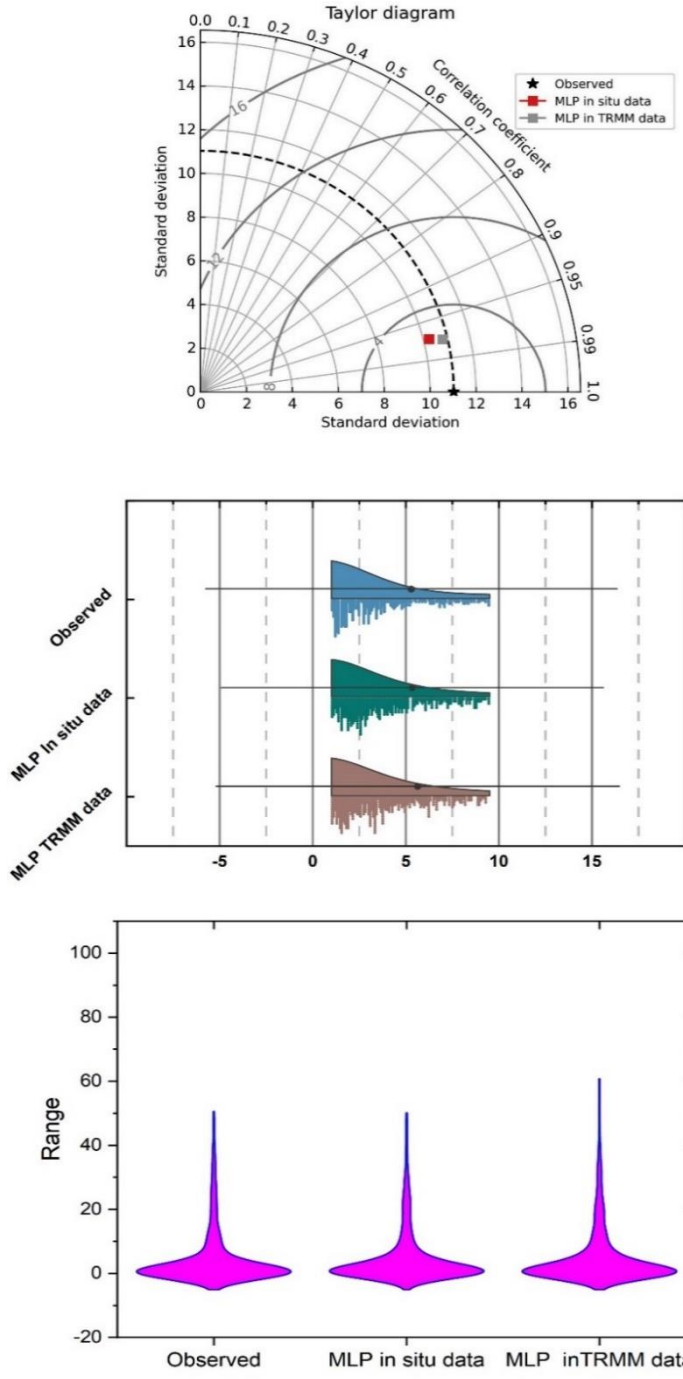

Figure IV.21: Representation of the best MLP models for both in -situ and TRMM data during the test phase, illustrated using a Taylor diagram, raincloud plot, and violin plot, respectively

IV.5.Discussion

When evaluating the results of each study in comparison to the present research, several key metrics were considered, including the size of the data series, NSE, and RMSE. Zhang et al. (**2023**) investigated daily runoff series from various hydrological stations, reporting differing RMSE values (33.83 m^3/s and 38.45 m^3/s) and high NSE scores (0.95 and 0.96) for each station. He et al. (**2024**) focused on the Qujiang River, presenting a single data series of daily runoff data with a comparatively higher RMSE (64.6 m^3/s). Bajirao et al. (**2021**) examined the Koyna River Basin, reporting an RMSE of 77.75 m^3/s. Lu et al. (**2023**) analyzed the Fuchun River Reservoir, yielding an RMSE of 38.82 m^3/s, but NSE was not reported. Nascimento et al. (**2022**) and Zanial et al. (**2023**) focused on TRMM data, achieving NSE values of 0.82 and 0.606 respectively. Gomaa et al. (**2023**) achieved an RMSE of 60.03 m^3/s and a high NSE of 0.96 for the Três Marias Reservoir. Adane et al. (**2021**) reported an NSE of 0.82 for the Awash River Basin. Ying Bi et al. (**2020**) achieved a low RMSE of 2.58 m^3/s and a high NSE of 0.993 for the Qingxi river basin. Tang et al. (**2021**) obtained an RMSE of 4.49 m^3/s and a high NSE of 0.92 for the Shouxi River. In comparison, the present study on Wadi ouahrane (Chelif) utilized TRMM data, resulting in a relatively low RMSE of 2.4850 m^3/s and a commendable NSE of 0.9493. These results suggest that the present study's model demonstrates strong performance in accurately predicting runoff dynamics compared to previous research efforts, particularly in terms of minimizing errors and maximizing the agreement between simulated and observed values.

The wadi ouahrane basin, using LSTM, XGBoost, MLP by used two types of datasets TRMM and in situ Datasets. The effectiveness of each algorithms was assessed based on various statistical metrics. The outcomes indicated that the MLP in both datasets consistently outperformed the XGBoost and LSTM, across most input combinations it achieved the lowest RMSE in several cases indicating its spurious predictive accuracy, and the LSTM also exhibited competitive performance, particularly in capturing nonlinear patterns and complex dependencies However, the XGBoost generally had higher RMSE values compared to the other models for all input combinations, consistent with previous research findings.

The MLP model emerged as the best-performing model in TRMM datasets compared to the in situ datasets consistently achieving the lowest RMSE values across different input combinations. Especially in the M8 in TRMM and in the M7 in the in situ datasets, It demonstrated significant improvement over the XGBoost and LSTM models, highlighting its effectiveness in capturing the complex rainfall-runoff relationship and accurately predicting

runoff discharge, The MLP model exhibited significant improvement in MAE and RMSE in contrast to the XGBoost and LSTM model during testing, indicating its effectiveness in capturing stream flow dynamics and making accurate predictions on unseen data.

Table IV.9: Comparison of the XGBoost –MLP-LSTM models from the present study with other models reported in the literature.

Authors	Location	Algorithms used	Data type	RMSE (m^3/s)	NSE	MAE (m^3/s)	R^2	Length
Zhang et al,2023	the lower Yellow River in (China)	VMD-HHO-KELM	Daily runoff series from the Gaocun and Lijin Hydrological stations.	Gaocun hydrological station: 33.83 Lijin hydrological station: 38.45	/	13.13 8.03	0.95 0.96	2016-2020 (daily)
He et al,.2024	Qujiang River (china).	SD-GRU	Daily runoff of Qingjiang Shuibuya. the average rainfall and runoff data	64.6	/	38.5	0.87	2013-2019 (daily)
Bajirao et al, .2021	Koyna River Basin (India).	ANN, WANN, ANFIS, WANFIS	Daily rainfall and runoff time series data	77.75	/	/	0.93	1999-2011 (daily)
Lu et al, .2023	Fuchun River Reservoir in the Qiantang River basin (china)	RF, XGBoost, AdaBoost, Proposed Stacking Ensemble Learning	Daily inflow	38.82	/	24.27	0.93	1970-2011 (daily)
Nascimento et al.2022	Três Marias Reservoir (Brazil)	SOM	TRMM	/	0.82	/	/	1998-2019 (daily)
Gomaa et al., 2023	Três Marias Reservoir (Brazil)	GRNN MLP-PSO GP	TRMM data	MLP-PSO: 60.03	0.96	/	/	1988-2019 (daily)
Adane et al. 2021.	Awash River Basin (Ethiopia)	GR2M	TRMM 3B43v7	/	0.82	/	/	1998-2010 (daily)
ying Bi et al,.2020	Qingxi river basin (China.)	CAGANet SVM LSTM AM-LSTM	daily rainfall daily evaporation,	2.58	0.993	0.60	/	1986-2005 (daily)

			and daily runoff data					
Zanial et al.2023	The hydro power plant (Malaysia)	HP11	SDSM and TRMM rainfall Daily	12.4	/	/	0.606	1980-1986 (daily)
Tang et al.2021	The Shouxi River (China)	LSTM	IMERG data	4.49	0.92	/	/	2014-2020 (hourly)
Present Study	Wadi ouahrane (Chelif)	LSTM XGBOOST MLP	TRMM	2.4850	0.9493	1.238	0.95	1998-2012 (daily)

Moreover, the study examined the impact of incorporating different components on the prediction accuracy of runoff. The results revealed that Model M8, in TRMM datasets that incorporated specific components and variables, consistently achieved the lowest RMSE values in both the training and testing stages. This model demonstrated superior accuracy in predicting Runoff. Comparisons with other models reported in the literature highlighted the competitive performance of the MLP model in runoff prediction. It outperformed various models in terms of RMSE and NSE, showcasing its effectiveness in capturing the observed runoff dynamics.

IV.6.Conclusion

The comparative analysis of in situ and TRMM data provides an important understanding of the performance of three machine learning algorithms. Among them, MLP stands out as the most reliable and effective model across both datasets, consistently achieving the lowest RMSE values of 2.485 for TRMM data and 2.659 for in situ data. LSTM shows moderate performance, particularly excelling with in situ data, achieving an RMSE of 2.847. Conversely, XGBoost has the highest RMSE values in both scenarios, with 11.879 for in situ data and 11.721 for TRMM data, indicating limited effectiveness in these contexts. We did not use optimization or hybrid models such as time-frequency techniques; instead, we used grid search for parameter tuning with XGBoost. This evaluation provides a clear understanding of the most suitable models for each dataset and offers valuable guidance for future modeling efforts in similar scenarios.

General conclusion

General conclusion

This study is a part of the accurate daily runoff prediction for the Wadi Ouahrane basin in the Chelif basin (northern Algeria) by utilizing two types of data for comparison: in situ data and TRMM data. To accomplish this, we employ three ML algorithms: LSTM, XGBoost, and MLP. We evaluate the accuracy of the models in each algorithm using RMSE, MAE, NSE, R, and R^2. However, in this study, the RMSE was set to measure how well the model evaluates.

The obtained results are summarized in the following points:

- The 9 models in the MLP for in situ data show that M7 (Qt-3, Qt-2, Qt-1, Pt-3, Pt-2, Pt-1, P, and Q as outputs) gives the best results with the lowest RMSE values in M7 (Train phase = 4.2080, Test phase = 2.6590).
- The 9 models in the LSTM for in situ data show that M7 (Qt-3, Qt-2, Qt-1, Pt-3, Pt-2, Pt-1, P, and Q as outputs) gives the best results with the lowest RMSE values in M7 (Train phase = 4.2080, Test phase = 2.8470).
- The 9 models in XGBoost for in situ data show that M5 (Qt-1, Pt-3, Pt-2, Pt-1, P, and Q as outputs) gives the best results with the lowest RMSE values in M5 (Train phase = 5.4840, Test phase = 3.4540).
- In the TRMM data the 9 models in the MLP shows that the M8 (Qt-4,Qt-3,Qt-2,Qt-1, P(TRMM)t-3 ,P(TRMM)t-2 ,P(TRMM)t-1 ,P(TRMM) and Q as outputs) gives the best results with the lowest RMSE values in M8 (Train phase = 3.6610, Test phase = 2.4850).
- In the TRMM data the 9 models in the LSTM shows that the M5 (Qt-1, P(TRMM)t-3 ,P(TRMM)t-2 ,P(TRMM)t-1 ,P(TRMM) and Q as outputs) gives the best results with the lowest RMSE values in M5 (Train phase = 4.9040, Test phase = 2.8210).
- In the TRMM data the 9 models in the XGBoost shows that the M9 (Qt-5,Qt-4,Qt-3,Qt-2,Qt-1, P(TRMM)t-3 ,P(TRMM)t-2 ,P(TRMM)t-1 ,P(TRMM) and Q as outputs) gives the best results with the lowest RMSE values in M9 (Train phase =2.4510, Test phase = 3.5250).
- The high RMSE values are obtained in the LSTM in M4 (train phase =11.8765, Test phase=11.1690) for the in-situ data and in the TRMM data in the LSTM the M1 (train phase=11.720, Test phase=11.1090).

- The simulation shows that the MLP successfully reduced the RMSE in the test phase for both datasets, but the TRMM data the MLP gives the good results compared to the in situ data and compared to the XGBoost and LSTM.

Future research, will focus on integrating time-frequency analysis approaches and other optimization strategies to hybridize the model and improve its performance. Our goal is to attain results that are more precise and effective by incorporating these cutting-edge methods. To enhance the precision and fine-tune the parameters of our model, optimization methods including simulated annealing, particle swarm optimization, and genetic algorithms could be applied. Furthermore, techniques for time-frequency analysis, such as wavelet transforms or short-time Fourier transforms, may offer more profound understanding of the temporal patterns in the data, improving the model's ability to handle intricate, non-stationary signals. With this diverse approach, we hope to push the limits of current performance levels and create new opportunities for application across a range of areas.

Bibliographic references

Bibliographic references

- Asadieh, B., Krakauer, N. Y., & Fekete, B. M. (2016). Historical trends in mean and extreme runoff and stream flow based on observations and climate models. *Water*, 8(5), 189. https://doi.org/10.3390/w8050189.
- Achite, M., Ceribasi, G., Wałęga, A., Ceyhunlu, A. I., Elshaboury, N., Krakauer, N., Hartani, T., Caloiero, T., & Gul, S. (2023). Analysis of monthly average precipitation of Wadi Ouahrane basin in Algeria by using the ITRA, ITPAM, and TPS methods. Environmental Monitoring and Assessment, 195(606). https://doi.org/10.1007/s10661-023-11236-3
- Amatya, D., Walega, A., Callahan, T., Morrison, A., Vulava, V., Hitchcock, D., Williams, T., & Epps, T. (2022). Storm event analysis of four forested catchments on the Atlantic Coastal Plain using a modified SCS-CN rainfall-runoff model. *Journal of Hydrology*. https://doi.org/10.1016/j.jhydrol.2022.127772.
- Abro, M. I., Zhu, D., Khaskheli, M. A., Elahi, E., & Ramay, M. A. H. (2020). Statistical and qualitative evaluation of multi-sources for hydrological suitability in flood-prone areas of Pakistan. Journal of Hydrology, 588, 125117. https://doi.org/10.1016/j.jhydrol.2020.125117.
- Abda, Z., Zerouali, B., Chettih, M., Guimaraes Santos, C. A., de Farias, C. A. S., & Elbeltagi, A. (2022). Assessing machine learning models for stream flow estimation: a case study in Oued Sebaou watershed (Northern Algeria). Hydrological Sciences Journal, 67(9), 1328-1341.
- Aoulmi, Y., Marouf, N., Amireche, M., Kisi, O., Shubair, R. M., & Keshtegar, B. (2021). Highly accurate prediction model for daily runoff in semi-arid basin exploiting metaheuristic learning algorithms. Ieee Access, 9, 92500-92515.
- Adam, E. O., Abd Elbasit, M. A. M., Solomon, T., & Ahmed, F. (2017). Integration of satellite rainfall data and curve number method for runoff estimation under semi-arid wadi system. The International Archives of the Photogrammetry, Remote Sensing and Spatial Information Sciences, XLII-3/W2, 1-444. https://doi.org/10.5194/isprs-archives-XLII-3-W2-1-2017.
- Bardossy, A., Kilsby, C., Birkinshaw, S., Wang, N., & Anwar, F. (2022). Is precipitation responsible for the most hydrological model uncertainty, Frontiers in Water, 4, 836554. https://doi.org/10.3389/frwa.2022.836554.

- Beven, K. J. (2012). *Rainfall-runoff modelling: The primer*. John Wiley & Sons.
- Bai, Y., Zhang, Z., & Zhao, W. (2019). Assessing the impact of climate change on flood events using HEC-HMS and CMIP5. *Water, Air, & Soil Pollution*. https://doi.org/10.1007/s11270-019-4159-0.
- Beck, H. E., Vergopolan, N., Pan, M., Levizzani, V., van Dijk, A. I. J. M., Weedon, G. P., Brocca, L., Pappenberger, F., Huffman, G. J., & Wood, E. F. (2017). Global-scale evaluation of 22 precipitation datasets using gauge observations and hydrological modeling. Hydrology and Earth System Sciences, 21(12), 6201–6217. https://doi.org/10.5194/hess-21-6201-2017.
- Bajirao, T. S., Kumar, P., Kumar, M., Elbeltagi, A., & Kuriqi, A. (2021). Potential of hybrid wavelet-coupled data-driven-based algorithms for daily runoff prediction in complex river basins. Theoretical and Applied Climatology, 145(4), 1207–1231. https://doi.org/10.1007/s00704-021-03681-2.
- Chen, T.; Guestrin, C. XGBoost: A Scalable Tree Boosting System. In Proceedings of the 22nd ACM SIGKDD International Conference on Knowledge Discovery and Data Mining (KDD '16), San Francisco, CA, USA, 13–17 August 2016.
- Chen, L., & Wang, L. (2018). Recent advances in Earth observation big data for hydrology. Geospatial Information Science, 21(2), 143-156. https://doi.org/10.1080/20964471.2018.1435072.
- Devia, G. K., Ganasri, P., & Dwarakish, G. S. (2015). A review on hydrological models. In International Conference on Water Resources, Coastal and Ocean Engineering (ICWRCOE 2015) (Vol. 4, pp. 1001-1007). https://doi.org/10.1016/j.aqpro.2015.02.126.
- Farnsworth, R. K., Barrett, E. C., & Dhanju, M. S. (1984). *Application of remote sensing to hydrology including ground water*. United Nations Educational, Scientific and Cultural Organization (UNESCO). Paris, France. Retrieved from https://www.ircwash.org/sites/default/files/212.1-84AP-5812.
- G.B. Adane, B.A. Hirpa, B.M. Gebru, C. Song, W.-K. Lee, Integrating satellite rainfall estimates with hydrological water balance model: rainfall-runoff modeling in awash River Basin, Ethiopia, Water 13 (2021) 800, https://doi.org/10.3390/w13060800.
- Gomaa, E., Zerouali, B., Difi, S., El-Nagdy, K. A., Santos, C. A. G., Abda, Z., Ghoneim, S. S. M., Bailek, N., da Silva, R. M., Rajput, J., & Ali, E. (2023). Assessment of hybrid machine learning algorithms using TRMM rainfall data for daily inflow forecasting in Trˆes Marias Reservoir, eastern Brazil. *Heliyon, 9*, e18819.

- Hong, Z., Han, Z., Li, X., Long, D., & Wang, J. (2021). Generation of an improved precipitation data set from multisource information over the Tibetan Plateau. Journal of Hydrometeorology, 22(3), 627–645. https://doi.org/10.1175/JHM-D-20-0252.1.
- Huang, Q., Qin, G., Zhang, Y., Tang, Q., Liu, C., Xia, J., & Francis, D. H. S. (2020). Using remote sensing data based hydrological model calibrations for predicting runoff in ungauged or poorly gauged catchments. *Water Resources Research*, 56(12), e2020WR028205. https://doi.org/10.1029/2020WR028205.
- Herath, H. M. V. V., Chadalawada, J., & Babovic, V. (2020). Hydrologically informed machine learning for rainfall-runoff modelling: Towards distributed modelling.
- He, X., Chaney, N., Schleiss, M., & Sheffield, J. (2016). Spatial downscaling of precipitation using adaptable random forests. Water Resources Research, 52(12), 9343–9365. https://doi.org/10.1002/2016WR019034.
- Hochreiter, S.; Schmidhuber, J. Long Short-Term Memory. Neural Comput. **1997**, 9, 1735–1780.
- Habib, E., et al. (2009). Evaluation of TMPA satellite-based research and real-time rainfall estimates during six tropical-related heavy rainfall events over Louisiana, USA. Atmospheric Research, 94(3), 373–388.
- He, F., & Zhang, X. (2024). Daily runoff prediction with a seasonal decomposition-based deep GRU method. *WATER*, 16(4), 618. https://doi.org/10.3390/w16040618.
- Islam, K. I., Elias, E., Carroll, K. C., & Brown, C. (2023). Exploring random forest machine learning and remote sensing data for stream flow prediction: An alternative approach to a process-based hydrologic modeling in a snowmelt-driven watershed. Remote Sensing, 15(16), 3999. https://doi.org/10.3390/rs15163999.
- International Atomic Energy Agency Information Series Division of Public Information 02-01578 / FS Series 2/03/E.
- Iamampai, S., Talaluxmana, Y., Kanasut, J., & Rangsiwanichpong, P. (2024). Enhancing rainfall–runoff model accuracy with machine learning models by using soil water index to reflect runoff characteristics. Water Science & Technology, 89(2), 368-381.
- Jehanzaib, M., Ajmal, M., Achite, M., & Kim, T.-W. (2022). Comprehensive review: Advancements in rainfall-runoff modelling for flood mitigation. Climate, 10(10), 147. https://doi.org/10.3390/cli10100147.

- Jehanzaib, M., Shah, S. A., Yoo, J., & Kim, T.-W. (2020). Investigating the impacts of climate change and human activities on hydrological drought using non-stationary approaches. *Journal of Hydrology*. https://doi.org/10.1016/j.jhydrol.2020.125052.
- Khosravi, K., Mirzai, H., & Saleh, I. (2013). Assessment of empirical methods of runoff estimation by statistical test, 1(3), 285–301.

- Kun Huang, Jing Zhang, Yongyu Song, "Application of machine learning models based on ANN and GA coupling algorithms in hydrological runoff simulation," Proc. SPIE 12256, International Conference on Electronic Information Engineering, Big Data, and Computer Technology (EIBDCT 2022), 122561K (6 May 2022); https://doi.org/10.1117/12.2635807.
- Khanbilvardi, R., Lakhankar, T., Krakauer, N., Nazari, R., & Powell, A, and Al Powell 1NOAA-CREST, The City College of New York, 160 Convent Ave, New York, NY, USA. Remote Sensing Data and Information for Hydrological Monitoring and Modeling.
- Kittel, C. M. M., Nielsen, K., Tottrup, C., & Bauer-Gottwein, P. (2018). Informing a hydrological model of the Ogooue with multi-mission remote sensing data. *Hydrology and Earth System Sciences*, **22**(2), 1453–1472. https://doi.org/10.5194/hess-22-1453-2018.
- Kite, G. W., & Pietronior, A. (1996). Remote sensing applications in hydrological modelling. *Hydrological Sciences Journal*, 41(4), 563–591. https://doi.org/10.1080/02626669609491526.
- Kumar, A., Ramsankaran, R., Brocca, L., & Muñoz-Arriola, F. (2019). A machine learning approach for improving near-real-time satellite-based rainfall estimates by integrating soil moisture. Remote Sensing, 11(19), 2221. https://doi.org/10.3390/rs11192221.
- Liu, X., Liu, F. M., Wang, X. X., et al. (2017). Combining rainfall data from rain gauges and TRMM in hydrological modelling of Laotian data-sparse basins. Applied Water Science, 7*, 1487–1496. Doi: 10.1007/s13201-015-0330-y.
- Lettenmaier, D. P., Wood, E. F., & Sharif, M. (1999). Hydrologic modeling of continental-scale basins. *Water Resources Research*, 35(5), 1541-1551.
- Lu, M.; Hou, Q.; Qin, S.; Zhou, L.; Hua, D.; Wang, X.; Cheng, L. A Stacking Ensemble Model of Various Machine Learning Models for Daily Runoff Forecasting. Water **2023**, 15, 1265. https://doi.org/10.3390/w15071265.
- M. Tayyab, D. Xiaohua, M. Sibtain, I. Ahmad, A. Zahra, M.I. Azam, Monthly stream flow forecasting using decomposition-based hybridization with two-step verification

method over the Mangla watershed, Pakistan, Iran. J. Sci. Technol. Transac. Civil Eng. (2022) 1–20.

- Martinez, J. M. (2022). Use of data science tools for assessing inland water surface and quality on regional scales through high-resolution Sentinel-2 remote sensing images [Doctoral dissertation, University of Toulouse 3].

- Nimai, S., Ren, Y., Tianqi, A., Zhou, L., Liang, H., & Cui, Y. (2023). Enhancing runoff simulation using BTOP-LSTM hybrid model in the Shinano River Basin. Water, 15(21), 3758. https://doi.org/10.3390/w15213758.
- Qanati, B., & Mohammadi, J. (2019). Remote sensing in hydrology. *[Journal Name]*, 2(1), 27-34. Retrieved from http://www.sciarena.com/.
- Ran, J., Cui, Y., Xiang, K., & Song, Y. (2022). Improved runoff forecasting based on time-varying model averaging method and deep learning. PLoS ONE, 17(9), e0274004. https://doi.org/10.1371/journal.pone.0274004.
- REMAOUN Mohamed (2007), Crues et sécheresses en Algérie, Cas du Moyen Cheliff, thèse de doctorat d'Etat, USTHB, 240 p.
- Schmugge, T. J., Kustas, W. P., Ritchie, J. C., Jackson, T. J., & Rango, A. (2002). Remote sensing in hydrology. *Hydrological Processes*, 25(8-12), 1367-1385. https://doi.org/10.1016/S0309-1708(02)00065-9.
- Sitterson, J., Knightes, C., Parma, R., Wolfe, K., Avant, B., & Muche, M. (2018). An overview of rainfall-runoff model types. In *Proceedings of the International Congress on Environmental Modelling and Software* (Paper No. 41).
- Stewart, J. B., & Finch, J. W. (1993). Application of remote-sensing to forest hydrology. *Journal of Hydrology*, **150**(2–4), 701–716. https://doi.org/10.1016/0022-1694(93)90132-s.
- Sutanudjaja, E. H., van Beek, L. P. H., de Jong, S. M., van Geer, F. C., & Bierkens, M. F. P. (2014). Calibrating a large-extent high-resolution coupled .Groundwater-land surface model using soil moisture and discharge data. *Water Resources Research*, **50**, 687 705. https://doi.org/10.1002/2013wr013807.
- Schultz, G. A. (1993). Hydrological modeling based on remote sensing information. Advances in Space Research, 13(5), 149-166. https://doi.org/10.1016/0273-1177(93)90540-R.
- Samantaray, S., & Sahoo, A. (2020). Estimation of runoff through BPNN and SVM in Agalpur Watershed. Publisher. https://doi.org/10.1007/978-981-13-9920-6_27.

- Saha, A., & Pal, S. C. (2024). Application of machine learning and emerging remote sensing techniques in hydrology: A state-of-the-art review and current research trends. Journal of Hydrology, 632, 130907. https://doi.org/10.1016/j.jhydrol.2024.130907.

- Suroso, Santoso, P. B., Birkinshaw, S., Kilsby, C., Bardossy, A., & Aldrian, E. (2023). Assessment of TRMM rainfall data for flood modeling in three contrasting catchments in Java, Indonesia. Journal of Hydro informatics. 25 (3): 797–814 ; https://doi.org/10.2166/hydro.2023.132.
- Sreedevi, S., Kunnath-Poovakka, A., & Eldho, T. I. (2021). Comparison of conceptual and distributed hydrological models for runoff estimation in a river basin. In M. Chauhan & C. S. P. Ojha (Eds.), The Ganga River Basin: A Hydro meteorological Approach (pp. 173–190). Springer. https://doi.org/10.1007/978-3-030-60869-9_9.
- Schmugge, T. J., Kustas, W. P., Ritchie, J. C., Jackson, T. J., & Rango, A. (2002). Remote sensing in hydrology. *Advances in Water Resources, 25*(8-12), 1367-1385. Retrieved http://www.elsevier.com/locate/advwatres.
- Shah, G., Zaidi, A., Qureshi, A. L., Hussain, S., Jokhio, R., & Aziz, T. (2023). Rainfall-runoff modeling using machine learning in the urban watershed of Pishin Lora Basin, Balochistan (Pakistan). Research Square. https://doi.org/10.21203/rs.3.rs-3309647/v1.
- Sawunyama, T., & Hughes, D. (2008). Application of satellite-derived rainfall estimates to extend water resource simulation modelling in South Africa. Water SA, 34(1), 1–9.
- Scheele, M., et al. (2011). Evaluation of TRMM Multi-satellite Precipitation Analysis (TMPA) performance in the Central Andes region and its dependency on spatial and temporal resolution. Hydrology and Earth System Sciences, 15 (8), 2649–2663.
- Szczepanek, R. (2022). Daily stream flow forecasting in mountainous catchment using XGBoost, LightGBM and CatBoost. Hydrology, 9(12), 226.
- Todini, E. (1988). The ARNO rainfall-runoff model. *Journal of Hydrology*, 100(1-3), 341-352.
- Tao, Y., GAO, X., Hsu, K., Sorooshian, S., & Ihler, A. (2016). A deep neural network modeling framework to reduce bias in satellite precipitation products. Journal of Hydrometeorology, 17(11), 2859–2879. https://doi.org/10.1175/JHM-D-15-0075.1.
- Tang, X., Yin, Z., Qin, G., Guo, L., & Li, H. (2021). Integration of satellite precipitation data and deep learning for improving flash flood simulation in a poor-gauged

mountainous catchment. Remote Sensing, 13(24), 5083. https://doi.org/10.3390/rs13245083.

- Vaze, J., Jordan, P., Beecham, R., Frost, A., summer ell, G., 2012. Guidelines for rainfall-runoff modelling: Towards best practice model application. pp. 47.
-

- W.N.C.W. Zanial, M.A. Malek, M.N.M. Reba, N. Zaini, A.N. Ahmed, M. Sherif, A. Elshafie, Rainfall-runoff modelling based on global climate model and tropical rainfall Measuring mission (GCM-TRMM): a case study in Hulu Terengganu catchment, Malaysia, Heliyon 9 (5) (2023).
- Wu, J., Wang, Z., Hu, Y., & Zhu, L. (2023). Runoff forecasting using convolutional neural networks and optimized bi-directional long short-term memory. Water Resources Management, 37, 937–953. https://doi.org/10.1007/s11269-022-03414-8.
- Wu, H., Yang, Q., Liu, J., & Wang, G. (2020). A spatiotemporal deep fusion model for merging satellite and gauge precipitation in China. Journal of Hydrology, 590, 124664. https://doi.org/10.1016/j.jhydrol.2020.124664.
- W. Zhang, C. Wu, H. Zhong, Y. Li, L. Wang, Prediction of undrained shear strength using extreme gradient boosting and random forest based on Bayesian optimization, Geosci. Front. 12 (1) (2021) 469–477 Jan, doi: 10.1016/j.gsf.2020.03.007
- Wang, Y., Zhu, C., Li, Y., Zheng, H., & Li, J. (2023). Improving daily runoff prediction in the lower Yellow River using a combined VMD–HHO–KELM model. *Water*, *15*(2), 618. https://doi.org/10.3390/w15040618.
- X. Tang, Z. Yin, G. Qin, L. Guo, H. Li, Integration of satellite precipitation data and deep learning for improving flash flood simulation in a poor-gauged mountainous catchment, Rem. Sens. 13 (24) (2021) 5083.
- Xu, C. Y. (2002). From PDM to PI: A generic rainfall-runoff model for ungauged catchments. *Journal of Hydrology*, 268(1-4), 1-22.
- Yu, L., Wang, Z., Dai, R., & Wang, W. (2023). Daily runoff prediction based on the adaptive Fourier decomposition method and multiscale temporal convolutional network. Environmental Science and Pollution Research International, 30(42), 95449-95463. https://doi.org/10.1007/s11356-023-28936-5
- Yang, X., Zhou, J., Zhang, Q., & Wang, Y. (2024). Evaluation and interpretation of runoff forecasting models based on hybrid deep neural networks. Water Resources Management, 38, 1987–2013. https://doi.org/10.1007/s11269-023-03731-6

- Yan, L., Lei, Q., Jiang, C., Yan, P., Ren, Z., Liu, B., & Liu, Z. (2022). Climate-informed monthly runoff prediction model using machine learning and feature importance analysis. *Frontiers in Environmental Science, 10*. https://doi.org/10.3389/fenvs.2022.1049840

- Yassin, F., Razavi, S., Wheatear, H., Sapriza-Azuri, G., Davison, B., & Pietroniro, A. (2017). Enhanced identification of a hydrologic model using stream flow and satellite water storage data: A multicriteria sensitivity analysis and optimization approach. Hydrological Processes, **31**(19), 3320–3333. https://doi.org/10.1002/hyp.11267
- Zhang, Y., Chiew, F. H. S., Liu, C., Tang, Q., Xia, J., Tian, J., Kong, D., & Li, C. (2020). Can remotely sense actual evapotranspiration facilitate hydrological prediction in ungauged regions without runoff calibration? *Water Resources Research*, **56**, e24394. https://doi.org/10.1029/2019wr026236
- Zhu, S., Wei, J., Zhang, H., Xu, Y., & Qin, H. (2023). Spatiotemporal deep learning rainfall-runoff forecasting combined with remote sensing precipitation products in large scale basins. *Journal of Hydrology*, 616, 128727. https://doi.org/10.1016/j.jhydrol.2022.128727

- Zhang, X., Liu, F., Yin, Q., & Yuan, J. (2023). A runoff prediction method based on hyper parameter optimization of a kernel extreme learning machine with multi-step decomposition. Scientific Reports, 13, 19341. https://doi.org/10.1038/s41598-023-46682-z.
- Zhang, Y., Ryu, D., & Zheng, D. (2021). Using remote sensing techniques to improve hydrological predictions in a rapidly changing world. *Remote Sensing*, 13(19), 3865. https://doi.org/10.3390/rs13193865.
- ZEKOUDA Naima, Modélisation des crues d'oued Ouahrane pour la gestion intégrée des risques d'inondation, l'obtention du diplôme de Magister, University Hassiba Ben Bouali. Chlef, Faculty of Sciences and Engineering Dep https://gpm.nasa.gov/missions/trmmartment of Hydraulic, 2009.

Websites

- https://www.spatialpost.com/application-of-remote-sensing-in-hydrology/
- https://labelyourdata.com/articles/data-collection-methods-AI

- https://www.ayadata.ai/blog-posts/challenges-of-data-collection-for-ml-explained/
- https://www.epa.gov/water-research/visualizing-ecosystem-land-management-assessments-velma-model-20.
- MIKE SHE (mikepoweredbydhi.com)

- GES DISC Dataset: TRMM (TMPA) Precipitation L3 1 day 0.25 degree x 0.25 degree V7 (TRMM_3B42_Daily 7) (nasa.gov)
- https://earthobservatory.nasa.gov/features/TRMM.